Dielectron Performance of the CBM Experiment at $\sqrt{s} = 3.19\,\mathrm{GeV}$

Master Thesis in Physics

Luisa Faber

Institut für Kernphysik
Universität Münster

Supervised by

Anton Andronic
and
Christian Klein-Bösing

May, 2026

First Referee: Prof. Dr. Anton Andronic

Second Referee: Apl. Prof. Dr. Christian Klein-Bösing

Contents

1 Introduction

Protons and neutrons consist of quarks and gluons, fundamental constituents of the visible matter surrounding us. These quarks and gluons are confined within hadrons such as neutrons and protons and cannot be observed freely [1]. Under extreme conditions, however, quarks and gluons can transition to a deconfined state of matter known as quark-gluon plasma (QGP). Microseconds after the Big Bang, the universe passed through such a state, and a similar state is also expected to exist in the cores of neutron stars [2]. These states typically occur at extremely high temperatures and/or densities.

To recreate such extreme conditions and study these states of matter, large-scale experiments must be constructed. In such experiments particles are collided and for timescales in the range of 10^{-23} s [2] high densities and/or temperatures can be reached in the so-called fireball. At the Large Hadron Collider (LHC), located in Geneva at the European Organization for Nuclear Research (CERN), heavy ions are accelerated in a ring with a circumference of 27 km and collided in experiments such as ALICE (A Large Ion Collider Experiment) [3]. These heavy-ion collisions can reach temperatures exceeding 10^{12} K [2], briefly reproducing the state of matter that existed shortly after the Big Bang. Hence, at ALICE the high-temperature and low-density region is accessed.

Complementing this, the upcoming Facility for Antiproton and Ion Research (FAIR) in Darmstadt accesses the high-density, moderate-temperature regime. In the fixed-target experiment CBM, accelerated ions are directed onto a fixed target to produce heavy-ion collisions. These collisions achieve lower temperatures but higher densities, allowing to probe a different part of the QCD phase diagram. In this region, a first-order phase transition between confined and deconfined matter is expected, in contrast to the smooth crossover observed in the conditions investigated by ALICE. Confirming this first-order phase transition would also imply the existence of a critical point seperating the crossover and first-order phase transition. To probe this region, the center of mass energy range from $\sqrt{s_{\mathrm{NN}}} = 2.7\,\mathrm{GeV}$ to $\sqrt{s_{\mathrm{NN}}} = 5\,\mathrm{GeV}$ is accessed. In addition, to use rare probes, CBM is designed to operate at interaction rates of up to 10^7 Hz [4].

Dileptons are an important tool for probing collision properties such as temperature, as they are produced throughout the evolution of the collision and leave the fireball undisturbed [5].

For dilepton studies in CBM, this work builds on the PAPA analysis framework, most recently refined by Adrian Meyer-Ahrens for top energy ($P_{\text{beam}} = 12\,\text{AGeV/c}$) [6]. The analysis chain is adapted in this thesis for $P_{\text{beam}} = 4.41\,\text{AGeV}$, corresponding to $\sqrt{s_{\text{NN}}} = 3.19\,\text{GeV}$.
As the CBM experiment is still under construction, no data is available. However, different simulation tools can model heavy-ion collisions and detector response based on the current design. Such simulations are crucial for evaluating detector performance, optimizing design parameters, and developing and testing analysis frameworks, since they provide both simulated detector signals and access to the true associated particle information. In this thesis different tools are used to access the data.
The analysis goal is to efficiently preserve signal electrons while rejecting background such as hadrons and conversion electrons. CBM subdetectors provide different information which can be used to distinguish signal electrons from other particles based on their properties. Thus different rejection cuts are applied using the detector information.
Additionally, the beampipe, through which the beam travels to the downstream beam dump, requires specific consideration. As beam trajectories in the magnetic field depend on momentum, either the field or beampipe geometry must be adjusted to avoid the beam colliding with the beampipe. Field scaling, however, degrades momentum resolution. Therefore, three dedicated beampipes are planned for CBM to operate at different energies with full magnetic field. With no beampipe available for $P_{\text{beam}} = 4.41\,\text{AGeV}$, this thesis compares two different scenarios: either using the beampipe `v24h` designed for top energy $P_{\text{beam}} = 12\,\text{AGeV/c}$ or the one built for $P_{\text{beam}} = 5.93\,\text{AGeV/c}$, which is called `v24e`. For both cases, the magnetic field must be scaled down to 37 % and 74 % of its nominal value, respectively.
After introducing the theoretical background and experimental setup in chapter 2, chapter 3 presents the simulation framework and detector geometry. The applied selection cuts to suppress background, as well as the comparison of the two beampipe configurations and the additional background simulation, are discussed in chapter 4. Finally, the results are summarized in chapter 5.

2 Theoretical Background

2.1 CBM Experiment

In Darmstadt, FAIR is currently under construction. The planned complex is shown in Fig. 2.1. In addition to two existing accelerators, a linear and a circular one, a new ring accelerator, the SIS100 is build, which will deliver heavy-ion and proton beams of varying energy. Proton beams reach energies of up to 29 AGeV, whereas gold beams reach up to 11 AGeV [7]. Several different experiments are planned, including the CBM experiment,

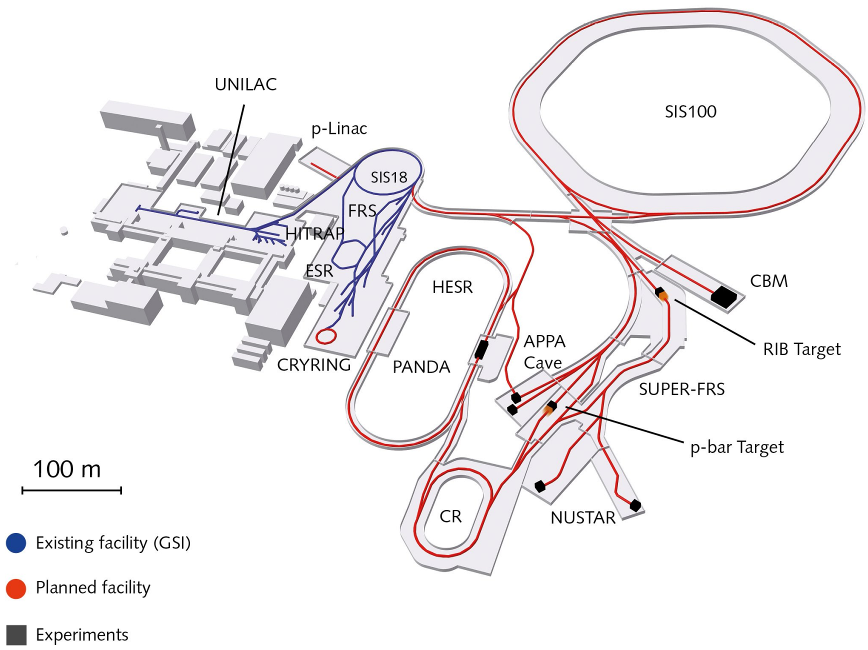

Figure 2.1: Layout of the planned FAIR facility. The main accelerator, SIS100, and various experiments, such as the CBM experiment, are being constructed in order to expand the existing facilities. [8].

which is located right next to the main accelerator ring. CBM is a fixed-target experiment with interaction rates up to 10^7 Hz. A visualization of the CBM experiment in the cave in Fig. 2.2a, showing the individual subdetectors. The lineup of the subdetectors is also shown in Fig. 2.2b. In front of the detectors, drawn in blue in Fig. 2.2a, is a superconducting dipole magnet. Inside this magnet is a vacuum chamber housing the target and the Micro Vertex Detector (MVD), as well as the Silicon Tracking System (STS). Behind the magnet, the Ring Imaging Cherenkov (RICH) Detector, the Transition Radiation Detector (TRD), and the Time-of-Flight System (TOF) are lined up. The experiment can also be operated in the muon setup when RICH is replaced by the Muon Chambers (MuCh). However, only the electron setup is relevant for this thesis and will therefore be described in the following.

(a) **(b)**

Figure 2.2: The layout of the CBM experiment in the cave [9] (a) and as a schematic drawing (b). Different subdetectors are lined up behind the target which is placed inside a superconducting dipole magnet.

2.1.1 Micro Vertex Detector (MVD)

Inside the target vacuum chamber, 8 cm behind the target, the MVD is located. It enables secondary vertex reconstruction for weak decays and momentum reconstruction down to 300 MeV/c. The MVD supports identification of pairs from conversion and π^0–Dalitz decays to reduce background in dilepton spectroscopy. It consists of 4 equidistant layers, each 4 cm apart, built from Monolithic Active Pixel Sensor (MAPS) chips, which enable tracking with a spatial resolution of 5 μm [10].

2.1.2 Silicon Tracking System (STS)

The main tracking device, the STS, achieves a momentum resolution of $\Delta p/p \approx 1\%$ and a tracking efficiency of 95 % for particle momenta above 1 GeV/c. Eight layers, consisting of silicon strip detectors mounted on ladders, cover polar angles $2.5° < \theta < 25°$. These layers are installed between 30 and 100 cm downstream of the target, situated within the magnetic field [11].

2.1.3 Ring Imaging Cherenkov (RICH) Detector

The RICH detector is filled with CO_2 and provides pion suppression up to about 8 GeV/c. In Fig. 2.3a, a sketch of the detector is shown. It consists of two spherical glass mirrors and two photon detectors, installed directly behind the magnet. When a charged particle traverses the CO_2 radiator, Cherenkov light is emitted in a cone with opening angle θ_c around the particle trajectory. This light is reflected by the mirrors and projected onto the photon detectors, where the cone appears as a ring. Electrons passing through CO_2 always produce Cherenkov light, whereas for pions there is a momentum threshold of 4.65 GeV/c above which Cherenkov radiation is generated.

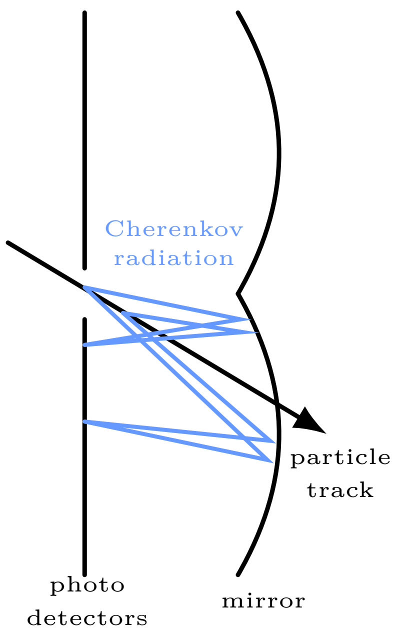

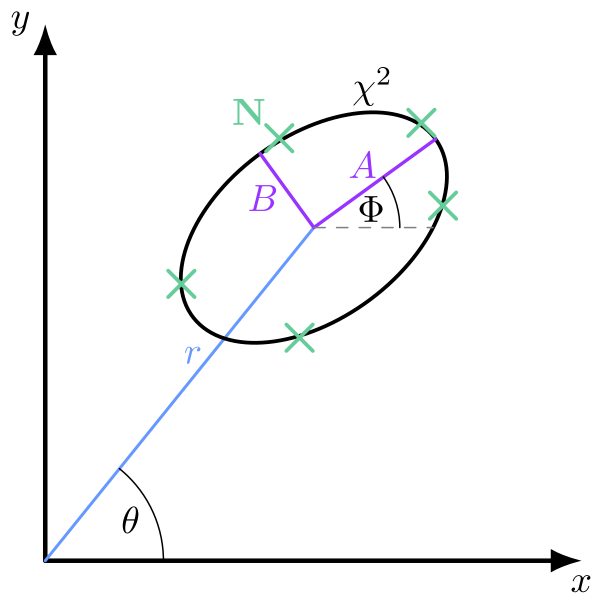

Figure 2.3: Working principle of the RICH. Produced Cherenkov light is mirrored on photon detector planes (a), where it appears as a ring. Thus, rings are detected and fitted with an ellipse providing ellipse parameters and information about the position on the detector plane (b), which are used by an ANN to classify the rings.

A ring-finding algorithm based on the Hough transform is used in a first step to identify ring candidates, which are then fitted with an ellipse. Each ring is matched to the closest extrapolated STS track. Subsequently, an artificial neural network (ANN) is applied. As input, it uses the parameters shown in Fig. 2.3b: the ellipse axes A and B, the rotation angle Φ, as well as the radial position r and radial angle θ on the detector plane. The number of hits N associated with the ring and the χ^2 of the ellipse fit are also included. The distance to the matched track and the corresponding track momentum are used as further input parameters. The ANN is employed to classify the rings, providing an output between -1 and 1, corresponding to the probability of the ring originating from an electron [12].

2.1.4 Transition Radiation Detector (TRD)

The TRD is positioned downstream of the RICH and extends its pion suppression and electron identification to higher momenta. In addition it is used for the identification of nuclear fragments. The TRD consists of four layers of Multi-Wire Proportional Chambers (MWPCs), each equipped with a polyethylene foam radiator in front. The configuration of the chambers in one layer is shown in Fig. 2.4. Four different types of two sizes, $99 \times 99\,\mathrm{cm}^2$ and $57 \times 57\,\mathrm{cm}^2$, are installed. In the inner zone the chambers of type 1 are replaced by different modules, the so-called TRD-2D, to improve the position resolution [13].
The readout chambers are filled with a Xe-CO_2 gas mixture, in which traversing charged particles deposit energy along their trajectory. Additionally, transition radiation (TR) is produced in the radiator when charged particles cross boundaries between materials with different dielectric constants. As the TR production depends on the Lorentz factor γ, electrons at a given momentum produce significantly more TR, than pions and heavier particles. The resulting higher energy deposit for electrons allows an efficient separation from hadrons [14].

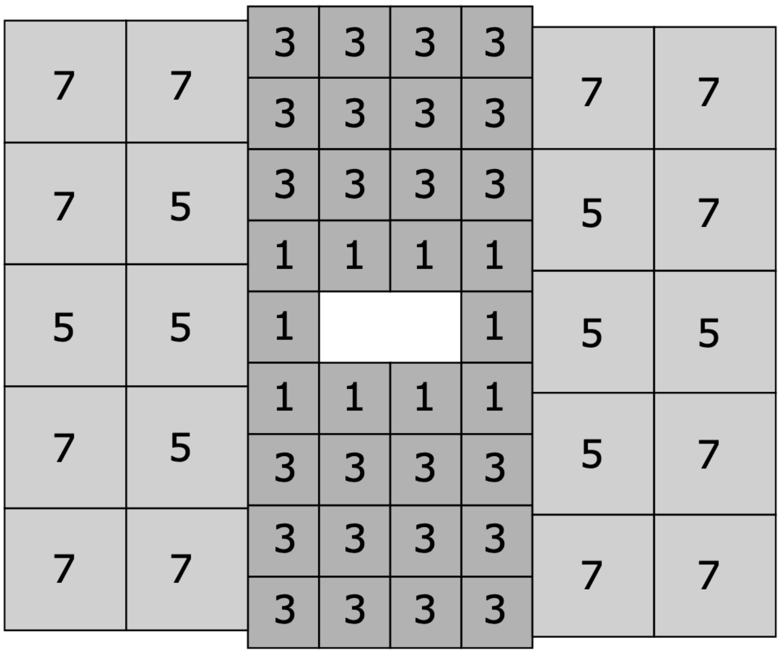

Figure 2.4: Layout of one TRD layer. Four different types of chambers are placed in each of the four layers of the TRD.

2.1.5 Time-of-Flight System (TOF)

The TOF detector consists of 1376 Multi-Gap Resistive-Plate Chambers (MRPCs) arranged in 226 modules of six types, forming a wall with an active area of about $120\,\mathrm{m}^2$. The wall is installed 6 to 10 m downstream of the interaction point.
Using the measured time in the detector t_{MRPC}, and a start time t_0 of the event, the time of flight is obtained as $t_{\mathrm{tof}} = t_{\mathrm{MRPC}} - t_0$. The time resolution is better than 80 ps [15].

2.1.6 Forward Spectator Detector (FSD)

The FSD is designed for event plane reconstruction and centrality measurements. It is positioned behind the TOF and planned to be built out of scintillators. It replaces the former planned PSD [16].

2.1.7 Beampipe

The beam passes through the beampipe to reach the beam dump located 20 m downstream. Currently, three different beampipes are planned, each specifically designed for a particular beam momentum. The different beampipes are listed in table 2.1. To accommodate varying beam momenta, the deflection angle and the beam dump position are adjusted accordingly to compensate for differences in beam deflection in the magnetic field. The deflection of a

Table 2.1: Different beampipes are planned for different beam momenta. The beamdump position and deflection angle are adjusted according to the beam deflection in the magnetic field.

label	P_{beam} AGeV	beam dump position (x, y, z) m	deflection angle
v24e	5.93	(0.68, 0.0, 20.0)	1.89°
v24i	11.00	(0.365, 0.0, 20.0)	1.05°
v24h	12.00	(0.34, 0.0, 20.0)	0.98°

charged particle in a magnetic field is governed by the Lorentz force F_L. This force causes the particle to follow a circular trajectory with radius r, as it provides the required centripetal force for circular motion, expressed as

$$|F_L| = |F_c| \Rightarrow qvB = \frac{pv}{r}\,, \tag{2.1}$$

where p and v denote the particle's momentum and velocity, q is its charge, and B is the magnetic field strength [17, p.287]. From this, the radius of curvature can be written as

$$r = \frac{p}{qB}\,. \tag{2.2}$$

The radius r increases with particle momentum p, and a larger radius corresponds to a smaller deflection angle. Consequently, particles with lower momentum experience stronger deflection.

The design of the different downstream beampipes listed in table 2.1 reflects this behavior. For lower momenta, the deflection angle is greater, and the beam dump's position is shifted away from the center. Fig. 2.5 shows a top view of the beampipes `v24h` and `v24e`, which are adjusted at the red connection point.

When switching to a beam with a different momentum, the magnetic field must be scaled accordingly to maintain the desired deflection angle. According to eq. (2.2), reducing the magnetic field B increases the radius r. Thus tracks are closer together. As a result, the momentum resolution deteriorates with decreasing magnetic field strength, which is shown in appendix A.1 for CBM. For the initial operation phase of CBM, it is planned to use the beampipe `v24h` for the highest beam energy and adjust the magnetic field strength accordingly to avoid any mechanical modifications of the setup.

(a) `v24h`

(b) `v24e`

Figure 2.5: Top view of two different beampipes. The beampipes are designed for beam momenta of $P_{\text{beam}} = 12\,\text{AGeV}$ and $P_{\text{beam}} = 5.93\,\text{AGeV}$. At the red connection point the beampipe is shifted to adjust for the different deflection angle.

2.2 QCD Phase Diagram

Quantum Chromodynamics (QCD) is part of the standard model of particle physics and describes the strong interaction. The strong interaction is mediated by its gauge bosons, gluons, which couple to color charge. Particles carrying color charge, quarks and gluons themselves, constitute strongly interacting matter. As a consequence of gluon self-interactions, quarks are confined within color-neutral hadrons [1, chapter 8.2].

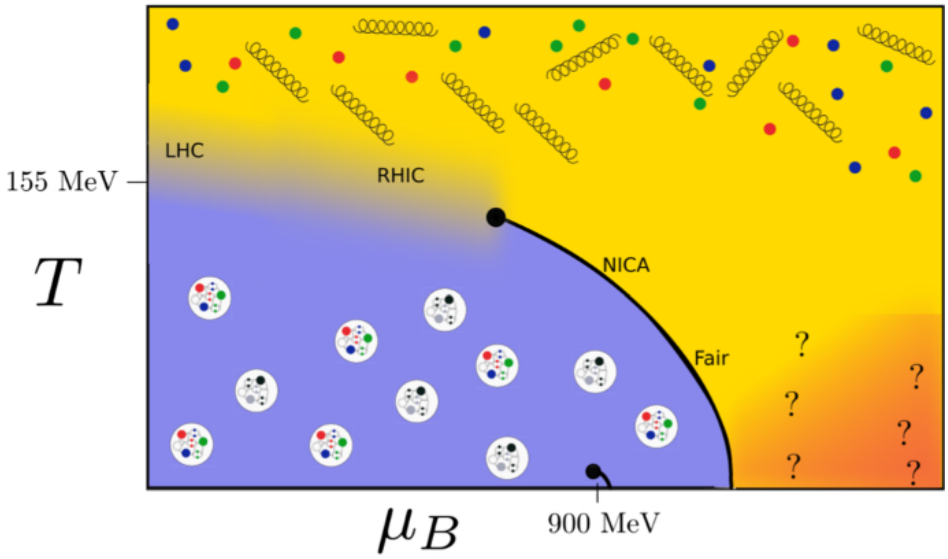

Figure 2.6: QCD phase diagram of strongly interacting matter. The confined state can transition to a deconfined state, the QGP. At low μ_B this change is a smooth crossover, described theoretically by lattice QCD and investigated at the LHC. CBM is being built to investigate high μ_B where a first-order phase transition is expected [18].

The QCD phase diagram shown in Fig. 2.6 maps the states of strongly interacting matter as a function of temperature T and baryochemical potential μ_B, which characterizes the imbalance of baryons and antibaryons. The hadronic state of confined quarks and gluons is shown in blue in Fig. 2.6. For sufficiently high temperatures and/or densities, a deconfined state of matter, the quark–gluon plasma (QGP), can be reached. For vanishing μ_B, the transition between the hadronic phase and the QGP is a smooth crossover [18, 19]. Lattice QCD calculations determine the corresponding pseudocritical temperature to be $T = 156.5 \pm 1.5\,\text{MeV}$ [20]. Conditions in this regime are comparable to those in the early universe shortly after the Big Bang and are probed experimentally, for example, in Pb–Pb collisions at the LHC by the ALICE experiment [18].

At large μ_B, lattice QCD calculations are hindered by the sign problem, but various models predict a first-order phase transition in this region. The endpoint between the first-order transition line and the crossover is the QCD critical point. The CBM experiment at FAIR is designed to investigate this part of the phase diagram [18]. For even higher μ_B, a color-superconducting phase of quark matter is expected [21].

2.3 Heavy-Ion Collisions

In heavy-ion collisions, extreme conditions can be reached to probe different stages of the QCD phase diagram in the laboratory. Two different modes are used to generate heavy-ion collisions. In fixed-target experiments like CBM, ion beams are accelerated and shot onto a

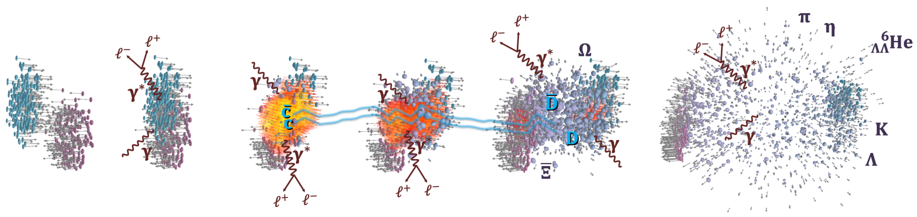

Figure 2.7: Time evolution of a heavy-ion collision. In heavy-ion collisions, two nuclei are collided to reach extremely high densities and temperatures, making it possible to create a deconfined state of matter, the QGP. Dileptons are a particularly useful probe, since they are emitted during all stages of the evolution of the resulting fireball and escape the medium largely undisturbed [6].

target, other than in collider experiments, where two ion beams are accelerated and collided. Due to momentum conservation, collider experiments reach center-of-mass energies $\sqrt{s} = 2E$ with beam energy E, whereas fixed target experiments reach energies $\sqrt{s} \propto E$ [17, p.16 f.]. In return, fixed target experiments allow higher interaction rates [22, p.74]. The reached temperature and μ_B in a heavy ion collision depend on the collision energy. Higher $\sqrt{s}$ leads to higher temperatures but lower μ_B [23].

The evolution of a heavy-ion collision is shown in Fig. 2.7. Before the collision, two Lorentz-contracted nuclei are approaching each other. An important value is the centrality of the collision given by the impact parameter b, which indicates the distance between the centers of the two nuclei. The collision during the overlap of the two nuclei can be described by nucleon–nucleon (NN) collisions. Hard NN collisions with high momentum transfer are rare and happen right at the beginning, and after that, soft NN collisions with lower momentum transfer occur [24].

At high energies as at the LHC, the pre-equilibrium stage thermalizes within $\tau \sim 1\,\text{fm/c}$ into a deconfined state, the QGP [18]. At CBM energies, strong baryon stopping produces high net-baryon densities at moderate temperatures. The evolution is predominantly hadronic. Different models describe a possible mixed phase of a hadron gas and QGP for the existence of a first-order phase transition in this region [25, p.542].

As the fireball expands and cools down, any deconfined phase hadronizes. In the subsequent hadronic stage, inelastic collisions stop at the chemical freeze-out. At this moment, the distribution of particle species is fixed. The hadrons are still colliding elastically until the kinetic freeze-out. At this point also spectra freeze out [2].

2.4 Dileptons in Heavy-Ion Collisions

Dileptons are emitted throughout the entire space–time evolution of the fireball via the decay of virtual photons, $\gamma^* \to e^+e^-$, as illustrated in Fig. 2.7. Since leptons do not participate in the strong interaction, these pairs leave the medium essentially undisturbed and therefore provide a probe of fireball dynamics. At early times, hard collisions lead to Drell-Yan production of dileptons. During the subsequent evolution, thermal radiation from the hot and dense medium generates additional dilepton yield. In the late freeze-out stage, hadronic decays contribute via two-body channels and three-body Dalitz decays, summarized as the freeze-out cocktail [26].

The thermal dilepton emission rate is given by

$$\frac{dN_{ll}}{d^4x\, d^4q} = -\frac{\alpha_{\rm em}^2}{\pi^3 M^2} f_B(q_0;T) \times \frac{1}{3} g_{\mu\nu} \,{\rm Im}\, \Pi^{\mu\nu}_{\rm em,ret}(M,q;T,\mu_B), \tag{2.3}$$

with the electromagnetic coupling constant $\alpha_{\rm em}$, the thermal Bose-Einstein distribution $f_B(q_0;T)$, and momentum q of the dilepton [5]. ${\rm Im}\,\Pi_{\rm em}$ is the electromagnetic spectral function [27], which depends explicitly on the invariant mass M. In the low-mass region (LMR), $M \lesssim 1\,{\rm GeV}$, the dominant contributions arise from light vector mesons ρ, ω, and ϕ, while in the intermediate-mass region (IMR), $1.5 \lesssim M \lesssim 3\,{\rm GeV}$, the main source is quark–antiquark annihilation $q\bar{q} \to e^+e^-$. Medium effects require substantial corrections to the spectral function in the LMR, linking it to chiral symmetry restoration. In the IMR, however, the corrections are comparatively small, making this mass range particularly suitable for extracting an effective temperature of the fireball [5].

The mass dependence is reflected in the expected dilepton invariant-mass spectrum for $\sqrt{s_{NN}} = 3.19\,{\rm GeV}$, shown in Fig. 2.8. At low masses, the spectrum is dominated by the freeze-out cocktail, composed of Dalitz decays and two-body hadronic decays. In the intermediate mass range, however, the thermal contribution becomes dominant. By subtracting the hadronic cocktail from the measured spectrum, one gains access to the thermal radiation in the relevant mass window [26]. A non-relativistic approximation gives

$$\frac{dN_{ll}}{dM} \propto (MT)^{3/2} \exp(-M/T) \tag{2.4}$$

for this mass range [27]. The temperature extracted from the thermal dilepton yield can be used to extend the caloric curve, which relates the fireball temperature to the collision energy. In Fig. 2.9, the caloric curve is shown for low beam energies, with measurements from the HADES and NA60 experiments indicated by black points. For a smooth crossover or purely hadronic scenario, the curve is expected to follow the red dotted line. In the presence of a first-order phase transition, the trajectory between the onset of deconfinement and the

critical point (blue points) is modified, as indicated by the alternative purple path. The CBM experiment will explore this region and may provide insights into the nature of the phase transition [28].
In addition to the temperature, the low-mass region can be used for lifetime measurements and as an indicator for chiral symmetry restoration [29].

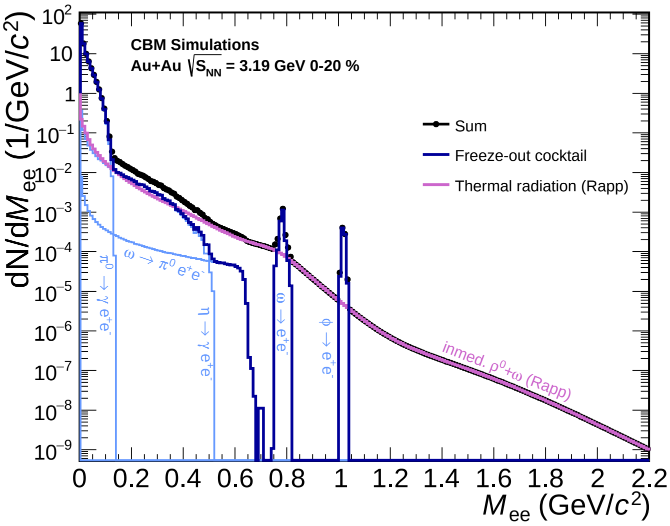

Figure 2.8: Dilepton mass spectrum showing contributions from different sources: freeze-out cocktail at low masses and thermal radiation. By subtracting the hadronic cocktail, the thermal contribution becomes accessible.

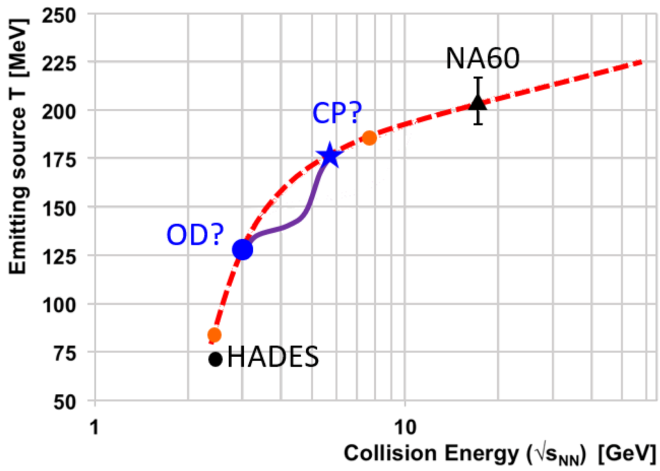

Figure 2.9: Caloric curve for low beam energies. The curve has a different shape between onset of deconfinement (OD) and critical point (CP) if there is a first order phase transition, indicated in purple. CBM probes this region between HADES and NA60 measurements [28].

3 Simulation

To simulate heavy-ion collisions, two event generators are used in this thesis. The Ultra-relativistic Quantum Molecular Dynamics (UrQMD) generator [30] simulates the full collision, while the event generator pluto [31] simulates individual decays that are embedded to improve statistics. The particle generation is described in section 3.1. Subsequently, all particles generated in the collision are transported through the CBM detector using GEANT 3, a simulation software, that describes the passage of particles through matter [32]. This is followed by digitization and reconstruction to obtain the detector response. The used configuration of the CBM experiment setup, the geometry, is explained in section 3.2.

3.1 Particle Generation

The UrQMD model can be used to simulate hadron–hadron, hadron-nucleus, and nucleus–nucleus collisions in the energy range $\sqrt{s_{\mathrm{NN}}} \sim 2$—$200\,\mathrm{GeV}$ [33]. It is a microscopic hadronic transport model that includes 55 baryon species and 32 meson species, together with their antiparticles. Projectile and target nuclei are initialized, and the subsequent space-time propagation and interactions of all hadrons are simulated numerically [34]. The primary output is an ASCII file containing the final-state particles of each event [30]. Using the UniGen converter, this file is converted to ROOT format to facilitate further analysis [35].
In this work central Au+Au collisions with an impact parameter range $b = 0$–$6.71\,\mathrm{fm}$, corresponding to a centrality of 0–20 %, at a beam momentum of $P = 4.41\,\mathrm{AGeV/c}$ are simulated. Additionally, the in-medium modified spectral function of ρ and ω, along with various decays listed in table 3.1, are simulated using the Pluto event generator. Pluto is a Monte Carlo based simulation framework used in ROOT that covers hadronic interactions up to a few GeV. It is an event generator that allows simulation of particle and resonance decay chains [31]. Additionally, pluto provides the PFireball source object, which enables simulation of thermal emission from a fireball-like source, such as that created in heavy-ion collisions [36]. These signal events are embedded into UrQMD events and scaled by their expected yield per event to improve statistics. For embedding into 10 million UrQMD events, exactly one pluto decay is inserted per UrQMD event, distributed as follows: 4 million events of the spectral

function and 2 million each of $\phi \to e^+e^-$, $\omega \to e^+e^-$, and $\omega \to \gamma e^+e^-$ decays. Since the ϕ, ω, and ω Dalitz decays are embedded in 1 out of 5 UrQMD events (2M/10M), their effective yield per event is scaled by a factor of 5 when normalized to the full event sample. The yield of the in-medium modified spectral function receives a scaling factor of 2.5 (4M/10M). Additionally, all yields per event are given for 0–5 % centrality and corrected by a factor of 0.7658 to represent 0–20 % centrality. The calculation of the correction is based on [37] and explained in appendix A.3.

Table 3.1: Decay channels simulated with pluto and embedded in the simulation to increase statistics. The events are scaled by the expected yield per event and by factor 5 since they are only embedded in one of five events. The given yields are for 0–5 % centrality and need a correction by factor 0.7658 to 0–20 % (see appendix A.3). Yield per event and branching ratio are taken from [38].

Decay Channel	Yield per event	Branching Ratio
$\omega \to e^+e^-$	0.3802×5	7.36×10^{-5}
$\omega \to \gamma e^+e^-$	0.3802×5	7.70×10^{-4}
$\phi \to e^+e^-$	0.0314×5	2.97×10^{-4}

3.2 Geometry

As described in section 2.1.7, different beampipes are available, but none is dedicated to the beam momentum of interest for this thesis $P_{\text{beam}} = 4.41\,\text{AGeV/c}$. The beampipe `v24e` is designed for $P_{\text{beam}} = 5.93\,\text{AGeV/c}$, which is the closest to the target momentum, while for the first measurement campaigns, it is planned to use the beampipe `v24h`, designed for top energy $P_{\text{beam}} = 12\,\text{AGeV/c}$. For both beampipes, the magnetic field needs to be scaled down since they were designed for higher energies. Otherwise, the spectators would collide with the beampipe downstream, as the deflection angle changes with momentum. The magnetic field scaling factor s is given by the ratio of the new magnetic field B_{new} to the design value of the beampipe B_{bp}. To determine appropriate settings, eq. (2.2) is used. The charge $q = Z$ is fixed by the beam species and the total momentum is $p = P_{\text{beam}} \cdot A$. The radius r remains constant as it is determined by the beampipe geometry. For the same ion species, both A and Z are constant and can be disregarded, yielding

$$B = \frac{p}{qr} = \frac{P_{\text{beam}} \cdot A}{Z \cdot r} \quad \Rightarrow \quad B \propto \frac{P_{\text{beam}} \cdot A}{Z} \quad \Rightarrow \quad B \propto P_{\text{beam}}. \tag{3.1}$$

The scaling of the magnetic field is therefore given by the ratio of the desired momentum P_{new} to the beampipe design momentum P_{bp}:

$$s = \frac{B_{\text{new}}}{B_{\text{bp}}} = \frac{P_{\text{new}}}{P_{\text{bp}}} = \frac{4.41}{5.93} \approx 0.74 \quad \text{and} \quad \frac{4.41}{12} \approx 0.37. \tag{3.2}$$

To verify these scaling factors, beam transport simulations are performed starting 3 m upstream, outside the magnetic field region. In Fig. 3.1a (left), a side view of the detector setup is shown using the `v24e` beampipe with magnetic field scaling of 0.74. Secondary particles are shown in pink and yellow. These secondaries appear in front of the magnet and at the end of the beampipe. Interactions with air and target generate secondaries in front of the magnet, while in the actual detector volume, no secondaries are observed, but they appear at the end of the beampipe instead. This indicates that the beam passes through the beampipe cleanly without interaction and reaches the beam dump. Additionally, the top view on the right side of Fig. 3.1a shows that the beam is well centered within the beampipe. Similar results are obtained for the `v24h` beampipe with magnetic field scaling of 0.37 in Fig. 3.1b.
Each configuration is used for simulations in this thesis to compare results and assess the performance of the dilepton analysis. The two different setups are summarized in table 3.2. Besides the beampipe, the FSD must be adapted, and the magnetic field scaling adjusted accordingly. Unlike described in section 2.1.4, the geometry `v20b_1e` does not include the TRD-2D modules in the inner zone, as the TRD-2D software is still under development (see appendix A.2).
In this simulation, a 250 μm thick target is used. For the CBM experiment, a $10 \times 25\,\mu$m segmented target is planned. The effect of the different target is discussed and corrected for in section 4.5.

Table 3.2: Geometry configurations for the two setups. Tags correspond to CBMROOT geometry versions. For different beampipes, the magnetic field is scaled according to eq. (3.2) and the FSD is adapted.

	setup `v24h`	setup `v24e`
magnet	v22a	v22a
pipe	v21d:v24h	v21d:v24e
mvd	v20d_tr	v20d_tr
sts	v22d	v22d
rich	v25a	v25a
trd	v20b_1e	v20b_1e
tof	v21a_1e	v21a_1e
fsd	v25h	v25e
platform	v22b	v22b
fieldTag	v22c	v22c
Scaling	0.37	0.74

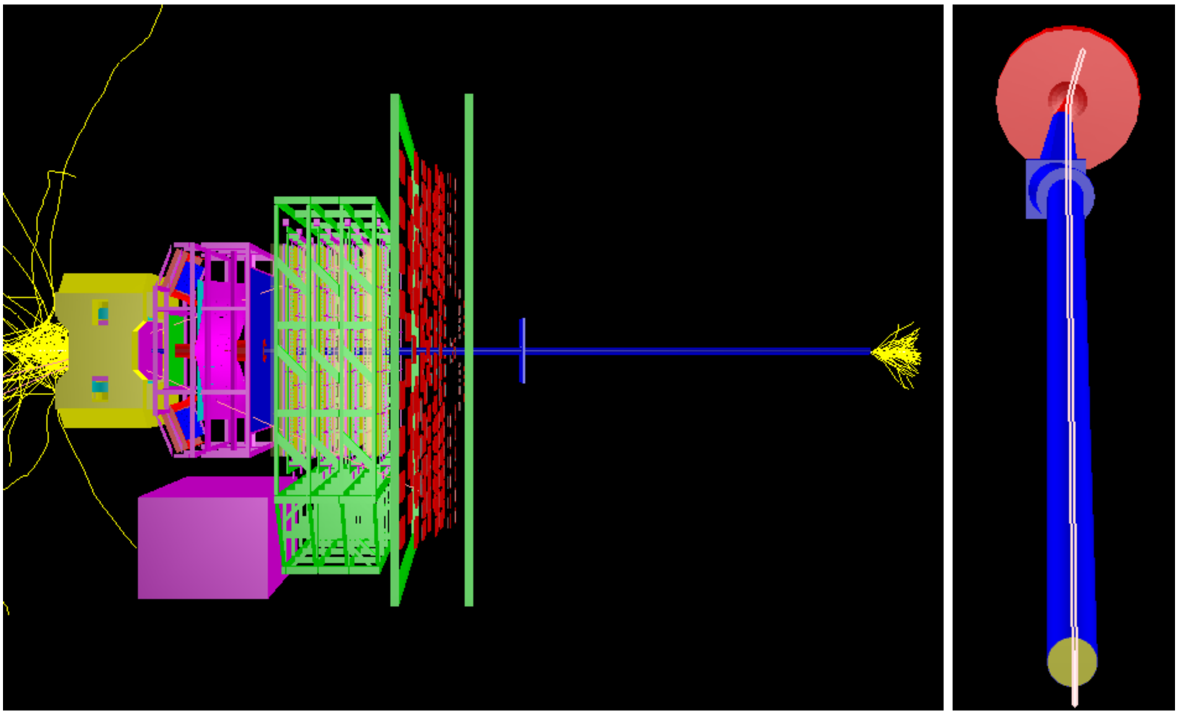

(a) Beampipe `v24e` with magnetic field scaling 0.74.

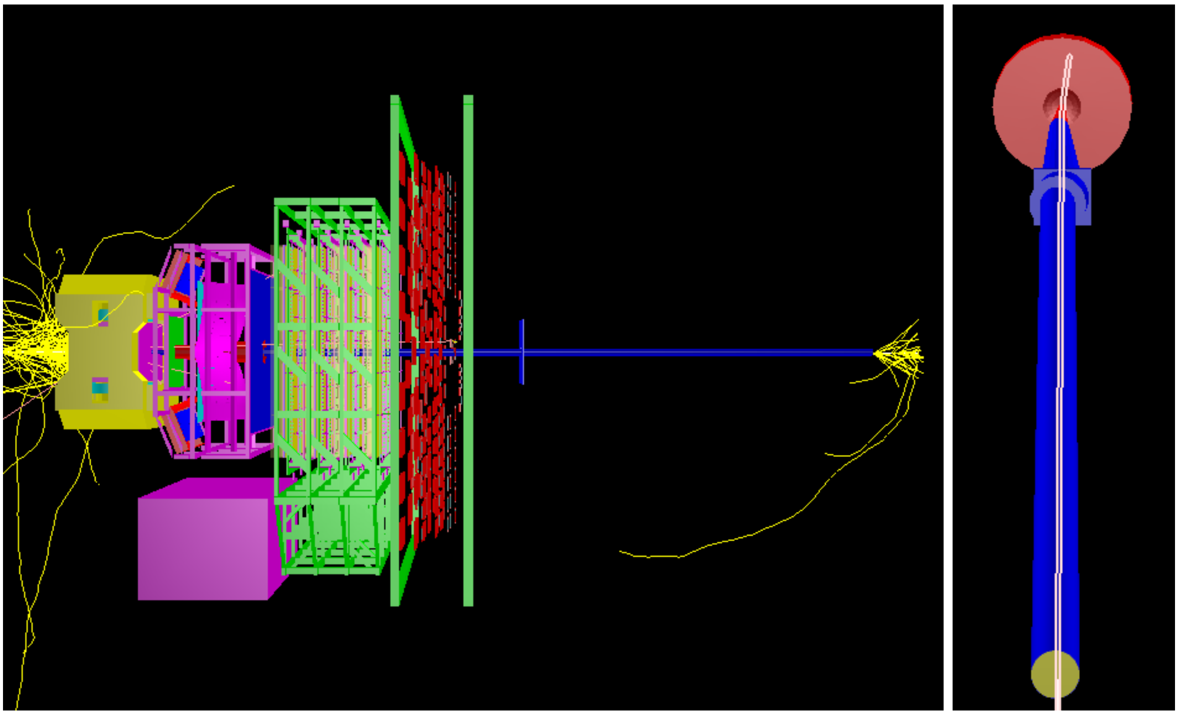

(b) Beampipe `v24h` with magnetic field scaling 0.37.

Figure 3.1: Beam transport simulations for beampipe configurations `v24e` (a) and `v24h` (b). No secondary particles are visible within the detector volume (side views), indicating clean beam passage. The beam is well centered within the beampipe (top views) and reaches the beam dump successfully.

4 Dilepton analysis

For the analysis, the Pair Analysis Framework PAPA in CBMROOT is used. Originally developed by Julian Book based on a dielectron framework for the ALICE experiment, it was further extended in [39] by Etienne Bechtel and in [6] by Adrian Meyer-Ahrens. The goal of the analysis is to obtain an invariant mass spectrum by combining all positively and negatively charged tracks from each event. As explained in section 2.4 the mass spectrum can be used to access the thermal radiation.

In Fig. 4.1a, a schematic drawing shows one event, in which different positive and negative particle tracks originate from the primary vertex. These include electrons and positrons, as well as positive and negative pions, protons, and kaons, which constitute the hadronic background. To obtain a mass spectrum, the invariant mass of each opposite-charge pair must be calculated. Since the origin of the tracks can not be distinguished further, all possible opposite-charge pairs are considered. Thus every positive track is paired with every negative track. In Fig. 4.1b, an example is shown where an electron track is paired with each positive track. Among these pairs, there is one true pair marked and additional incorrect pairs with other positive tracks, which constitute the so-called combinatorial background. Tracks without a true partner, as shown in Fig. 4.1c, contribute exclusively to the combinatorial background.

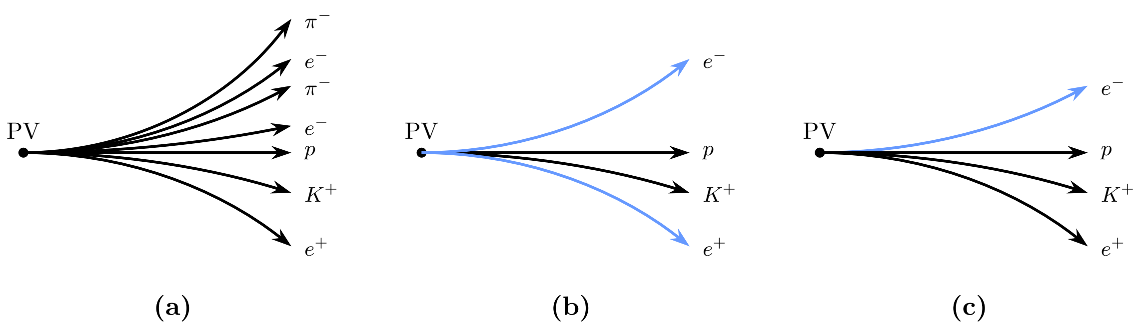

Figure 4.1: Schematic drawing of particle tracks in one event. Tracks originating from the primary vertex (PV) include electrons/positrons and hadronic background particles (a). All possible opposite-charge pairs are formed, resulting in true signal pairs and combinatorial background (b). Tracks without true partners contribute only to combinatorial background (c).

In Fig. 4.2, the particle composition of reconstructed tracks before analysis is shown for both setups defined in section 3.2. Monte-Carlo (MC) information is used to classify the particle species and as in the following, positively and negatively charged particles are summarized, like elctrons and positrons as electrons. The signal consists of electrons from pluto-generated decays, while UrQMD electrons originate from π^0 and η Dalitz decays. The relevant background comprises two components: hadrons misidentified as electrons, and electrons not contributing to the signal, namely those from photon conversions in detector materials. The particle composition differs for the two setups in the number of tracks, in particular for electrons, with higher counts in the `v24h` setup. Due to the higher magnetic field in the `v24e` setup, more particles are bent out of the detector acceptance which affects low momentum tracks up to $\sim 0.4\,\mathrm{GeV/c}$. While the main electron contribution is below $0.4\,\mathrm{GeV/c}$, the hadron momentum distributions peak at higher momenta, which is why the effect is relatively higher for electrons (compare Fig. A.4).

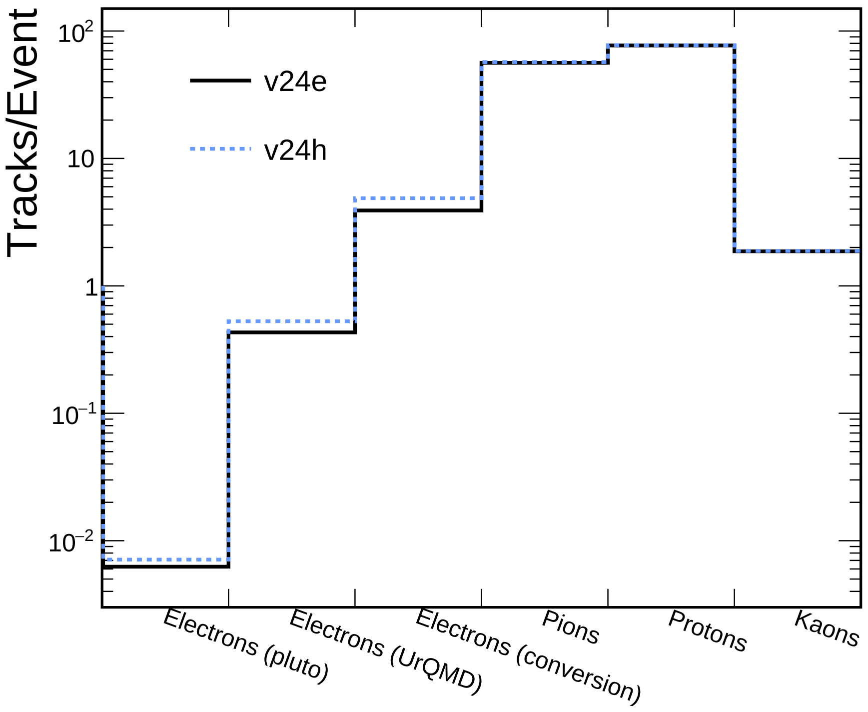

Figure 4.2: Particle species composition before analysis for the two different setups. Besides signal electrons there are various background contributions constituting electron and hadronic background. Due to the stronger bending in the `v24e` setup, there are more tracks in the acceptence of the `v24h` setup.

The goal of the analysis is to suppress this background, which is particularly important due to the combinatorial background. The number of possible opposite-charge pairs scales with the product of positive and negative track multiplicities

$$SE^{+-}\left(N^{+},N^{-}\right) = N^{+}\cdot N^{-}. \tag{4.1}$$

Decomposing the track counts into signal and background contributions $N^{\pm} = N_S^{\pm} + N_B^{\pm}$,

$$SE^{+-} = N_S^{+}N_S^{-} + N_S^{+}N_B^{-} + N_B^{+}N_S^{-} + N_B^{+}N_B^{-}, \tag{4.2}$$

reveals that the number of pairs grows roughly quadratically with the number of background tracks $N_B^{+}N_B^{-}$ [6].
To reduce the background in PAPA, a series of different rejection cuts is applied to events, tracks, or pairs. First, event cuts reject entire events (e.g., by centrality). Track cuts are then applied to individual positive and negative tracks (e.g., momentum, number of hits in detectors). To apply pair cuts, all possible opposite-charge pairs are formed and cuts are applied to their combined attributes like invariant mass. This is not the exclusive order, because the order also affects efficiencies. For example, track cuts applied before pair cuts can reduce the number of true pairs available for pair selection.
In [6], the dielectron pair analysis was performed for $P_{\text{beam}} = 12\,\text{GeV/c}$ and implemented in PAPA. Here, the cuts are applied in the same order and the cut sequence is identical for both beampipe configurations. An overview of the cuts is shown in table A.1. First, track quality cuts ensure that tracks have sufficient hits in multiple detectors and reach the outer detectors. Subsequently, hadron suppression and electron background reduction are achieved through dedicated cuts, as explained in section 4.1 and section 4.2, respectively.

4.1 PID Cuts

To reduce the hadronic background, particle identification (PID) cuts are applied using information from different detectors. As described in section 2.1.3 and 2.1.4, RICH and TRD are specifically designed for pion suppression. However, the STS and TOF detectors also provide valuable information for hadron rejection. The following sections describe the individual PID cuts for each detector. For each cut, the performance is evaluated comparing the momentum distribution before and after the cut, along with the corresponding suppression factor across the momentum range. The cuts were tuned using a sample of 4 million UrQMD events including embedded dielectrons from the in-medium modified spectral function of ρ and ω (see section section 2.4). The resulting momentum spectra, suppression factors, and efficiencies are then shown for the full 10 million UrQMD events with the sources described in section 3.1 embedded. The single cuts are explained and evaluated for the `v24e` setup, but were equally implemented for the `v24h` setup. Each plot shown for the `v24e` setup, is shown in appendix A.5 for the `v24h` setup. In section 4.1.5 the results of the cuts are evaluated and compared for the two different beampipe configurations.

4.1.1 RICH Cut

In the RICH detector, electrons produce Cherenkov light which is detected as rings on the photon detector plane, as described in section 2.1.3. To reject particles other than electrons, two selection cuts are applied. First, only tracks associated with a reconstructed ring in the RICH, i.e. with more than five hits, are accepted. This "ring cut" is designed to reject tracks which did not produce Cherenkov light, corresponding to all particles except electrons, as well as pions above the pion Cherenkov threshold in CO_2.

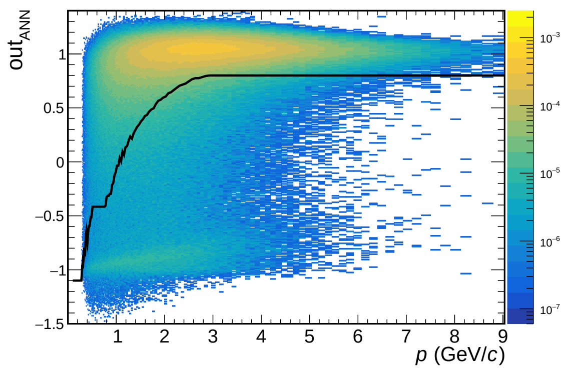

(a) Electrons

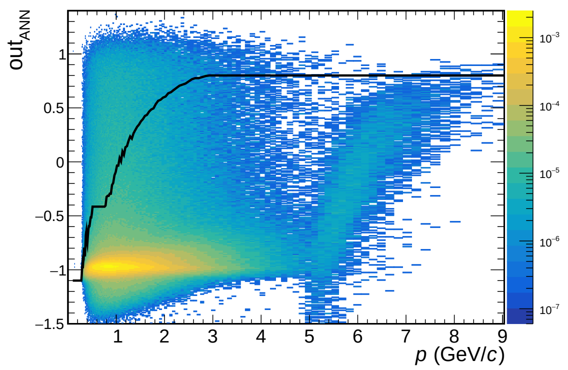

(b) Pions

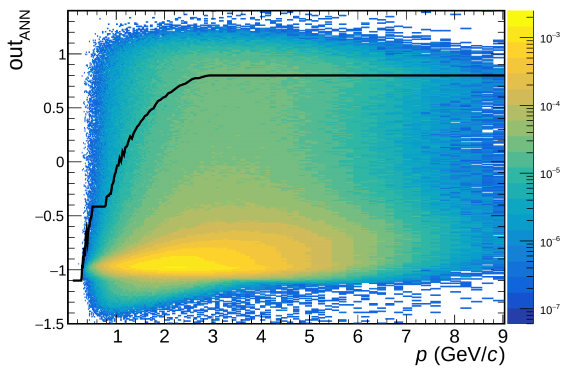

(c) Protons

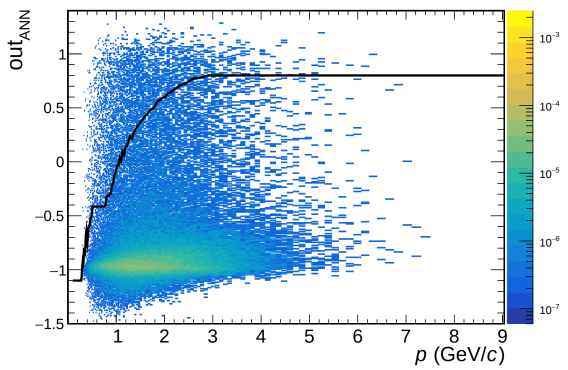

(d) Kaons

Figure 4.3: ANN output as a function of the momentum for electrons, pions, protons, and kaons. The output is ranging from about -1 to 1, where 1 is the classification as an electron. The black line marks the applied cut corresponding to the chosen electron efficiency.

In Fig. 4.3, the ANN output after applying the ring cut is shown for electrons, pions, protons, and kaons. The output ranges from approximately -1 to 1. Entries for all particle species indicate mismatches between tracks and rings, showing that ring–track association alone does not entirely remove non-electron tracks. In Fig. 4.3a, many electron tracks have ANN outputs close to 1 and are thus correctly classified as electrons. However, especially at low momenta, some electron tracks cannot be reliably classified because the ring parameters, particularly the ring-to-track distance, change significantly (compare Fig. A.5). For protons, kaons, and pions, the majority of tracks has ANN output near -1, enabling their rejection. For pions, an increase in ANN output is observed above 5 GeV, corresponding to the Cherenkov threshold at 4.65 GeV, above which pions also produce rings. At higher momenta the ANN output for pions further increases because their rings become less distinguishable from those of electrons.

To reject remaining non-electron tracks, a cut on the ANN output is applied. The corresponding ANN threshold is indicated by the black line in Fig. 4.3. Tracks with outputs below this threshold are rejected. The electron efficiency is fixed in momentum bins and set to 80 % up to about 1 GeV/c and 90 % up to 3 GeV/c, as shown in Fig. 4.4. Above 3 GeV/c the cut is kept constant at 0.8. This fixed threshold still rejects most pion tracks while achieving even higher electron efficiency. The pion distribution in Fig. 4.3b suggests that enforcing an efficiency of 90 % does not significantly improve the pion suppression. This results in an momentum integrated electron efficiency of 87.72 %, which is dominated by the large contribution of low momentum tracks.

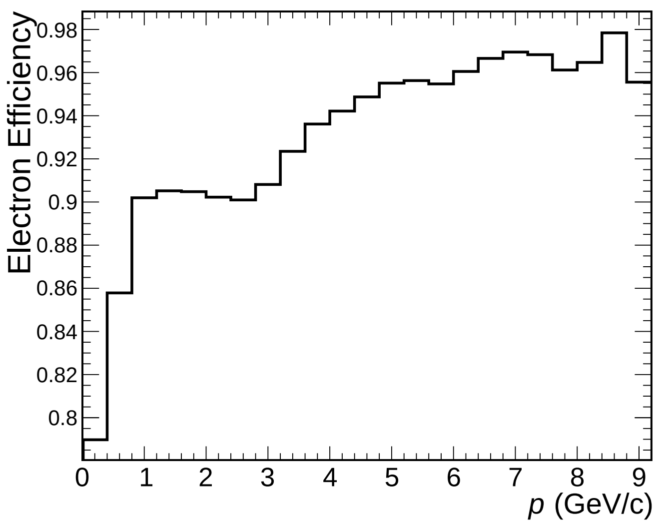

Figure 4.4: Electron efficiency as a function of momentum for the RICH ANN cut. Efficiency is fixed at 80 % up to 1 GeV/c and 90 % up to 3 GeV/c. Above 3 GeV/c, the constant ANN threshold of 0.8 yields an even higher efficiency.

Figure 4.5 shows the momentum distribution before any RICH cuts, after the ring cut, and after the ANN cut. For kaons and protons, the ring cut reduces the number of tracks across the full momentum range. For pions, however, rejection deteriorates above $\sim 5\,\mathrm{GeV}$. The suppression factors in Fig. 4.6a reflect this: kaons and protons reach 30–40 across all momenta, while pions show no suppression above $5\,\mathrm{GeV/c}$. This behaviour is a consequence of the pion Cherenkov threshold. Once the threshold is exceeded, pions also emit Cherenkov light and form rings in the RICH, making pion tracks indistinguishable from electron tracks based on the ring cut alone.

For all particle species, the ANN cut reduces tracks across the entire momentum range, which is also visible in the suppression factors shown in Fig. 4.6b. For pions, the suppression increases above $5\,\mathrm{GeV/c}$ because more pion tracks pass the ring cut but are rejected by ANN, since the rings they produce can be distinguished from the ones created by electron tracks with the same momentum. The combined suppression in Fig. 4.6c reaches values up to 10^3 over the full momentum range.

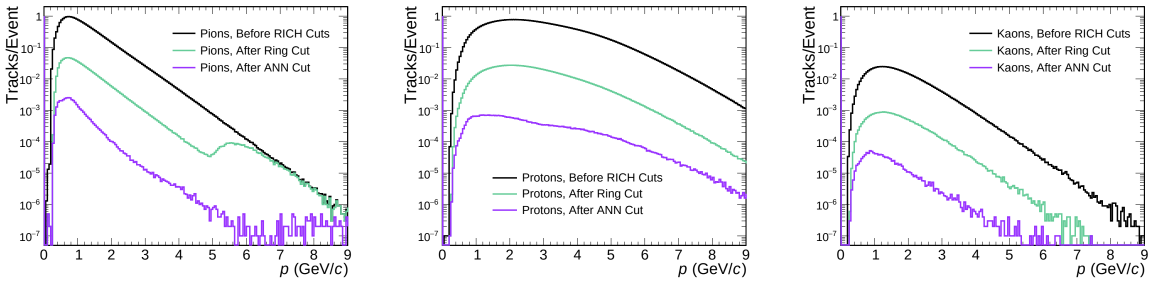

(a) Pions **(b)** Protons **(c)** Kaons

Figure 4.5: Momentum distribution for pions (a), protons (b), and kaons (c), before any RICH cuts, after the ring cut, and after the ANN cut. For kaons and protons, the number of tracks is reduced across the full momentum range by both cuts. For pions, the ring cut reduces tracks only up to about $5.5\,\mathrm{GeV/c}$, because pions above their Cherenkov threshold of $4.65\,\mathrm{GeV/c}$ also produce rings.

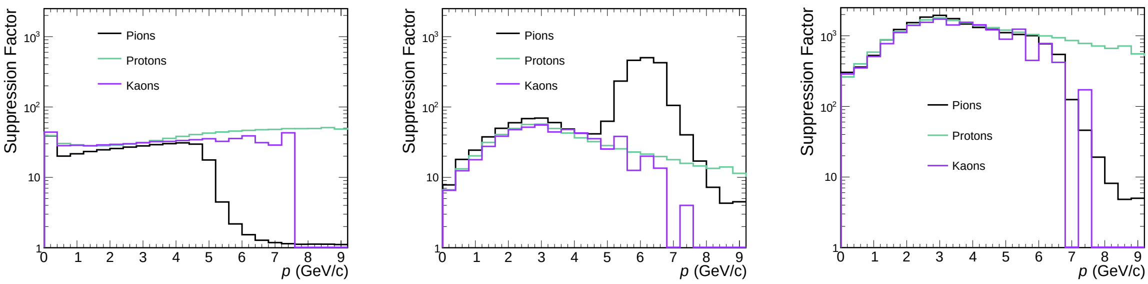

(a) Ring Cut **(b)** ANN Cut **(c)** Combined

Figure 4.6: Suppression factors as a function of momentum for the ring cut (a), the ANN cut (b), and the combination of both (c) for pions, protons, and kaons, respectively. The pion Cherenkov threshold is visible because pion suppression is dominated by the ANN cut at high momenta, while proton and kaon suppression remains almost constant over the entire momentum range for both cuts.

4.1.2 TRD Cut

Using the energy loss in the TRD, a likelihood L_e for a particle being an electron is calculated. The likelihood is defined as

$$L_e = \frac{P_e}{P_e + P_\pi + P_P + P_K} \qquad \text{with} \qquad P_j = \prod_{i=1}^{N} (E_i|j), \qquad j \in \{e, \pi, p, K\}, \tag{4.3}$$

where P_j is the probability that a track is of type j, given by the product over the probability of all N hits of the track depositing the measured energy E_i in the detector layer for particle j [14].

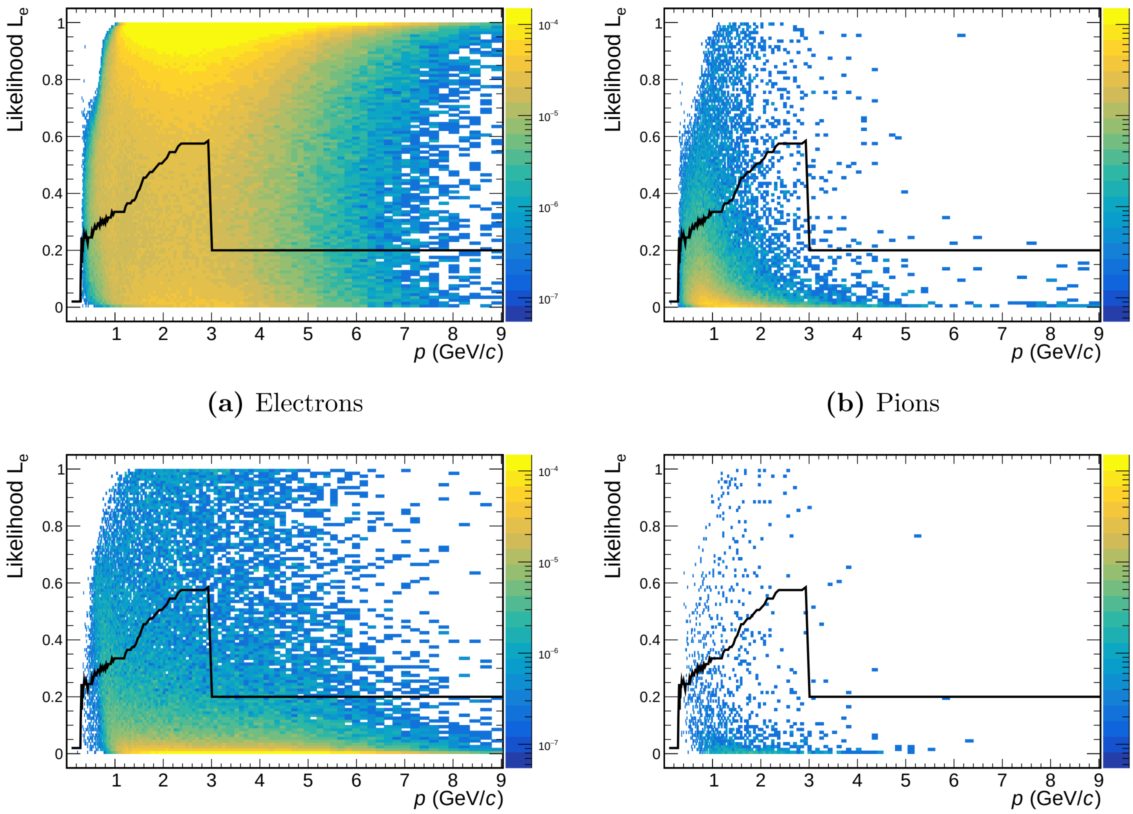

(a) Electrons **(b)** Pions

(c) Protons **(d)** Kaons

Figure 4.7: Electron likelihood L_e as a function of momentum for electrons, pions, protons, and kaons. The black line shows the applied cut corresponding to a fixed electron efficiency of 70–80 % up to 3 GeV/c. Above this, the constant $L_e = 0.2$ threshold increases electron efficiency while maintaining pion suppression.

The likelihood as a function of momentum is shown in Fig. 4.7 for electrons, pions, protons, and kaons. At low momenta, some electrons have low likelihood values because little transition radiation is produced in this regime. As for the RICH Cut, the electron efficiency is fixed in momentum bins, and the applied cut is marked in black in Fig. 4.7. The electron efficiency shown in Fig. 4.9a is set to 70 % below 1 GeV/c, since in this region many pion and proton tracks can be rejected with a tighter cut. Up to 3 GeV/c, the efficiency is set to 80 %. For $p > 3\,\mathrm{GeV/c}$, the rejection cut is kept constant at $L_e = 0.2$. This value is tuned to the pion likelihood distribution at high momenta. It removes most remaining pion tracks, as visible in Fig. 4.7b, while yielding an electron efficiency above 90 %, as seen in Fig. 4.9a. Again, the momentum integrated efficiency of 73.53% is dominated by the low momentum contribution.

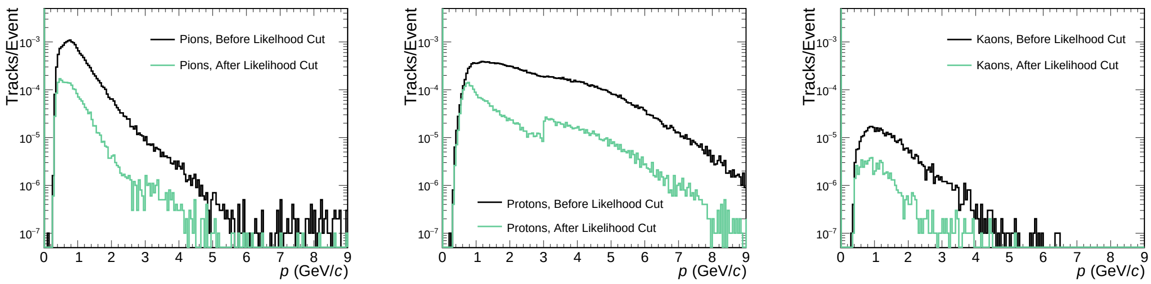

(a) Pions **(b)** Protons **(c)** Kaons

Figure 4.8: Momentum distributions before and after TRD cut for pions, protons, and kaons. Track suppression is visible above $\sim 0.4\,\mathrm{GeV/c}$ across all hadron species.

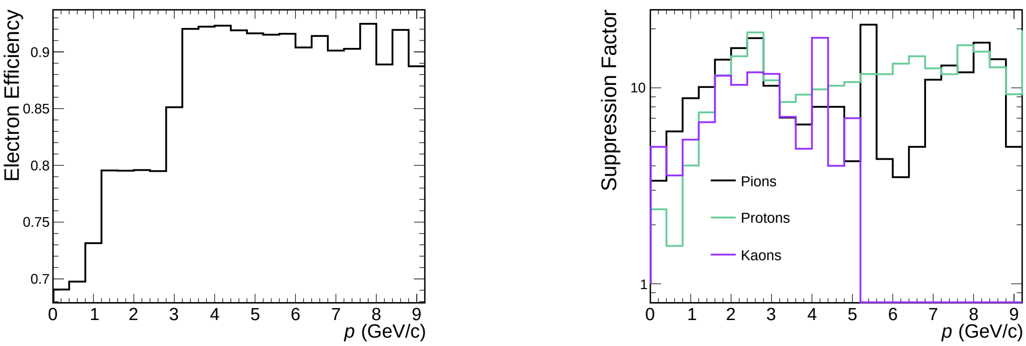

(a) Electron efficiency as a function of momentum.

(b) Suppression factors for pions, protons, and kaons as a function of momentum.

Figure 4.9: Electron efficiency and corresponding hadron suppression achieved with the TRD likelihood cut. The efficiency is fixed at 70 % at low and 80 % at intermediate momenta.The constant cut ($L_e = 0.2$) at high momenta yields an electron efficiency above 90 % while maintaining pion suppression.

The momentum distributions in Fig. 4.8 show that pions, protons, and kaons are suppressed across the whole momentum range, most clearly above $p \approx 0.4\,\mathrm{GeV/c}$. At 3 GeV/c, where the cut value is fixed, a visible change in the proton distribution appears. Since protons are rejected by subsequent cuts, the focus here is on pion rejection. For pions, the effect of the fixed cut is less pronounced because statistics at high momenta are limited. The suppression factors in Fig. 4.9b confirm this behaviour. Suppression is present at all momenta, increases up to 3 GeV/c, remains effective at higher momenta due to transition radiation, and provides good electron–hadron separation even at low momenta. Still, the TRD cut suppresses protons by factor ~ 10 above 3 GeV/c. Therefore it is an important tool for proton suppression at high momenta.

4.1.3 TOF Cut

Using the measured time in the TOF detector t_{TOF} and the distance of the TOF layer to the target d_{TOF}, the particle velocity β can be calculated as

$$\beta = \frac{v}{c} = \frac{d_{\mathrm{TOF}}}{t_{\mathrm{TOF}} - t_0} \cdot \frac{1}{c}. \tag{4.4}$$

For a particle with rest mass m and momentum p,

$$\beta = \frac{p}{\sqrt{m^2 + p^2}} \tag{4.5}$$

applies. To identify a particle as an electron, the difference $\Delta\beta_{\mathrm{electron}}$ is computed between the velocity β measured with the TOF detector and the expected β assuming the electron mass m_e and the reconstructed track momentum p_{track}:

$$\Delta\beta_{\mathrm{electron}} = \beta_{\mathrm{track}} - \beta_{\mathrm{electron}} = \frac{d_{\mathrm{TOF}}}{t_{\mathrm{TOF}} - t_0} \cdot \frac{1}{c} - \frac{p_{\mathrm{track}}}{\sqrt{m_e^2 + p_{\mathrm{track}}^2}}. \tag{4.6}$$

For true electrons, $\Delta\beta_{\mathrm{electron}} \approx 0$ should hold, since the measured and expected β values coincide. Figure 4.10 shows the $\Delta\beta_{\mathrm{electron}}$ distribution for electrons, pions, protons, and kaons. For electrons it is centered around 0, while the heavier particles exhibit negative shifts due to their mass dependence according to eq. (4.5). At fixed momentum, larger masses correspond to smaller β, with this effect diminishing at high momenta. This mass dependence is most pronounced for protons and least for pions. Due to TOF hits of faster particles which are falsely matched to hadron tracks, mismatches around $\Delta\beta_{\mathrm{electron}} = 0$ remain for all particle species. To reject tracks incompatible with the electron hypothesis, a cut on $\Delta\beta_{\mathrm{electron}}$ is applied. Tracks deviating too far from 0 are rejected, and only those with $\Delta\beta_{\mathrm{electron}} > -0.005$ are accepted, as indicated by the black line in Fig. 4.10.

The momentum distributions in Fig. 4.11 for pions, protons, and kaons are shown before and after the cut. Due to the mass dependece, pions are only reduced below $p \approx 2$ GeV/c. For protons and kaons, however, a reduction over the whole momentum range is visible, although for kaons the effect is small because only few kaon tracks remain already before the cut. The suppression factor in Fig. 4.12 shows again the mass dependence for pions. They are only

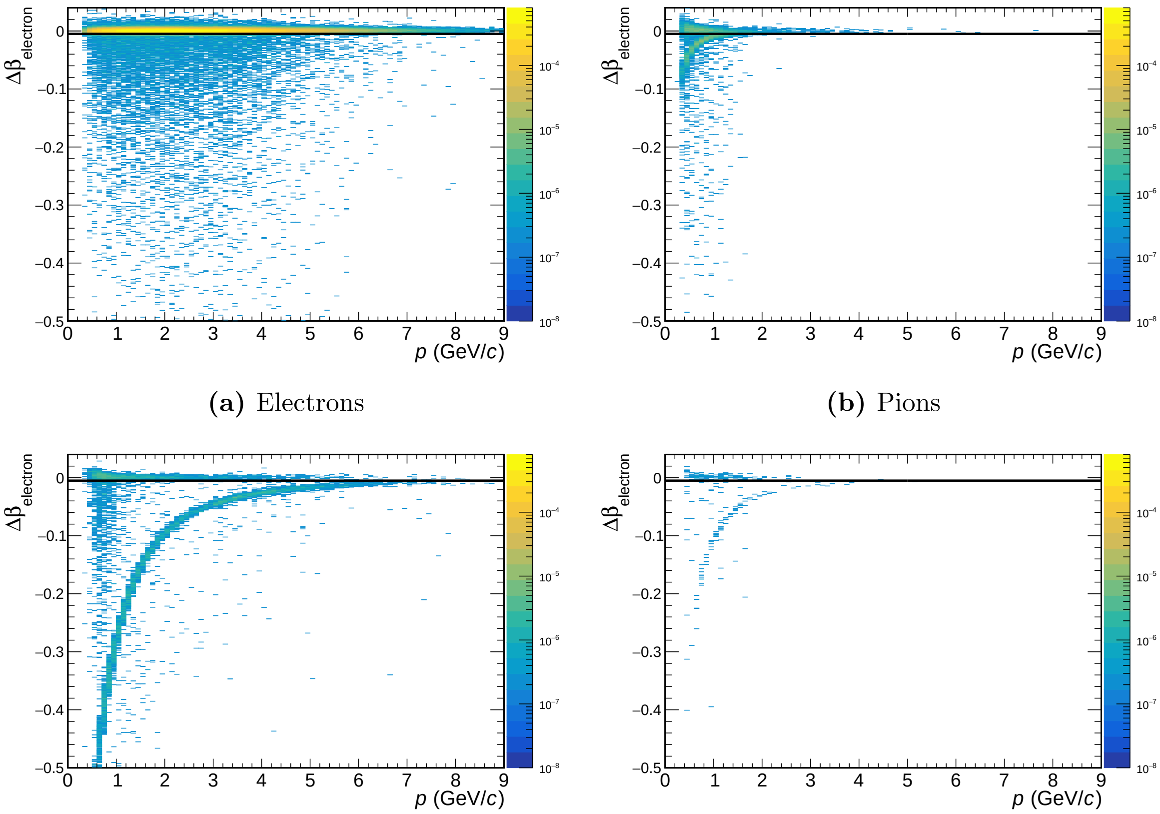

(a) Electrons **(b)** Pions

(c) Protons **(d)** Kaons

Figure 4.10: Difference $\Delta\beta_{\text{electron}}$ as function of momentum, shown for electrons, pions, protons, and kaons. The β values calculated from TOF information are compared with those expected from track momentum assuming the electron mass. The difference $\Delta\beta$ is shown for electrons, pions, protons, and kaons. Since $\Delta\beta = 0$ is expected for electrons, a cut is applied, rejecting tracks with $\Delta\beta > -0.005$. Because β depends on the mass, $\Delta\beta_{\text{electron}}$ approaches 0 with increasing momentum, and the effect is stronger for heavier particles.

suppressed for low momenta, while kaons are suppressed across the full momentum range of remaining tracks up to 4 GeV/c. The apperant increase of proton suppression above 3 GeV/c is caused by the preceding TRD cut. In Fig. 4.10c, the momentum distribution before the TOF cut clearly shows the step introduced by the TRD cut at 3 GeV/c. However, the TOF cut contributes to proton suppression across the whole momentum rang. Overall, the cut reaches an electron efficiency of 97.09%

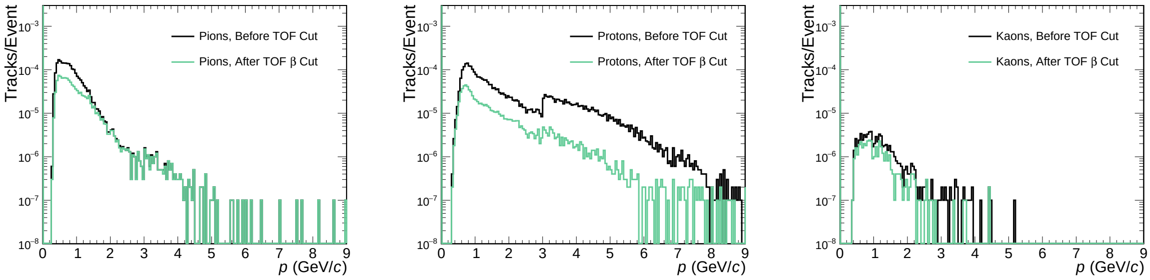

(a) Pions (b) Protons (c) Kaons

Figure 4.11: Momentum distributions before and after the TOF cut for pions, protons, and kaons. The number of protons is reduced across the whole momentum range, similar to kaons, although kaon statistics are already low prior to the cut. Due to their low rest mass, pions are only suppressed for $p < 2\,\mathrm{GeV/c}$.

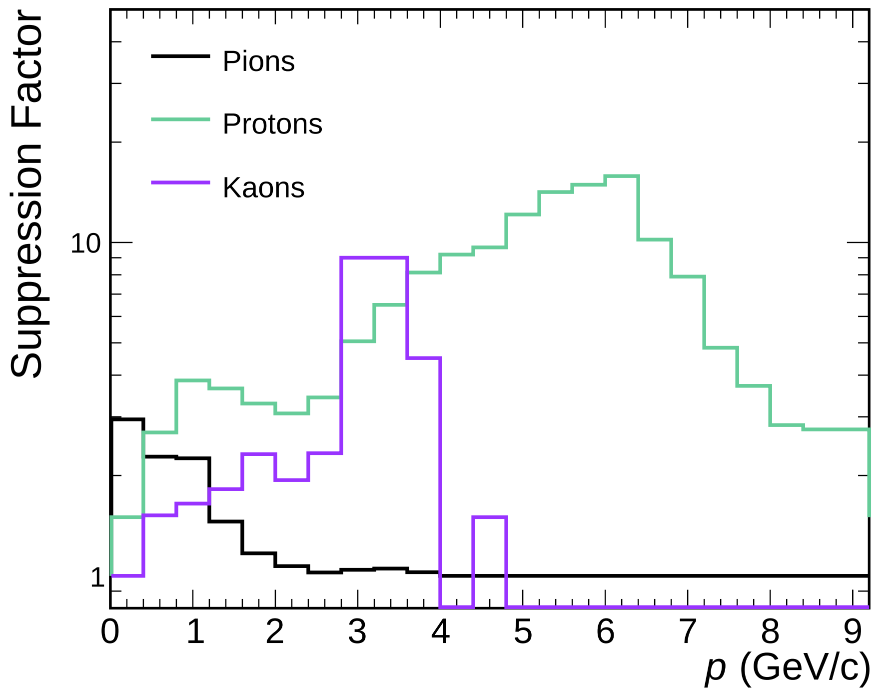

Figure 4.12: Suppression factors from the TOF cut as a function of momentum. Due to the mass dependence in eq. (4.5), the strongest suppression is observed at low momenta. Kaons and protons are suppressed over nearly the entire momentum range of the remaining tracks, whereas pions are only suppressed below $2\,\mathrm{GeV/c}$.

4.1.4 STS Cut

For the STS, the median energy deposit of electrons, protons, kaons, and pions is shown in Fig. 4.13. Protons, and to a lesser extent kaons, exhibit a larger energy loss at low momenta. As shown in the figure, a cut is applied along the upper edge of the electron distribution to suppress these particles. Below 2 GeV/c, tracks with $dE/dx_{\mathrm{STS}} > 3.2 \times 10^4\ e/300\ \mu$m are rejected.

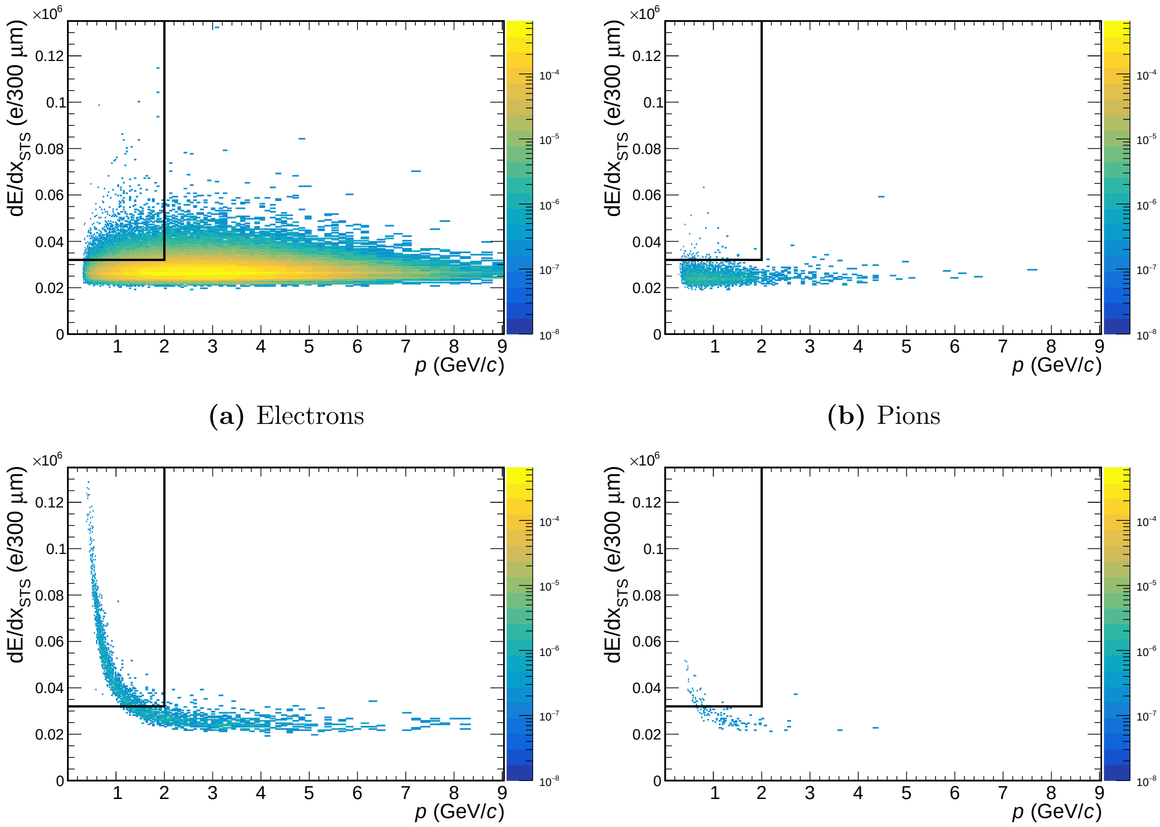

(a) Electrons **(b)** Pions

(c) Protons **(d)** Kaons

Figure 4.13: Energy loss in the STS layers as a function of momentum for electrons, pions, protons, and kaons. For protons and kaons, the energy loss in silicon is higher at low momenta compared to electrons. A cut is applied along this edge, rejecting tracks with $dE/dx_{STS} > 3.2 \times 10^4\ e/300\ \mu$m for $0 < p < 2$ GeV/c marked in black.

The momentum distribution of protons in Fig. 4.14b demonstrates that this cut reduces the number of protons up to about 2 GeV/c and kaons up to 0.7 GeV/c, while it has no visible effect on pions. For kaons below 0.6 GeV/c even all remaining tracks are rejected, which is why the suppression factor Fig. 4.15 for kaons in the first bin can not be calculated. Other than that, the suppression factor shows the same results. There is no suppression for pions, while for kaons suppression is evident below 1 GeV/c. The number of protons is reduced up to 2 GeV/c, with a suppression factor reaching 10^3 below 1 GeV/c. At higher momenta there is no suppression, which is a consequence of the shape of the energy-loss distribution and the fact that the cut is only applied below 2 GeV/c. The reached electron efficiency is 95.24 %.

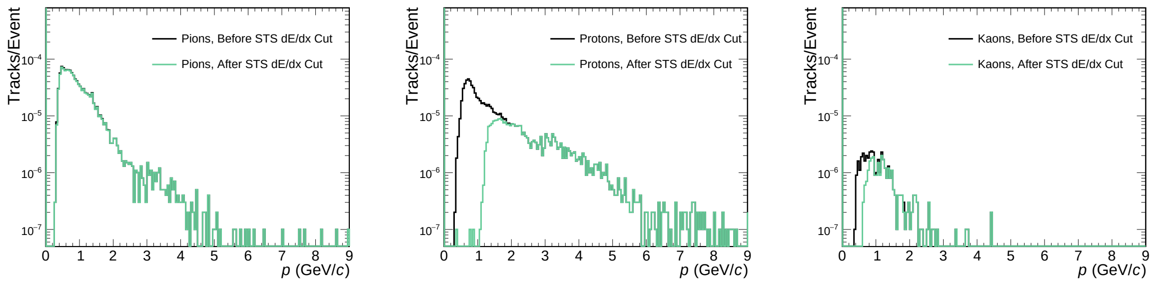

(a) Pions **(b)** Protons **(c)** Kaons

Figure 4.14: Momentum distributions before and after the STS cut for pions, protons, and kaons. The number of protons and kaons is reduced up to 2 GeV/c and 1 GeV/c, respectively, while there is no visible effect for pions.

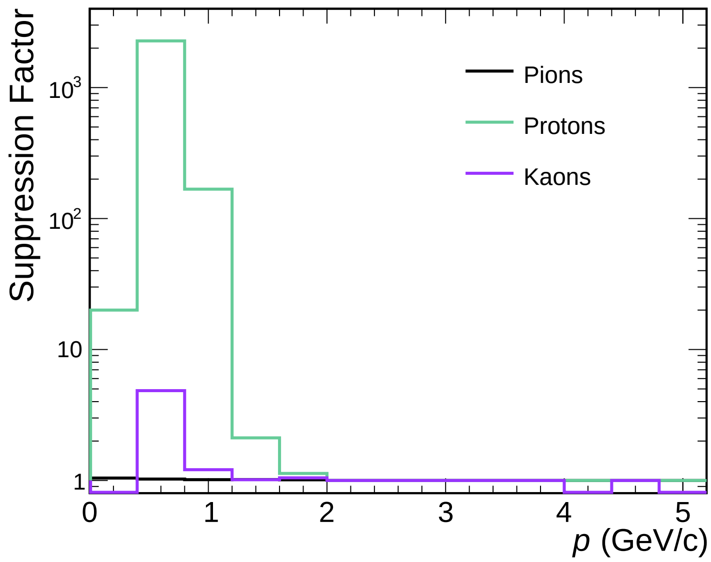

Figure 4.15: Suppression factor as a function of momentum for the STS cut. Protons and kaons at low momenta are suppressed by the STS cut, while there is no effect on pions because the energy loss in silicon differs from that of electrons only for protons and kaons at low momenta. The suppression factor in the first bin for kaons can not be calculated since all kaons are rejected.

4.1.5 Combined Results

In Fig. 4.16, the particle species distributions before and after the PID cuts are shown for the two setups v24e and v24h. For both setups, pions, protons, and kaons are strongly suppressed, while electrons are only moderately reduced. As a consequence, in the both setups fewer kaon tracks remain than pluto electrons, while pions are still more numerous than signal electrons and protons about the same amount. In general, the comparison shows that for each particle species there are more tracks in the v24h setup, both before and after applying the PID cuts. After the cuts this difference is even more pronounced for hadrons, indicating that the PID cuts are more effective in the v24e setup.

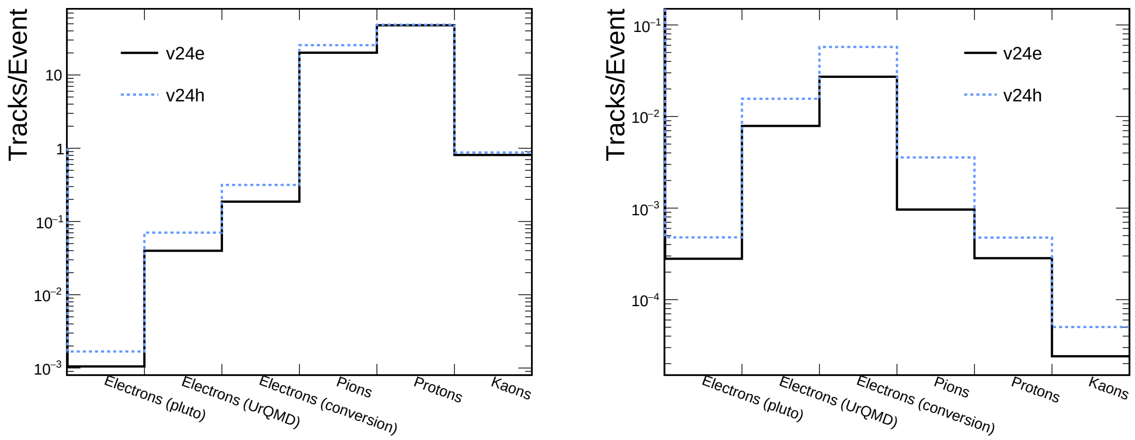

(a) Before PID cuts **(b)** After PID cuts

Figure 4.16: Particle species composition before and after the PID cuts for the two beampipe configurations v24e and v24h.

The PID selection comprises the RICH, TRD, TOF, and STS PID cuts described above and, in addition, two reconstruction cuts, requiring at least one TOF hit and at least three TRD hits. Since these reconstruction requirements are applied within the PID chain, they are also evaluated here. To quantify the impact of the different cuts, table 4.1 and table 4.2 list the momentum integrated suppression factors for each cut step in the order in which they are applied for the two setups. Suppression is given not only for the hadrons, but also for the different electron sources: pluto, UrQMD, and conversion. A different cut order would in principle change the suppression factors of individual cuts.
For the v24e setup, the combined results in table 4.1 show that pions, protons, and kaons are suppressed by factors of 18664, 157574, and 30187, respectively, while pluto electrons are reduced only by a factor of 3.10, corresponding to an electron efficiency of 32.36 %. Comparing to the results obtained with the same cuts in [6, p.80], the hadron suppression is improved by a factor of about 2–3, and the electron efficiency is higher for all electron sources. The higher

electron efficiency is expected, since the RICH and TRD cuts are tuned to higher electron efficiencies in this work. The reason for the higher suppression can be that there are less high momentum tracks due to the lower beam momentum. Therefor the low-momentum sensitivity of the TOF and STS cuts has a larger impact on the momentum-integrated suppression. In particular, the proton suppression is much higher (50361 in [6]). As pointed out before, the TRD cut is an important tool to suppress high momentum protons, but also the STS cut reduces the protons above 3 GeV/c. Especially the STS cut performs better at high momenta in comparison to [6], which is not expected to be related to the used beam energy. Since software and hardware are still under development, the matching of the tracks to TOF hits could have improved, which reduces mismatches.

In general, careful tuning of the cuts allows good results but requires effort for each beam configuration. For this reason, [6] also explored a machine-learning approach, which further improved hadron suppression; applying such methods at $P_{\text{beam}} = 4.41\,\text{GeV/c}$ would be a possible next step.

Table 4.1: Momentum integrated suppression factors for the different cut steps for the `v24e` beampipe.

Cut step	Pions	Protons	Kaons	e (pluto)	e (UrQMD)	e (conversion)
recRICH	22.18	31.59	28.99	1.22	1.20	1.26
pidRICH2d	23.82	37.36	25.42	1.14	1.14	1.15
recTRD	2.24	1.84	2.58	1.52	1.43	1.56
pidTRD2d	7.45	7.23	6.09	1.36	1.35	1.39
recTOF	1.00	1.00	1.00	1.00	1.00	1.00
pidTOF	2.07	3.89	1.75	1.03	1.03	1.03
STS dE/dx	1.02	2.58	1.49	1.05	1.05	1.05
combined	18667	157630	30187	3.10	2.82	3.41

The separation of the suppression into individual cuts in table 4.1 shows that the TOF reconstruction cut requiring one TOF hit has no effect on the suppression. Requiring one hit in the TRD already implies one TOF hit. The largest suppression of electrons occurs in the TRD cuts. For the recTRD cut this is an effect of the TRD acceptence and for the PID cut this is consistent with the PID tuning to relatively low electron efficiency and supports the choice of fixing a likelihood cut at high momenta, since this cut clearly has a strong impact. For both TRD cuts, the suppression is still larger for hadrons than for electrons, which confirms their usefulness. Nevertheless, the PID cut is already tuned and hard to improve. In contrast, the requirement of at least three TRD hits may offer room for optimization.

All the other PID cuts provide a slight suppression of pluto electrons while clearly reducing hadrons. The very small pion suppression factor of 1.02 in the STS cut reflects the nature of this cut which mainly targets protons and kaons at low momenta. The relatively small kaon suppression (1.75 in TOF, 1.49 in STS) is limited by statistics, since the number of remaining kaon tracks is already low, leaving little room for further improvement. Overall, the cuts are well tuned, and the resulting electron efficiency is reasonable given the achieved hadron suppression.

Table 4.2: Momentum integrated suppression factors for the different cut steps for the `v24h` beampipe.

Cut step	Pions	Protons	Kaons	e (pluto)	e (UrQMD)	e (conversion)
recRICH	20.96	25.17	22.92	1.26	1.21	1.34
pidRICH2d	13.59	34.02	21.87	1.16	1.15	1.18
recTRD	2.07	1.76	2.47	1.38	1.31	1.37
pidTRD2d	4.08	6.29	4.93	1.41	1.39	1.46
recTOF	1.00	1.00	1.00	1.00	1.00	1.00
pidTOF	2.44	3.41	1.64	1.04	1.04	1.05
STS dE/dx	1.13	3.02	1.64	1.06	1.05	1.06
combined	6649	97848	16339	3.14	2.77	3.51

Comparing these results to the suppression achieved with the `v24h` setup in table 4.2 shows, that for similar overall electron efficiency, the hadron suppression is worse for all three hadron species, and in particular for pions, where the total suppression is lower by about a factor of three. Figure 4.17 compares the momentum distributions for pions, protons, and kaons before and after the PID cuts for both setups. Before the cuts, more low-momentum hadrons are present in the `v24h` setup for each hadron. Due to the lower magnetic field, low-momentum particles are less likely to be bent out of the detector acceptance and therefore remain in the sample. After the cuts, only a few proton and kaon tracks remain due to the strong STS suppression at low momenta, but for the surviving tracks the `v24h` setup still shows larger yields over the whole momentum range. For pions, the difference at low momentum after the cuts shown in Fig. 4.17d is particularly pronounced. The reduced pion suppression in the `v24h` setup can be traced back mainly to the RICH and TRD cuts since STS and TOF cuts are designed for protons and kaons. In Fig. 4.18 the suppression factors for the RICH and TRD cuts are compared for the two setups. The pion suppression of the ring cut is lower in the first two momentum bins. This means that in this region are more mismatches of pion tracks to rings. Rings are matched to tracks by extrapolating from the STS using the reconstructed momentum. Thus, the reduced momentum resolution at lower magnetic field leads to a worse matching of the RICH rings. Also the recTRD cut yields a lower pion suppression at low momenta, which is an acceptence effect due to the different bending in the magnetic field. The ANN and Likelihood cut have a lower pion suppression across the whole momentum range.

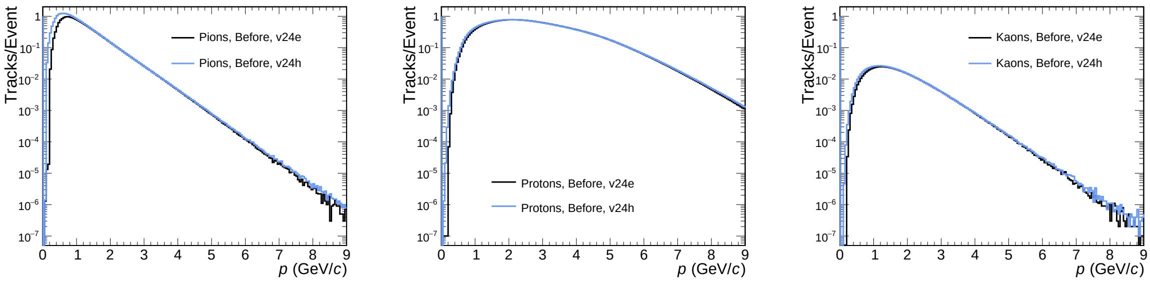

(a) Pions, before (b) Protons, before (c) Kaons, before

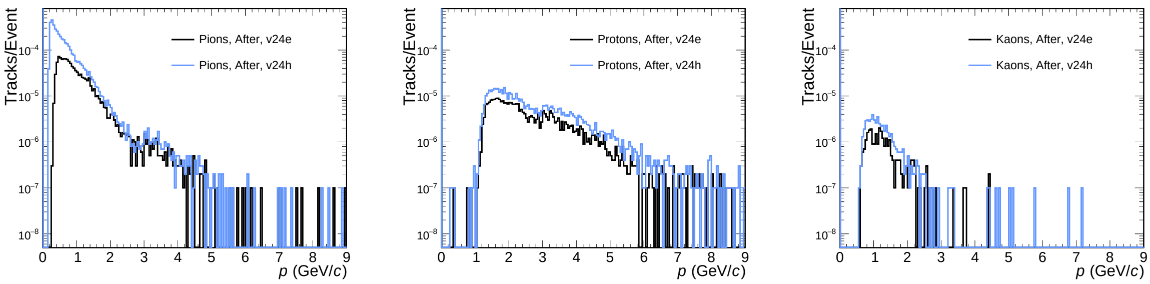

(d) Pions, after (e) Protons, after (f) Kaons, after

Figure 4.17: Momentum distribution before (top row) and after (bottom row) the PID cuts for pions, protons, and kaons, comparing the two beampipe configurations. For protons and kaons the suppression is worse across the whole momentum range in the `v24h` setup. For pions, the region below 1 GeV/c is particularly affected.

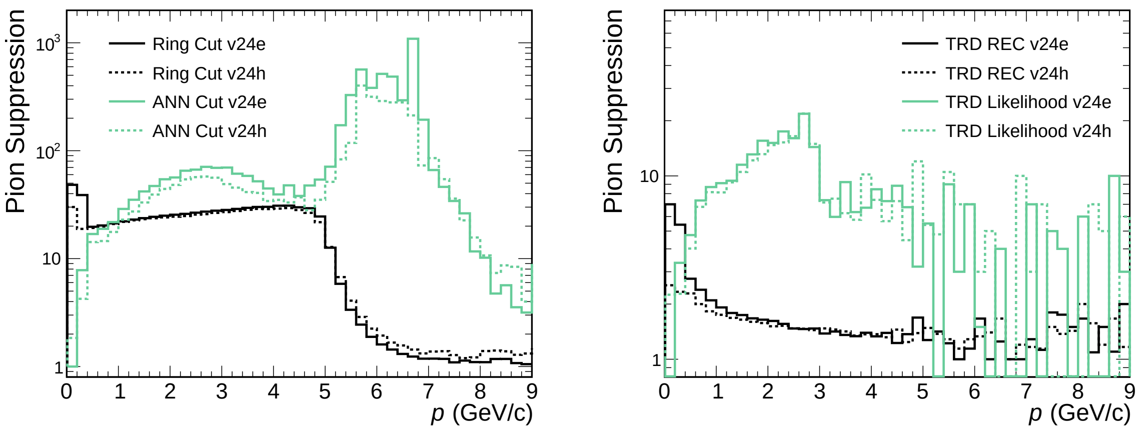

(a) RICH (b) TRD

Figure 4.18: Pion suppression of the RICH and TRD cut compared for the two different setups.

Fig. 4.19 shows the RICH ANN output and TRD Likelihood distributions integrated over the momentum range $0 < p < 2\,\mathrm{GeV/c}$ for electrons and pions compared for the two setups. The focus on the low momentum region remains since this is the dominating region for the integrated suppression. For pions in Fig. 4.19a and Fig. 4.19c the additional pions in the `v24h` setup distribute over the full range of output values. For electrons (Figures 4.19a and 4.19c), however, the distributions are shifted to lower values of L_e and $\mathrm{out}_{\mathrm{ANN}}$ in the `v24h` setup. Fixing a similar target electron efficiency therefore leads to a lower cut value and thus to worse hadron suppression. In the case of the TRD, this shift may be caused by reduced transition

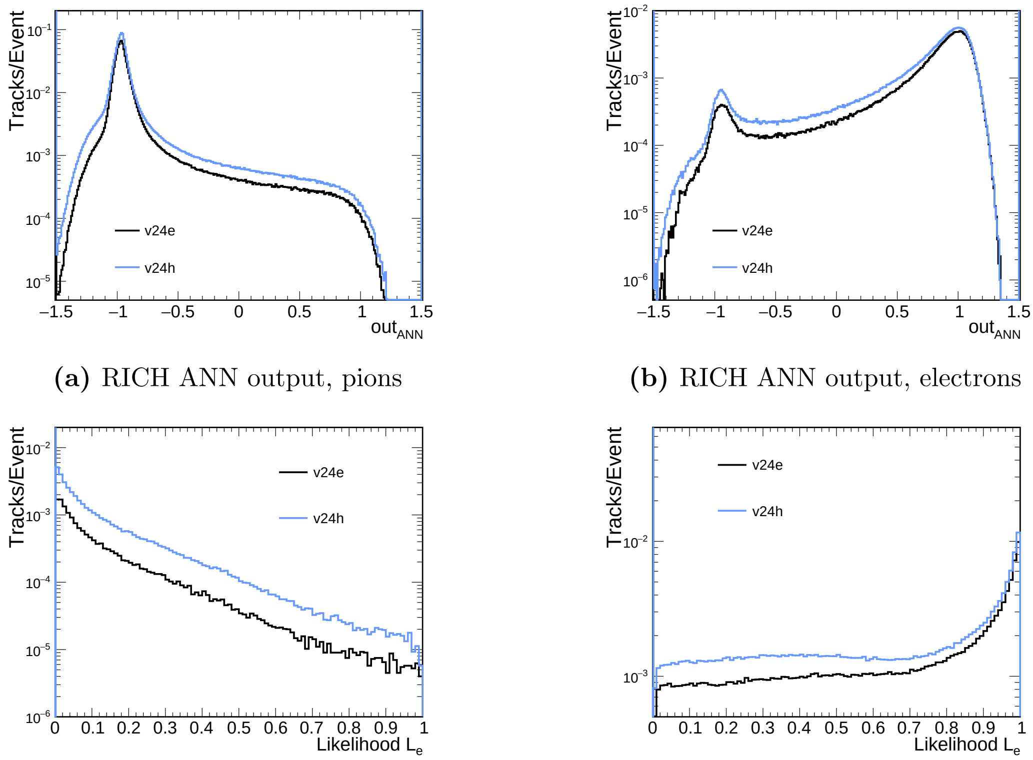

(a) RICH ANN output, pions

(b) RICH ANN output, electrons

(c) TRD likelihood, pions

(d) TRD likelihood, electrons

Figure 4.19: RICH ANN output and TRD likelihood distributions integrated over $0 < p < 2\,\mathrm{GeV/c}$ for electrons and pions in the two setups. In the `v24h` configuration, the electron distributions are shifted to lower values, which reduces the achievable pion suppression at fixed electron efficiency.

radiation at low momenta. Hence with more low-momentum pions and electrons present, their separation becomes more difficult. For the RICH, the ANN used for ring classification was trained for $P_{\mathrm{beam}} = 12\,\mathrm{GeV/c}$ and full magnetic field. Changing to lower beam energy and reduced magnetic field can degrade its performance. This is particularly relevant for the `v24h` configuration, where the magnetic field is even lower. Additionaly, also the RICH ANN cut performs worse at low momentum due to the ring-to-track distande as already discussed in section 4.1.1 and shown in Fig. A.5 which particularly affects the `v24h` setup.

4.2 Electron Cuts

In addition to the signal electrons, there are two main sources of electron background. First, electrons from photon conversions are produced in detector material via $\gamma \rightarrow e^+e^-$. Second, incomplete pairs arise from electrons that do not have an opposite-charge partner in the particle cocktail and therefore contribute only to the combinatorical background, as illustrated in Fig. 4.1. Conversion electrons can also appear as incomplete pairs. Both background sources and their suppression are described in the following.

4.2.1 Conversion Electrons

Conversion electrons are produced in the detector material and can appear along the entire detector. In Fig. 4.20, an example of a photon conversion in the last MVD layer is shown. Two conversion electrons are created and travel through the full detector, being measured by STS, RICH, TRD, and TOF. They should not be rejected by the PID cuts, since they are electrons traversing all PID detectors. To reduce conversion electrons, their invariant mass and their position in the detector is used.

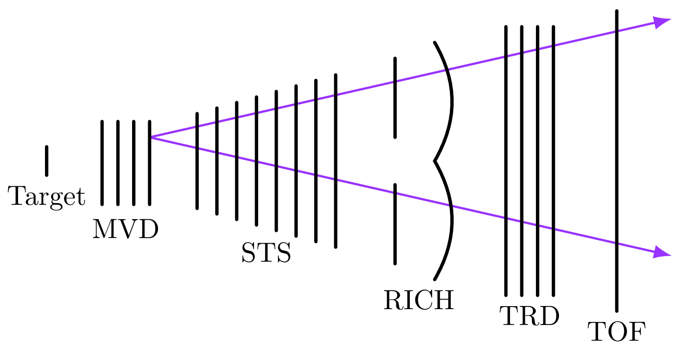

Figure 4.20: Sketch of the production of conversion electrons in the last MVD layer.

First, a cut on the invariant mass can be applied, since electron pairs from conversions are characterized by low invariant mass. For that, all possible pair candidates are used. As explained in [6, chapter 5.3.2.1], the position of this cut is crucial. On the one hand, to calculate a valid invariant mass, both tracks should be electrons, which is the case only after the PID cuts. On the other hand, if other cuts are applied first, it can happen that one partner is already rejected and random combinations with other tracks pass the threshold. In [6], the optimal position of this cut was determined, and the same procedure is used here. First, a cut requiring at least one hit in the TRD is applied to reduce low-momentum particles and thus random combinations that would later be rejected by the invariant mass cut. Then a cut $M_{\mathrm{inv}} < 0.025\,\mathrm{GeV}$ is applied. The momentum distributions before and after this cut are shown in Fig. 4.21 for pluto and conversion electrons. Both are slightly reduced, with conversion electrons being suppressed up to about 4 GeV/c. In table 4.3, the efficiency of the different cuts for electrons from UrQMD, pluto and conversions are listed. For the invariant mass cut, the efficiencies are 84.52% for pluto and 87.36% for conversions in the `v24e` setup. Even though the efficiency for pluto electrons is slightly lower, the cut is an important tool to suppress conversion electrons.

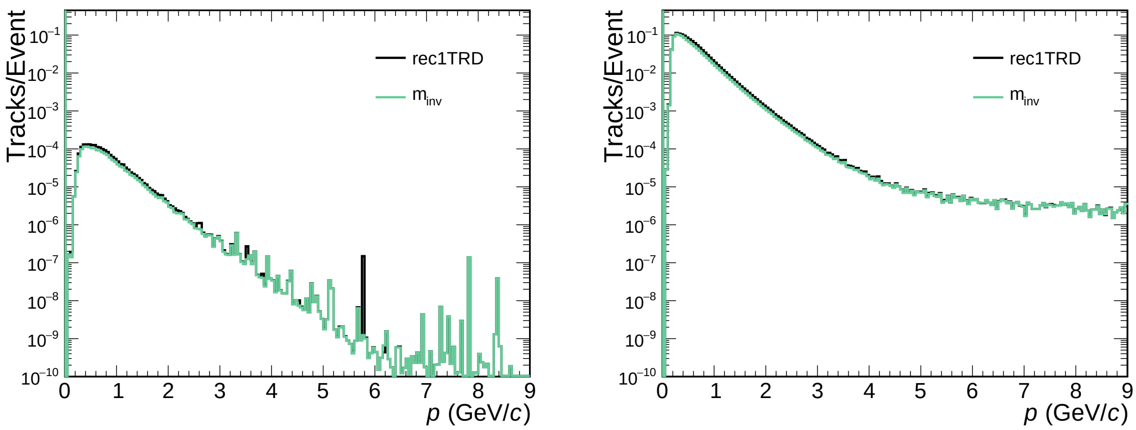

(a) Pluto electrons

(b) Conversion electrons

Figure 4.21: Momentum distribution of pluto electrons and conversion electrons before and after the invariant mass cut.

In the `v24h` setup, the pluto efficiency is lower and the conversion efficiency drops further to 68.95 % and 71.85 %, respectively, again due to the larger fraction of low-momentum tracks. The main difference is in the efficiency for UrQMD electrons, which is 79.45 % and 59.20 %, respectively, for the `v24h` and `v24e` setup. This effect arises because the previous rec1TRD cut suppresses UrQMD electrons more strongly in the `v24e` setup, changing the composition before the invariant mass cut. The momentum distributions for UrQMD electrons before and after the invariant mass cut in Fig. 4.22 shows the higher suppression in the low-momentum region in the `v24e` setup. Due to the lower magnetic field, low-momentum electrons are less likely to be bent out of the detector before reaching the TRD.
Additionally, the production position of conversion electrons in the detector can be used for the rejection. First, the χ^2/NDF to the primary vertex is considered. Since conversions occur along the whole detector, their track extrapolation does not necessarily point back to the primary vertex. A comparison of χ^2/NDF for pluto and conversion electrons is shown in Fig. 4.23b. Both distributions peak araound $\chi^{2/\mathrm{NDF}} \approx 0.5$, but the number of pluto electrons decreases for large χ^2/NDF, whereas the number of conversions remains nearly constant above $\chi^2/\mathrm{NDF} \approx 4$. Tracks with $\chi^2/\mathrm{NDF} > 3$ are rejected, as indicated by the black line in the figure. Second, the number of MVD hits is used. Tracks originating behind the second MVD layer are rejected by requiring 2 MVD hits. Electrons produced in the last

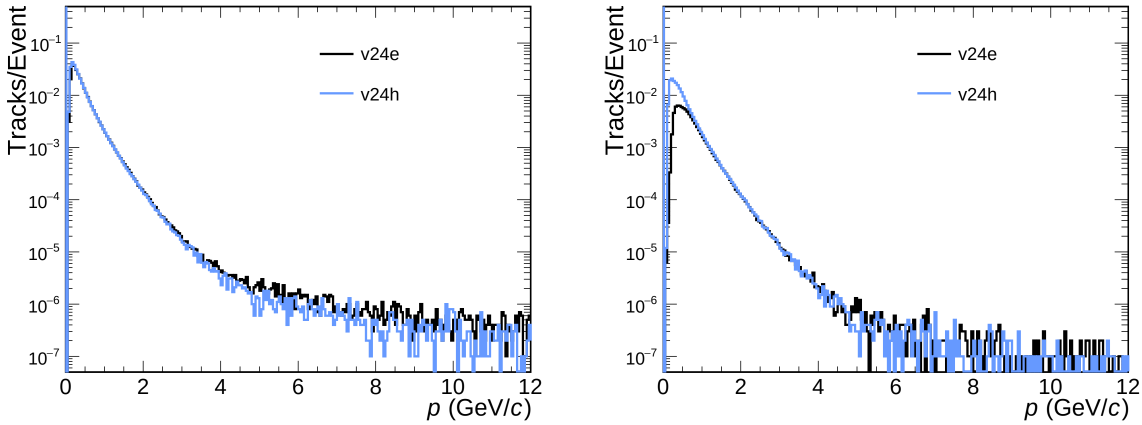

(a) Before rec1TRD **(b)** After rec1TRD

Figure 4.22: Momentum distribution before and after the rec1TRD cut for the `v24e` and `v24h` setup.

MVD layer or behind, as shown in the example in Fig. 4.20, traverse all PID detectors, but leave fewer than two hits in the MVD and can thus be suppressed. The number of MVD Hits is shown for pluto and conversion electrons before the invariant mass cut in Fig. 4.23a. While conversion electrons peak at zero MVD hits, pluto electrons peak at four MVD hits. The chosen cut, indicated in black, suppresses conversions but also affects signal electrons. In the same sequence, an additional cut on STS hits is applied.

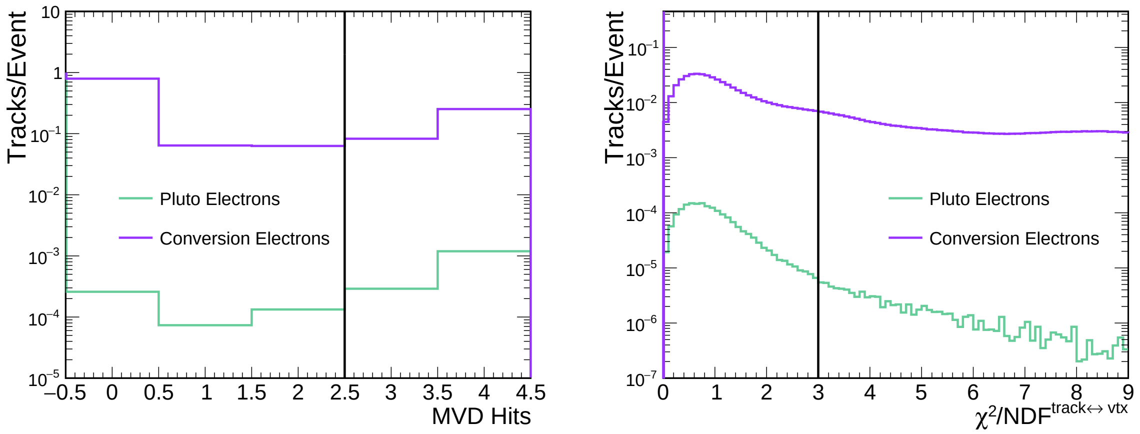

(a) MVD Hits **(b)** χ^2/NDF

Figure 4.23: MVD Hits and χ^2/NDF distribution before the invariant mass cut comparing pluto and conversion electrons. A cut is applied on both since signal electrons originating from the collision point should have lower χ^2/NDF and more MVD Hits than conversion electrons produced along the detector.

The momentum distributions before and after the position-related cuts are shown in Fig. 4.24 for the two different electron sources. The χ^2/NDF cut reduces conversion electrons efficiently

across the whole momentum range, while the MVD cut primarily suppresses conversions for $p < 1\,\mathrm{GeV/c}$. In this momentum range, a visible reduction of pluto electrons is observed as well. Since one hit in the TRD hit is already required before those are not tracks which are leaving the detector acceptence along the MVD. This effect is also visible in [6, Fig.5.25a)] and therefore not related to the beam momentum or the magnetic field. The values in table 4.3 underline the performance of the different cuts. In particular, the χ^2/NDF cut suppresses the conversion electrons by more than factor 2, while reaching an electron efficiency above 90 %. The efficiencies for the `v24h` setup are slightly higher for both sources, which may be related to the fact that more conversion and UrQMD electrons have already been removed in the preceding step. For the MVD cut, efficiencies of $\sim 75\,\%$ for pluto electrons are obtained in both setups while suppression factors larger than 2 are achieved for conversion electrons. As this cut reduces the pluto electrons also significantly, the effect on the low momentum tracks should be further investigated, not only for the used energy, but also for top energy, as the same effect is visible in **??**. Those tracks stem from the primary vertex due to the prior χ^2/NDF and pass the TRD due to the prior recTRD cut and therefore should pass the MVD but have less than 3 hits in the MVD. Overall, the performance of the cuts in the two setups is comparable, yielding similar suppression of conversion electrons and pluto electron efficiency. The main difference appears for UrQMD electrons, where the combined efficiencies are 51.21 % and 39.77 % for `v24e` and `v24h`, respectively. This difference is mainly driven by the invariant mass cut and the preceding rec1TRD cut as explained above.
The remaining conversion electrons are mainly produced close to the target, since they pass the position-related cuts and a large fraction of conversions is left. A detailed discussion of possible reasons is given in section 4.5.

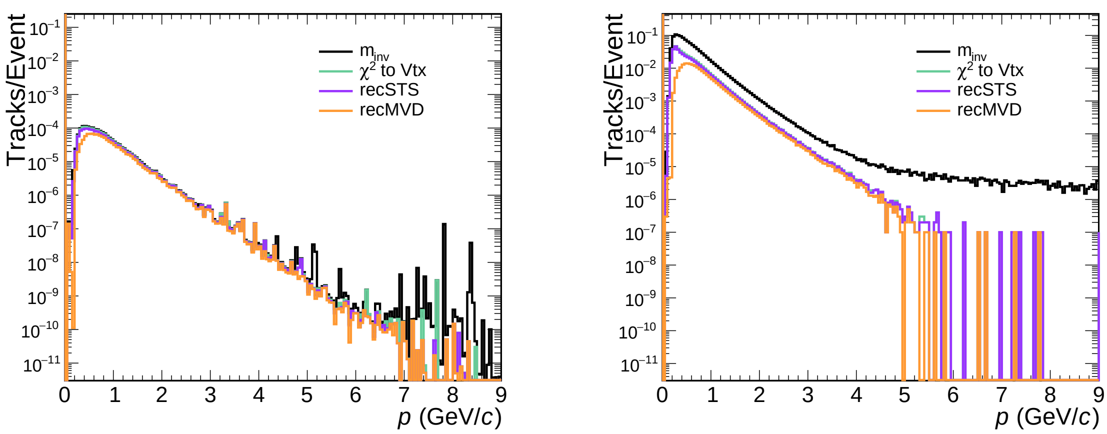

(a) pluto electrons

(b) Conversion electrons

Figure 4.24: Momentum distribution after different position-related cuts of pluto and conversion electrons.

Overall, the performance of the cuts in the two setups is comparable, yielding similar suppression of conversion electrons and pluto electron efficiency. The main difference appears for UrQMD electrons, where the combined efficiencies are 51.21 % and 39.77 % for `v24e` and `v24h`, respectively. This difference is mainly driven by the invariant mass cut and the preceding rec1TRD cut as explained above.
The remaining conversion electrons are mainly produced close to the target, since they pass the position related cuts and a large fraction of conversions is left. A detailed discussion of possible reasons is given in section 4.5.

Table 4.3: Momentum integrated electron efficiency for the different cuts on conversion electrons (values in %).

	v24e			v24h		
Cut step	pluto	UrQMD	conversion	pluto	UrQMD	conversion
m_{inv}	84.52	79.42	87.36	68.95	59.20	71.85
χ^2	93.89	93.61	38.50	94.70	94.46	46.07
recSTS	91.77	91.89	93.17	93.96	93.61	96.23
recMVD	74.22	74.93	47.40	75.85	75.97	42.84
Combined	54.06	51.21	14.91	46.53	39.77	13.64

4.2.2 Incomplete Pairs

Tracks can be classified according to the detectors they traverse, resulting in four distinct categories illustrated in Fig. 4.25a. Their definitions and implementation criteria are as follows:

Out-of-acceptance (OOA) tracks do not reach detectors. No MC hits in STS+MVD.

Track fragments reach the tracking detectors but are not reconstructed.
$1 \leq$ hits in MVD+STS ≤ 3.

Track segments are reconstructed but do not reach all PID detectors.
MVD+STS hits ≥ 4, no hits in RICH/TRD/TOF.

Global tracks traverse all detectors. MVD+STS hits ≥ 4, hits in RICH/TRD/TOF.

After the PID Cuts, only global tracks remain, since hits in all PID detectors are required. If the partner track of a global track is a fragment, segment, or out of acceptance, that partner is rejected by the cuts. The remaining global track then contributes solely to the combinatorial background, because its true partner is lost. To suppress this background source, global tracks with rejected partners must be identified.
Track classification uses MC information to determine the partner track types. In Fig. 4.25b,

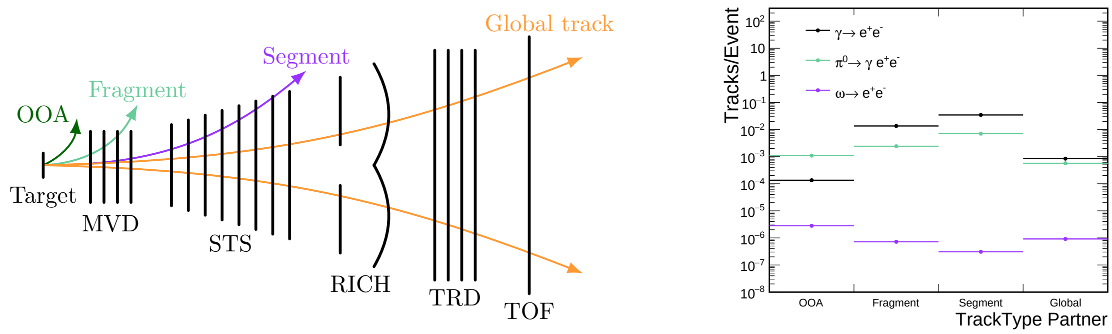

(a) **(b)**

Figure 4.25: Sketch of tracks classified as global, fragment, segment, or out of acceptence based on detector coverage (a) and their occurence as partners of remaining tracks for three decay channels (b). Fragments, segments, and OOA tracks are rejected by PID cuts. Global tracks whose partners fall into these categories contribute only to combinatorial background. Low-mass decays (γ, π^0) show significantly more segment partners and thus should be reduced.

the distribution of partner track types is shown for three different decay channels: photon conversions $\gamma \rightarrow e^+e^-$, π^0 Dalitz decays $\pi^0 \rightarrow \gamma e^+e^-$, and ω decays $\omega \rightarrow e^+e^-$. The high fraction of conversions and π^0 Dalitz tracks compared to ω decays demonstrates the importance of suppressing low-mass decays.

Since OOA tracks and track fragments are not reconstructed, information about them is only available using MC methods, which can only be accessed in simulations but not in the case of real data. Track segments, however, are reconstructed, so the first goal is to reduce the amount of global tracks with track segments as partners, which are most prevalent in low invariant mass decays. For $m_1 = m_2 = 0$, the invariant mass can be written as

$$M_{\text{inv}} = \sqrt{2p_1p_2(1 - \beta_1\beta_2\cos\Phi)} \approx 2\sin\left(\frac{\Phi}{2}\right)\sqrt{p_1p_2}. \tag{4.7}$$

Hence, for small M_{inv} the opening angle Φ is small. In the analysis, for each global track the opening angle is obtained by taking the smallest opening angle to segments from the same event. As shown in Fig. 4.26a, the opening angle to every possible partner segment is calculated and the segment with the smallest opening angle Φ_{min} is matched. For small opening angles, as in Fig. 4.26b, it is likely that this smallest opening angle corresponds to the true opening angle. For larger opening angles, as in Fig. 4.26c, it is likely that there are segments with smaller opening angles and it is a fake match.

In Fig. 4.27 the matches for the different decays are listed by accessing MC information and comparing the matched track to the true partner. No match means, that there is no reconstructed track to match, which can also count as a fake match. The distribution shows,

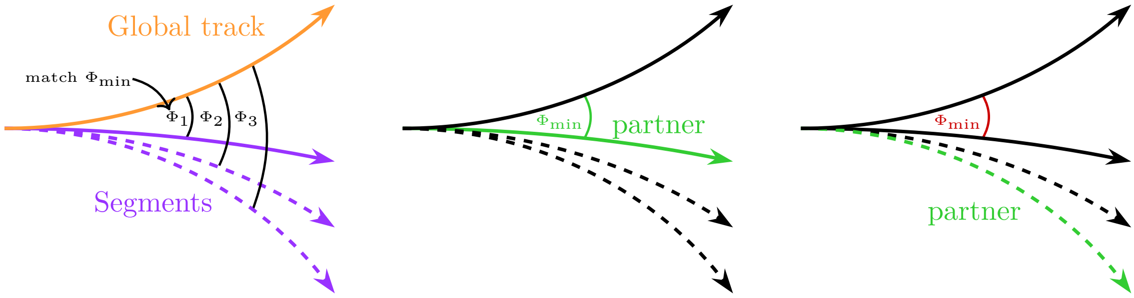

(a) **(b)** **(c)**

Figure 4.26: Schematic drawing of the calculation of the opening angle $\Phi_{\min}$. As opening angle for a track the lowest opening angle is chosen which is Φ_1 in (a). For small opening angles it is likely that the smallest opening angle is the true opening angle (b). For large opening angles usually there is a closer track and the opening angle is wrong (c).

that true matches contribute significantly for π^0 Dalitz and conversions, while there are no true matches for ω decays which confirms the dependence of the matched opening angle on the invariant mass.

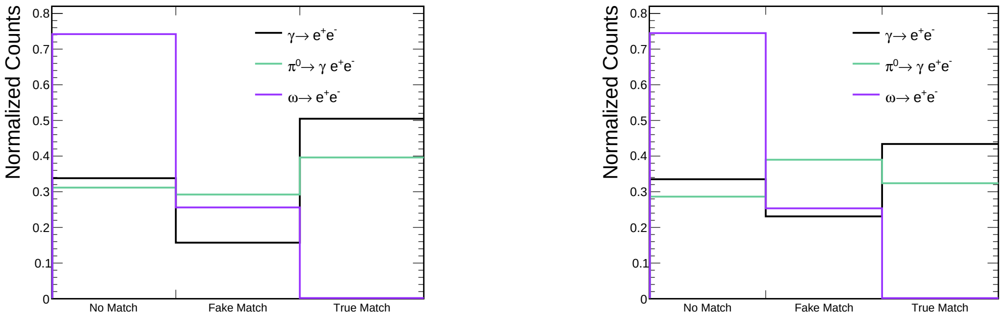

(a) v24e **(b)** v24h

Figure 4.27: Information about the matched track by taking the smallest opening angle $\Phi_{\min}$ for three different decays. Using MC information it is evaluated if the reconstructed track is a true or fake match where no match means that there is no true reconstructed partner which can also count as a fake match. While there are no true matches for ω-decays, there are true matches for conversions and π^0-Dalitz decays. In the **v24h** setup are less true matches.

To reduce the number of low invariant mass pairs, those true matches must be identified. For true matches, a correlation between $\Phi = \Phi_{\min}$ and $\sqrt{p_1 p_2} = \sqrt{p_{\text{global}} p_{\min}}$ is expected according to eq. (4.7). In Fig. 4.28, these two variables are shown. For γ and π^0 a correlated bulk is visible for small $\Phi_{\min}$, while for ω decays only the underlying random background from mismatched partners is visible. A cut is applied to reject this correlated bulk, as indicated by the black line in Fig. 4.28. The resulting distribution of partner types after this cut is shown in Fig. 4.29, where the fraction of segments is significantly reduced for γ and π^0 decays while global tracks are maintained for both setups.

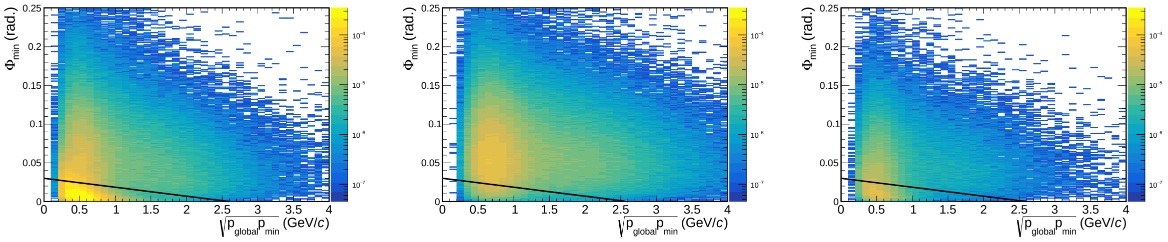

(a) $\gamma \to e^+e^-$ (b) $\omega \to e^+e^-$ (c) $\pi^0 \to \gamma e^+e^-$

Figure 4.28: Opening angle for $\sqrt{p_{d1}p_{min}}$ for different decays. Low invariant mass decays have true matches which are visible in a bulk at small angles, which is removed by a cut indicated by the black line.

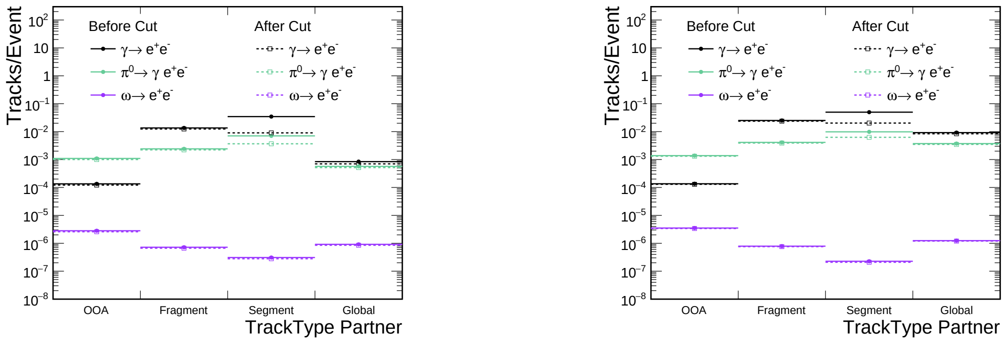

(a) `v24e` (b) `v24h`

Figure 4.29: Partner track types of remaining tracks before and after the opening-angle cut for three different decay channels. For low invariant mass decays, the fraction of partners classified as fragments is significantly reduced.

The reduction is higher in the `v24e` setup as the comparison of Fig. 4.29a and Fig. 4.29b shows. Already a comparison of the true hits in Fig. 4.27 shows that there are more fake matches and less true matches for the `v24h` setup. To compare the two setups the matched opening angle Φ_{min} is shown in Fig. 4.30a, b, and c for the three decays for both setups. For each decay, the matched opening angle in the `v24h` setup has a broader distribution to higher matched opening angles Φ_{min}. In addition, the opening angle to the true partner Φ_{true} is compared in Fig. 4.30d, e, and f for each decay. For the ω-decay, the distributions are comparable but for γ and π^0 the same shift to higher opening angles is visible. Thus small reconstructed angles are larger at lower magnetic field.

The opening angle is reconstructed by calculating the angle between the momentum vectors of the tracks. In Fig. 4.31 the matched opening angle Φ_{min} is compared to the opening angle of the corresponding MC momentum vectors $\Phi^{\mathrm{MC}}_{\mathrm{min}}$. The main diagonal meets $\Phi_{\mathrm{min}} = \Phi^{\mathrm{MC}}_{\mathrm{min}}$ and thus corresponds to correctly reconstructed opening angles. The main distribution is along this main diagonal. However, for conversions and π^0 Dalitz, there is a bulk below the main diagonal at low opening angles, corresponding to larger reconstructed opening. Hence at low opening angles, the reconstructed opening angle is larger than the true opening angles, which is a result of the momentum reconstruction. As the momentum resolution is better at higher magnetic field, the effect is stronger in the `v24h` setup resulting in the shifted peaks in Fig. 4.30. Since the matched opening angle Φ_{min} is the smallest possible opening angle, it is particularly affected unlike the larger opening angle to the true partner for ω in Fig. 4.30f.

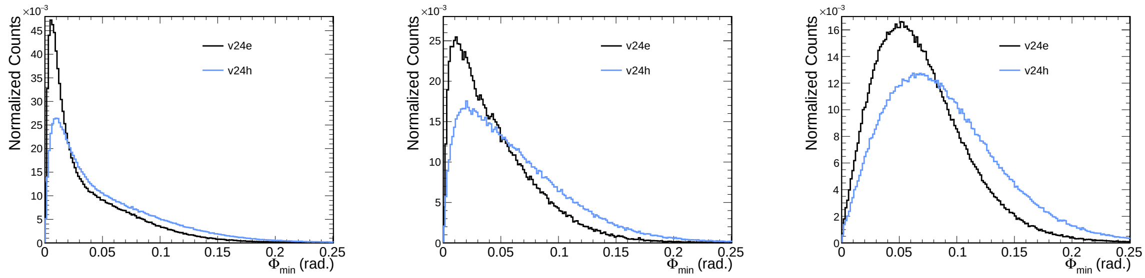

(a) $\gamma \to e^+e^-$ **(b)** $\pi^0 \to \gamma e^+e^-$ **(c)** $\omega \to e^+e^-$

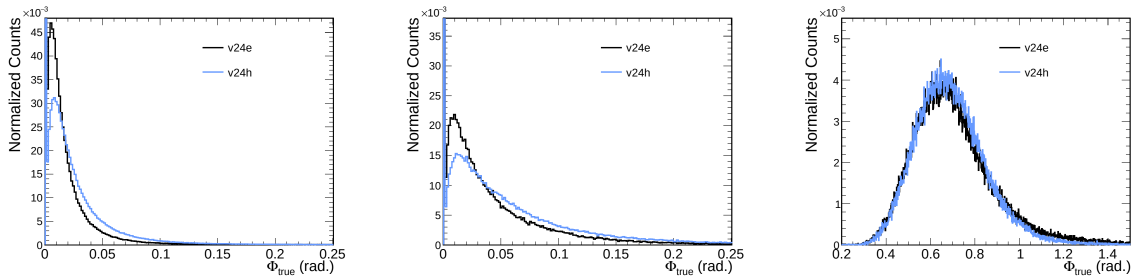

(d) $\gamma \to e^+e^-$ **(e)** $\pi^0 \to \gamma e^+e^-$ **(f)** $\omega \to e^+e^-$

Figure 4.30: Normalized distributions of the Opening angle to the matched partner partner Φ_{min} (top row) and the true partner Φ_{true} (bottom row) for three different decays in comparison for the two different setups. The matched opening angle Φ_{min} is larger at lower magnetic field in the `v24h` setup.

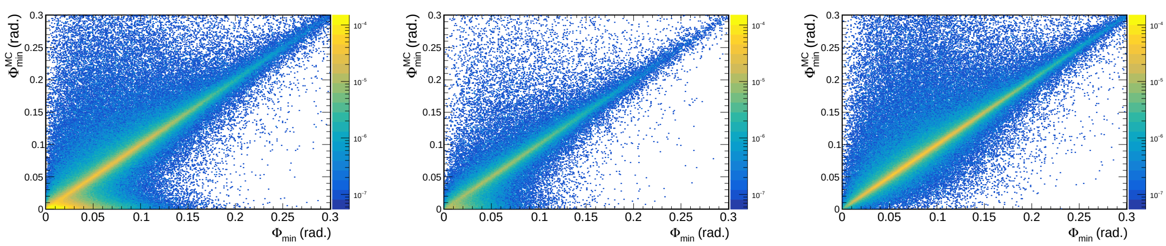

(a) $\gamma \to e^+e^-$ **(b)** $\pi^0 \to \gamma e^+e^-$ **(c)** $\omega \to e^+e^-$

Figure 4.31: Opening angle Φ_{min} compared to the MC value Φ_{min}^{MC} for different decays for the `v24h` setup. At small opening angles the reconstructed opening angle is larger for the low invariant mass decays of γ and π^0.

4.3 Combined Results

To evaluate the performance of the different cuts, the distribution of particle species after each group of cuts is shown in Fig. 4.32. The `v24e` setup is compared to the `v24h` setup (dashed lines). Overall, each group of cuts reduces the intended particle species. The preCuts, including the conversion rejection, mainly reduce UrQMD and conversion electrons, whereas the PID cuts suppress pions, protons, and kaons. The opening-angle cut reduces UrQMD and conversion electrons while maintaining high pluto electron efficiency. In total, the cuts significantly reduce the background with only moderate signal electron loss in both setups.

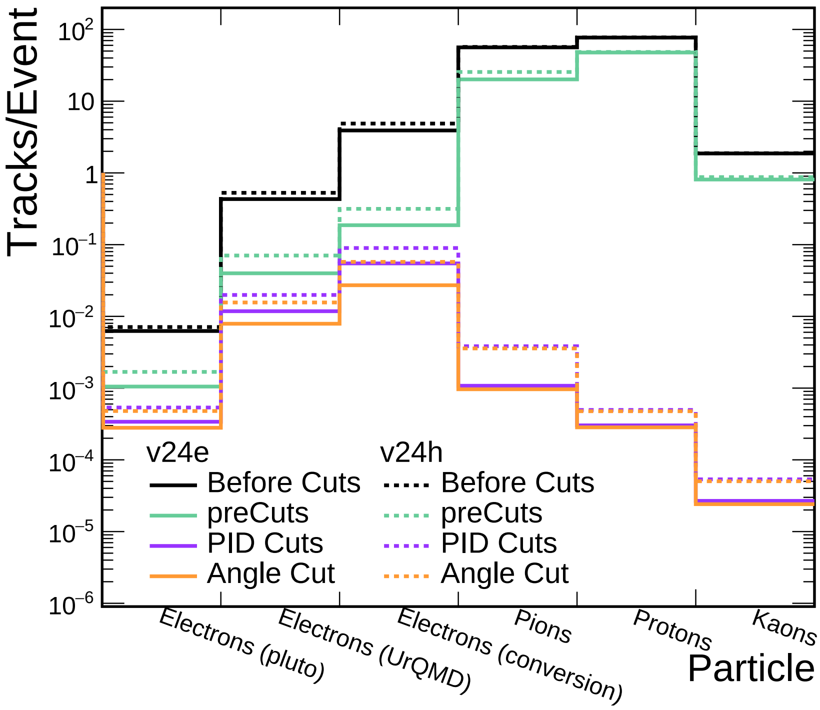

Figure 4.32: Particle species before and after each group of cuts compared for the two setups `v24e` and `v24h`. Each cut suppresses the background it is designed for.

Since the logarithmic scale in Fig. 4.32 makes a direct comparison between the two setups difficult, the ratio `v24h`/`v24e` is shown as a function of the particle species for each group of cuts in Fig. 4.33. Already before any cuts, slightly more tracks of each particle species are present in the `v24h` setup. As discussed before, this is due to the lower magnetic field, which bends low-momentum particles less strongly and therefore keeps more of them within the detector acceptence. This effect is most pronounced for the three different elctron sources.

The change in ratio allows one to compare the effect of each cut group in the two different setups. If the ratio increases after a given cut group, relatively more tracks survive in the `v24h` setup, meaning that the suppression is lower there. The first group, the preCuts, includes besides general cuts the conversion rejection described in section 4.2.1. The ratio increases for all species, indicating stronger overall suppression in the `v24e` setup. In particular, this is visible for UrQMD and conversion electrons, which are dominantly reduced by these cuts. In section 4.2.1 it was noted that the conversion cuts themselves perform better in the `v24h` setup by reaching slightly higher suppression for conversion electrons and significantly higher suppression for UrQMD electrons. At the same time, the requirement of at least one TRD hit affects `v24e` and `v24h` differently because of the different magnetic fields which leads to a different baseline for the cuts. When all preCuts are combined, the suppression is still stronger in `v24e`, while the higher ratio for pluto electrons shows that more signal survives in `v24h` at this stage.

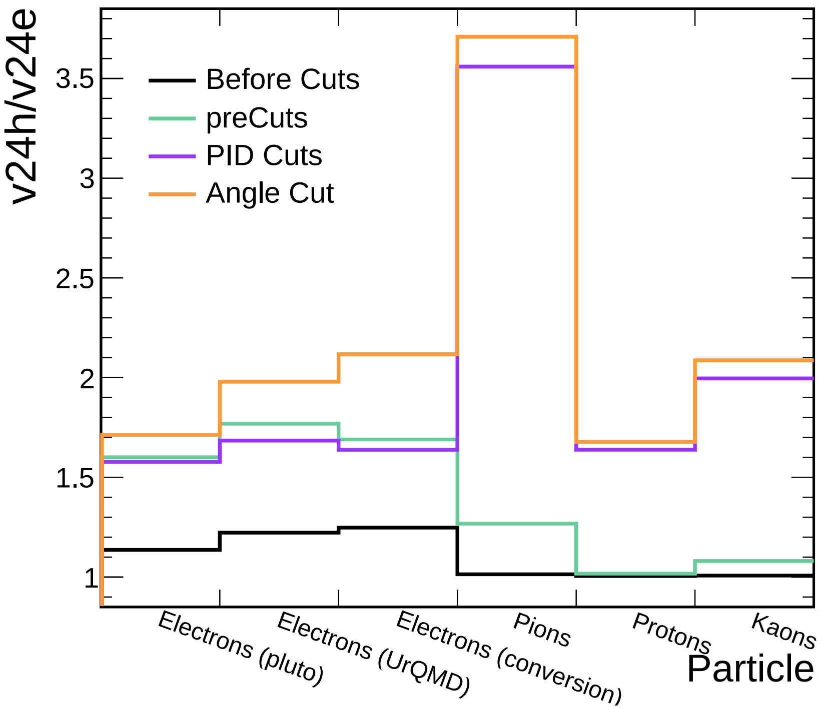

Figure 4.33: Ratio of particle yields `v24h`/`v24e` after each group of cuts. Values greater than one indicate weaker suppression in the `v24h` setup.

Next, the PID cuts, which target the hadronic background reduction, are applied. Here the ratio again increases for most particle species, in particular for pions. This trend is consistent with section 4.1, where the combined pion suppression factors of 6649 and 18664 were found for `v24h` and `v24e`, respectively. This explains the increase of ~ 3 in the ratio, but also for protons and kaons the `v24e` performs better. The weaker suppression in `v24h` is due to the reduced performance of RICH and TRD at low momenta, and this region is more populated because of the lower magnetic field.

Finally, the opening angle cut also increases the ratio for all particle species, implying stronger suppression in the `v24e` setup for this step as well, which is caused by the reconstruction of the opening angle. All in all, the full cut chain performs better for the `v24e` setup: for comparable signal-electron efficiency, the hadron and conversion suppression are systematically stronger than in `v24h`. Only the preCuts have a better performance for signal electrons. Although RICH and TRD PID cuts are specifically tuned for the `v24h` setup, it is not possible to achieve comparable suppression at similar electron efficiency, due to the differences caused by the reduced magnetic field.

4.4 Invariant Mass Spectrum

The resulting invariant mass spectra for the two beampipe configurations are shown in Fig. 4.34. The remaining tracks after applying all cuts described in section 4.1 and section 4.2 are used to form all possible unlike-sign pairs from the same event (SE^{+-}), shown in black. In addition, MC information is used to determine the origin of the electrons, and the different contributions are displayed separately. π^0 Dalitz decays dominate the region $M_{\mathrm{inv}} < 0.1\,\mathrm{GeV/c^2}$. In the low-mass region up to $M_{\mathrm{inv}} < 0.6\,\mathrm{GeV/c^2}$, η Dalitz decays provide the main contribution. In this region, ω Dalitz decays and the in-medium spectral function also contribute. At higher masses, the peaks from $\omega \to e^+e^-$ and $\phi \to e^+e^-$ dominate, whereas above, only the spectral function contributes.
Comparing the spectra for the two setups shows that the ω and ϕ peaks are broader for the `v24h` configuration, with contributions extending up to about $1.8\,\mathrm{GeV/c^2}$, compared to $\sim 1.2\,\mathrm{GeV/c^2}$ in `v24e`. This is caused by the worse momentum resolution at lower magnetic field. All contributions are slightly larger in the `v24h` setup, which is particularly visible for the π^0 Dalitz component. This is due to the slightly higher electron efficiency for signal electrons and the weaker suppression of UrQMD electrons in the `v24h` setup. In addition, the combinatorial background is higher in the `v24h` setup and lies relatively further above the sum of the individual sources, which is due to the lower background suppression for hadrons and conversion electrons.
For both setups, many bins in the IMR above $M_{\mathrm{inv}} = 1.5\,\mathrm{GeV/c^2}$ follow the spectral-function curve exactly, and above $M_{\mathrm{inv}} \gtrsim 0.6\,\mathrm{GeV/c^2}$ individual bins fluctuate strongly, both in value and in statistical error. This is caused by the embedding in combination with limited tracks remaining in this mass range. Bins that contain only embedded pluto sources have small statistical errors due to weighting and fit the MC curve, since there is no background contribution. In contrast, bins with both signal and background fluctuate more strongly. To better reflect the underlying distribution including background, the spectra are therefore rebinned. In Fig. 4.35 the rebinned spectra are shown. Above $M_{\mathrm{inv}} = 1.24\,\mathrm{GeV/c^2}$, a bin width of

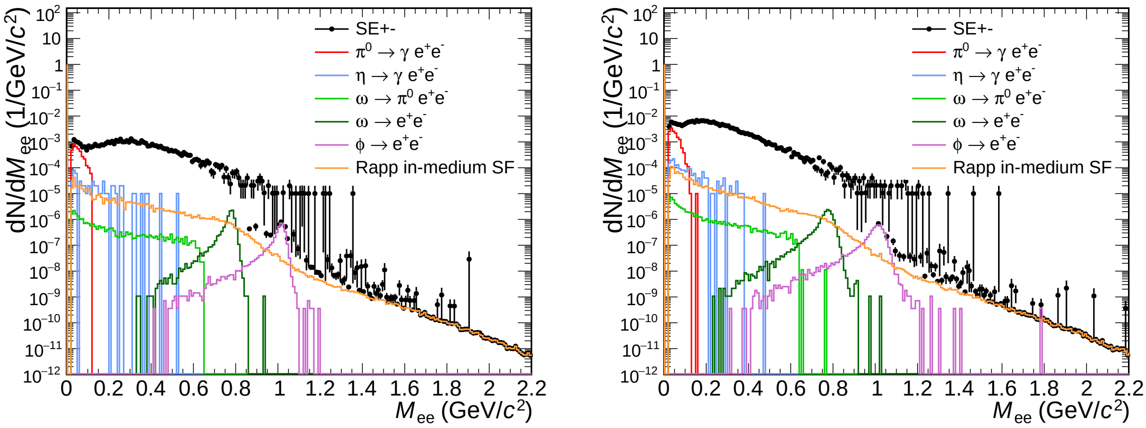

(a) v24e **(b)** v24h

Figure 4.34: Invariant mass spectrum after the full analysis for the two beampipe configurations. All unlike-sign pairs from the same event (SE^{+-}) of the remaining tracks are shown in black. MC information is used to decompose the spectrum into various pluto and UrQMD sources.

0.32 GeV/c^2 is used, while below this value a finer binning of 0.04 GeV/c^2 is applied. With this rebinning, the background level becomes more apparent, in particular in the v24h setup, and the regions around the ω and ϕ peaks are represented more realistically.

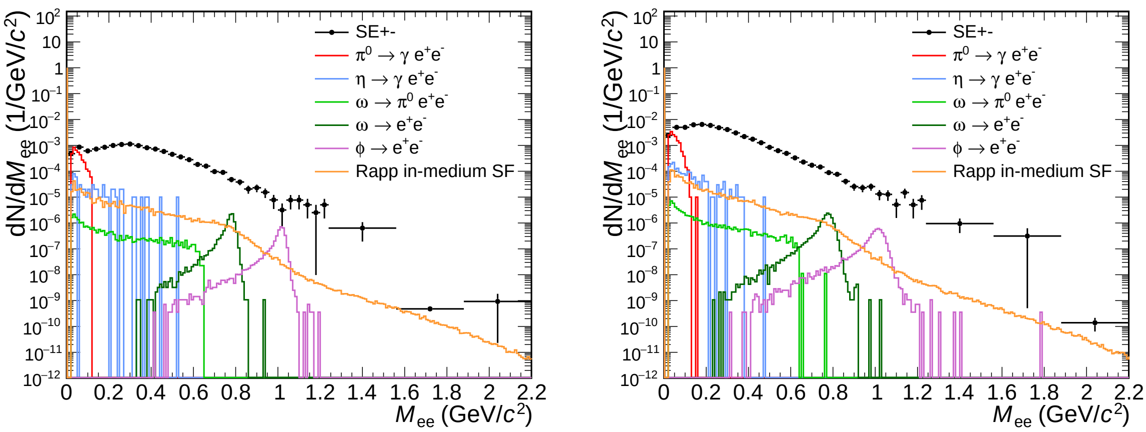

(a) v24e **(b)** v24h

Figure 4.35: Rebinned invariant mass spectra corresponding to Fig. 4.34. A bin width of 0.04 GeV/c^2 is chosen up to $M_{\text{inv}} = 1.24$ GeV/c^2 and 0.32 GeV/c^2 above, due to limited statistics in this region.

4.5 Reduction of Conversion Electrons

As noted at the end of section 4.2.1, even after conversion rejection a significant number of conversion electrons remains. These are most likely electrons produced close to the collision vertex, since they satisfy $\chi^2/\mathrm{NDF} < 3$ and have more than 2 MVD hits. Comparing Fig. 4.32 to [6, Fig.5.22] and other prior simulations shows that the number of remaining conversion electrons is comparatively high. After PID cuts, there are still more conversion electrons than UrQMD electrons, whereas [6] shows fewer conversions than UrQMD electrons.
This difference is due to the used target. While previous simulations used a 25 μm target, the simulation here uses a 250 μm target, which increases the number of conversions. CBM is foreseen to use a $10 \times 25\,\mu$m segmented target, which should significantly reduce conversions. In Fig. 4.36, schematic drawings of the two target types are shown. The segmented target on the left and the block target on the right. For the segmented target, conversions occur in different layers, while in the block target they occur throughout the whole target. This increases the distance from the collision vertex to the conversion point and, if the interaction layer is known, allows early reduction of conversions during analysis. The segmented target is expected to substantially reduce the conversion background compared to the target used here.

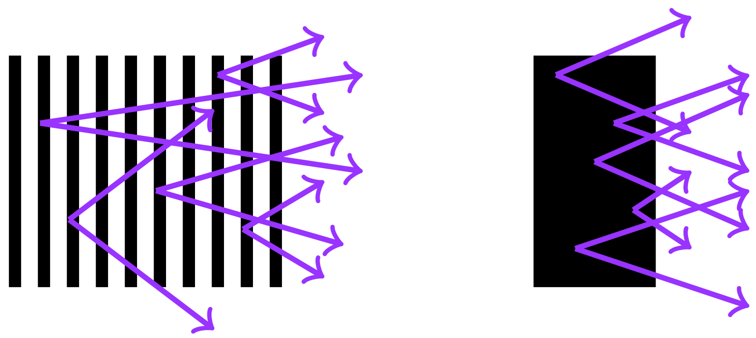

Figure 4.36: Schematic drawing of the conversions in a segmented target (left) and a block target (right).

To account for this reduction, the number of conversions was artificially reduced after completing the full analysis chain. Randomly selected conversion electrons were rejected. While removing the additional conversions only after the cuts makes the efficiencies of the cuts, in particular the conversion cuts, less meaningful, applying the reduction earlier is not possible. A reduction before the invariant mass cut would leave incomplete pairs which makes the invariant mass cut ineffective since it is a pair cut. Moreover, the artificial reduction should be applied to the conversions which are produced because of the different target. Those are exactly the conversion electrons produced close to the collision point which are passing all detectors and thus the ones passing the χ^2/NDF and MVD cuts. Therefore, the random rejection of conversion electrons is applied after the full chain of cuts.

Here, the mass spectra are shown for two different reduction levels: 50 % in Fig. 4.37 and 80 % in Fig. 4.38. For both setups and both reduction levels the unlike-sign pairs are significantly reduced. For the `v24e` setup and 80 % reduction, the distribution approaches the MC distribution in the IMR, while for the other spectra a fluctuation is visible even though the binwidth is large. This shows the low statistics in the intermediate-mass region of the mass spectra, particularly for the `v24e` setup.

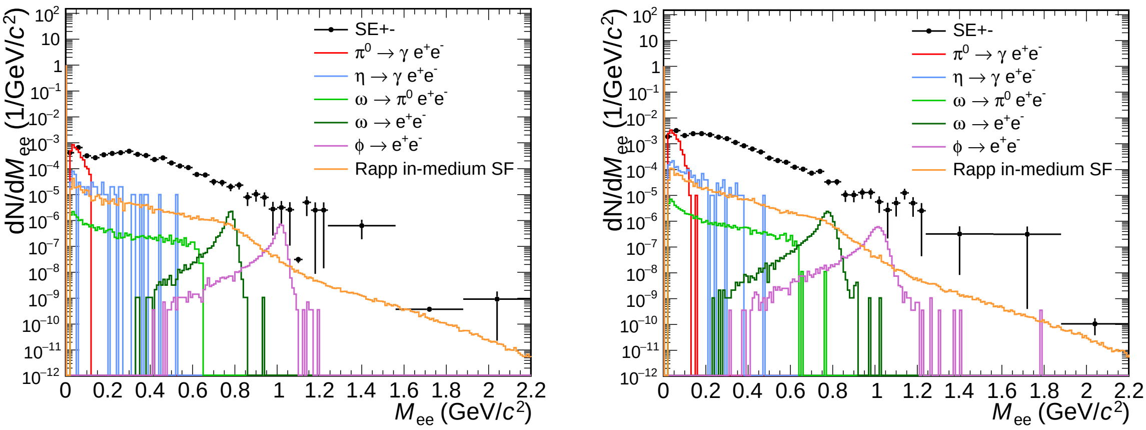

(a) `v24e` **(b)** `v24h`

Figure 4.37: Invariant mass spectra as in Fig. 4.35 but after the analysis chain the number of conversion electrons was reduced by 50%.

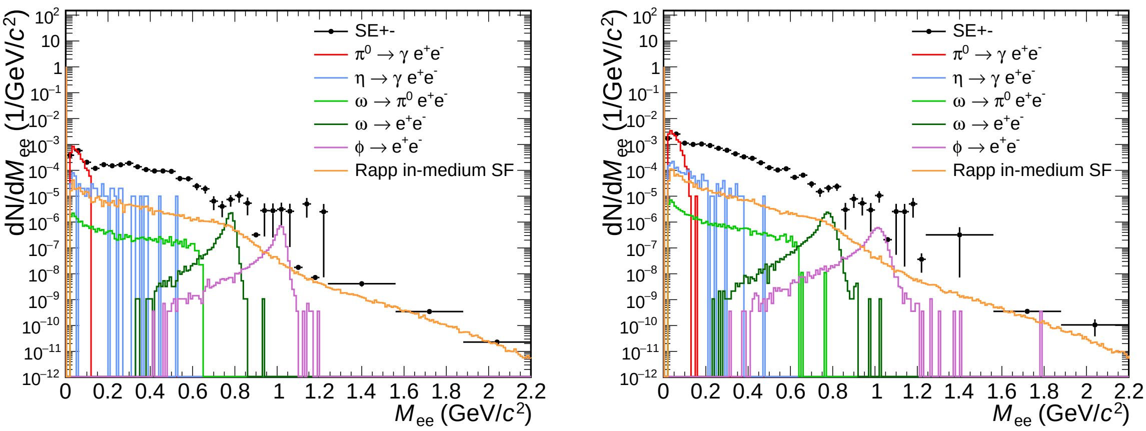

(a) `v24e` **(b)** `v24h`

Figure 4.38: Invariant mass spectra as in Fig. 4.35 but after the analysis chain the number of conversion electrons was reduced by 80%.

4.6 Additional Background Simulation

To increase statistics for the combinatorical background, especially in the IMR, a fast simulation approach is used, which was developed by Cornelius Feier-Riesen for CBM [40] and adaptet to PAPA in [6]. The full simulation chain, as described in chapter 3, requires a lot of resources, such as processing time and disk space. However, the fast simulation approach randomly samples multiplicities and three-momentum distribution of different particles to efficiently generate new events.

The full process for the background simulation is shown in Fig. 4.39. At first, the full simulation chain, comprising UrQMD, and pluto event generation, and GEANT transport, described in chapter 3 is completed. Subsequently, the provided reconstructed tracks and MC information is used to perform the analysis descriped in chapter 4 comprising the different cuts. The output of the analysis provides histograms and in particular multiplicity and three-momentum distributions for the different particles. This output is used as input file for the event generation. By randomply sampling the distributions random background events are generated.

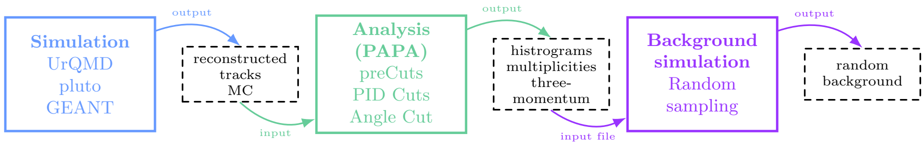

Figure 4.39: Schematic drawing of the simulation and analysis chain.

To verify the applied fast simulation approach, in the following the obtained background by using the random event technique is compared to the background in the used input file. A cut configuration until the RICH ANN cut is used to increase statistics and only UrQMD events are used for the comparison.

In Fig. 4.40 a comparison of the obtained multiplicity distribution by random event generation to the one of the input file for UrQMD tracks is shown. The random sampling reproduces the distribution of the input file. However, comparing the background of the input file to the obtained background in Fig. 4.41a shows a difference for both setups. As the ratio shows, the background in the input file is higher across the whole M_{inv} range, but especially at low M_{inv}. Since the random sampling should reproduce the distribution, the ratio should be 1. One reason for differences in the background are correlated pairs. While the correlations occur in the input file, the random event generator does not account for that.

Previously simulated data showed the same shift at low M_{inv}, but not across the full mass range. Therefore a comparison to this simulation campaign and a discussion of possible reasons is provided in appendix A.6. However, the shift is divided into two contributions: a

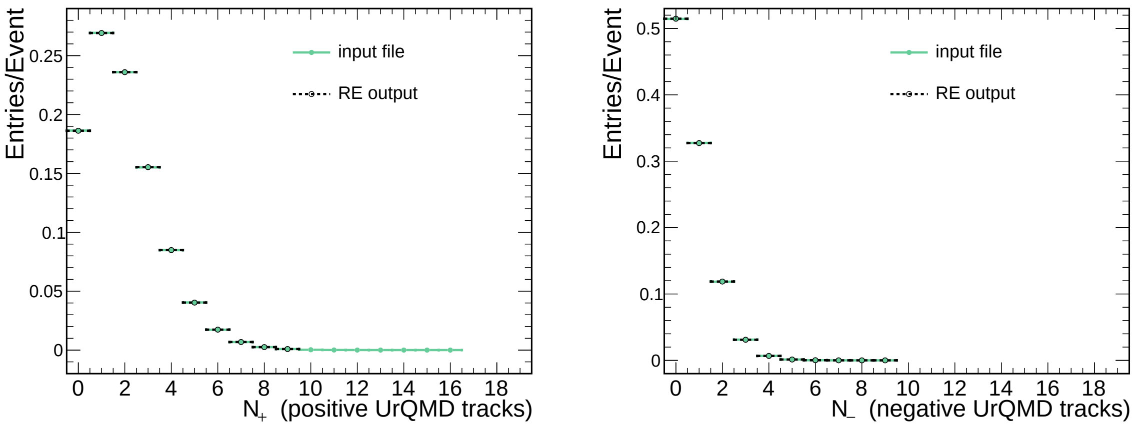

(a) (b)

Figure 4.40: Resulting multiplicities compared to the multiplicity of the input file for positive and negative UrQMD tracks.

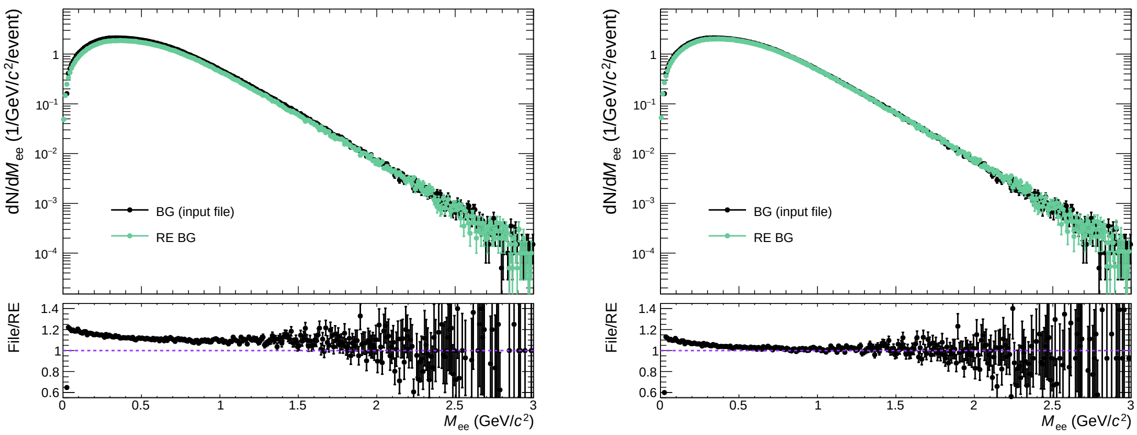

(a) (b)

Figure 4.41: Invariant mass distribution of the background simulated by the fast simulation approach compared to the background in the input file for the `v24e` setup. The unexpected shift in a) is accounted for by applying the obtained background by 1.08 (b).

constant shift across the whole mass range and a mass dependent shift at low masses. By multipliyng the random event backgorund by a factor of 1.08, the ratio approaches 1 for $M_{\mathrm{inv}} > 0.4\,\mathrm{GeV/c}^2$ as shown in Fig. 4.41b. Thus in the following, the obtained background is multiplied by 1.08 to account for the observed difference but investigations are ongoing to identify the reason of the difference and adapt the background simulation accordingly. At low M_{inv} the background in the input file is still higher. As statistics in this regime are reasonable high, the obtained background is only used for $M_{\mathrm{inv}} > 0.4\,\mathrm{GeV/c}^2$.
Using the descibed method, 6×10^9 events are simulated and the obtained background is compared to the signal. Therefore MC information is used to identify the signal as shown in

the mass spectrum in Fig. 4.34 and this signal is divided by the obtained background approximation. The results for both setups and the same reduction of conversion background as in section 4.5 is shown in Fig. 4.42. At low M_{inv}, the signal consists of Dalitz decays and the signal to background ratio is higher in the `v24e` setup as expected due to the higher combinatorical background in Fig. 4.34 for the `v24e` setup. By reducing the number of conversions, the signal to background ratio is significanty improved in this region for both setups.
As the ω and ϕ peaks are broader in the `v24h` setup, the signal to background ratio is higher around these peaks in the `v24h` setup but not at the highest point. The ϕ peak expands up to about $M_{\text{inv}} = 1.5\,\text{GeV}/\text{c}^2$ in the `v24h` setup. While the peaks reach a signal to background ratio of 0.05 for the full number of tracks, this is improved to 0.5 by reducing the number of conversion electrons by 80 %. This is comparable with the achieved ratio in [6]. Above, the ratio is again higher for the `v24e` setup but the statistics are limited for $M_{\text{inv}} > 1.5\,\text{GeV}/\text{c}^2$. However, Fig. 4.42a indicates that a signal to background ratio of 0.001 can be reached which can be increased up to 0.005 with a reduction of the conversions by 80 %. Again this is comparable with the values reached in [6]. To evaluate the difference of the two setups in the IMR even more background events are required.

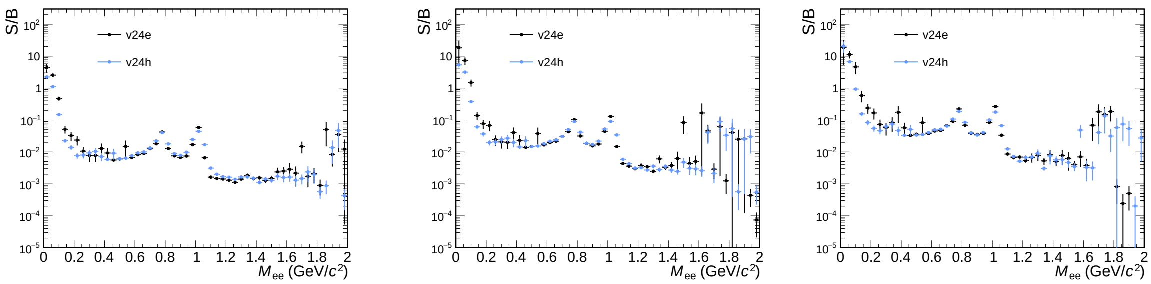

(a) 100 % conversions **(b)** 80 % conversions **(c)** 80 % conversions

Figure 4.42: Signal to background ratio for the full sample of remaining tracks and the number of conversion electrons reduced by 50 % and 80 %, respectively. 10^9 events are used for the background estimation for $M_{\text{inv}} > 0.4\,\text{GeV}/\text{c}^2$.

5 Conclusion and Outlook

CBM is designed to investigate the QCD phase transition at high μ_B. Accordingly, the collision energy range of CBM is scanned to probe properties of the fireball created in the heavy-ion collision. Dileptons are therefore an important probe, as, for example, the temperature can be extracted from the invariant-mass spectrum. To accurately measure the dilepton invariant mass spectrum the goal of the analysis is to suppress background such as hadrons, conversion electrons, but also single electrons without a partner. While prior work as in [6] and [39] was focused on top energy of CBM, in this thesis a lower energy of $\sqrt{s_{\mathrm{NN}}} = 3.19\,\mathrm{GeV}$, corresponding to gold beams of $P_{\mathrm{beam}} = 4.41\,\mathrm{AGeV}$, is assessed. Since hardware for lower collision energies was being developed in parallel with this thesis this is especially important. In particular, a lower beam energy requires a different beampipe to avoid the beam from colliding with the beampipe. Such beampipes were designed recently. Since there is no dedicated beampipe for the used beam momentum, this work compares two scenarios using the beampipes `v24e` and `v24h`. For both, the magnetic field has to be scaled down to acommodate the beam to 74% and 37% of its nominal value, respectively.
For the analysis the PAPA framework is used which was recently refined in [6]. The cut sequence is used and single cuts are slightly adjusted and their performance is evaluated. Hadrons are reduced by the PID cuts using RICH, TRD, STS, and TOF information. Compared to [6] the achieved hadron suppression is higher while reaching a comparable electron efficiency. This improvement results from tuning the RICH and TRD cuts to higher efficiencies, combined with the fact that tracks do not reach high momenta, which makes the low-momentum sensitive TOF and STS cuts more effective. Nevertheless, as a next step the machine learning approach which was applied in [6] might be used to further improve the hadron suppression.
Comparing the two setups, there are more low momentum tracks in the `v24h` setup, since the bending due to the magnetic field is less pronounced. Each PID cut reaches higher suppression factors in the `v24e` setup, which is particularly relevant for pions. While the RICH ring cut is mainly affected by ring-to-track matching at low momentum, the RICH ANN cut performs worse due to the ring-to-track distance at low momentum. Both are an effect of the worse momentum resolution at lower magnetic field. The Likelihood cut performs worse at

low momentum due to less TR production which is important due to the dominance of low momentum tracks.
The reduced momentum resolution in the lower magnetic field directly affects the opening angle cut, since small opening angles are reconstructed larger as their MC value. Since sxpecially these small values are important for the matching, there are less true matches which results in a lower suppression. Also position related improvements in [6] are not significant here since the distance between the tracks is affected by the magnetic field as well.
The conversion electrons are dominated by those from the target, which makes it hard to evaluate the cut. But a change from a monolithic to a segmented target is expected to significantly reduce the number of conversion electrons and therefore improves the signal to background ratio.
As the number of signal tracks, but also background tracks is lower at low momentum the additional background simulation is especially important, for which the fast simulation technique developed in [40] was used. The background simulated with this approach. The simulated background is lower as the background used as input, which is accounted for by applying a correction factor. Since this correction is just evaluated by comparison of input and output and there is no technical or physical reason found yet, this should be further investigated.
All in all, background rejection decreases with decreasing magnetic field strength, which is mainly affected by the higher number of low momentum tracks and the decreased momentum resolution. While the PID cuts still perform for protons and kaons and especially the RICH cut could be improved by training the ANN to lower energies and magnetic field, the electron rejection methods have less room for improvement. In particular, the opening angle cut is affected by the momentum resolution. Therefore the highest possible magnetic field configuration should be used to obtain the best results.

A Appendix

A.1 Momentum Resolution in CBM

The momentum resolution in the STS is shown for two different settings in Fig. A.1. While a 1 T magnetic field and a 12 AGeV beam were used in Fig. A.1a a 0.5 T magnetic field and a 2 AGeV beam were used in Fig. A.1b. In both figures two different setups are compared. For the lower magnetic field, the momentum resolution deteriorates, with $\Delta p/p$ being higher across the full momentum range, particularly at low momenta.

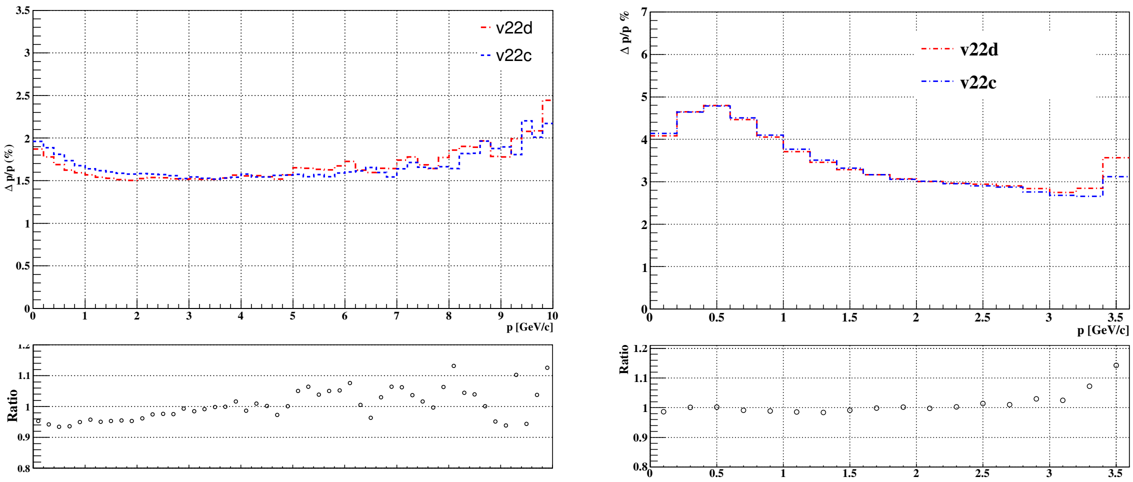

(a) 1 T; 12 AGeV

(b) 0.5 T; 2 AGeV

Figure A.1: Momentum resolution in the STS in two different field settings [41].

A.2 TRD 2D

As explained in section 2.1.4 in the center of the TRD the TRD-2D is placed. To take advantage of the TRD-2D the v20d geometry was included for a test run.

The energy loss for electrons in the TRD before applying the TRD cuts is shown in Fig. A.2a. Below 1 keV, an unexpected peak is visible. Figure A.2b shows this energy loss in comparison to the MC value for the energy loss. If the reconstructed energy loss were equal to the MC value, all the values would lie on the main diagonal. In addition to the main diagonal, another diagonal and a cluster are visible. The cluster is below the main diagonal, meaning the reconstructed energy loss is higher than the MC value. Since the plot is for electrons, such a cluster is expected for electrons with additional TR photons.

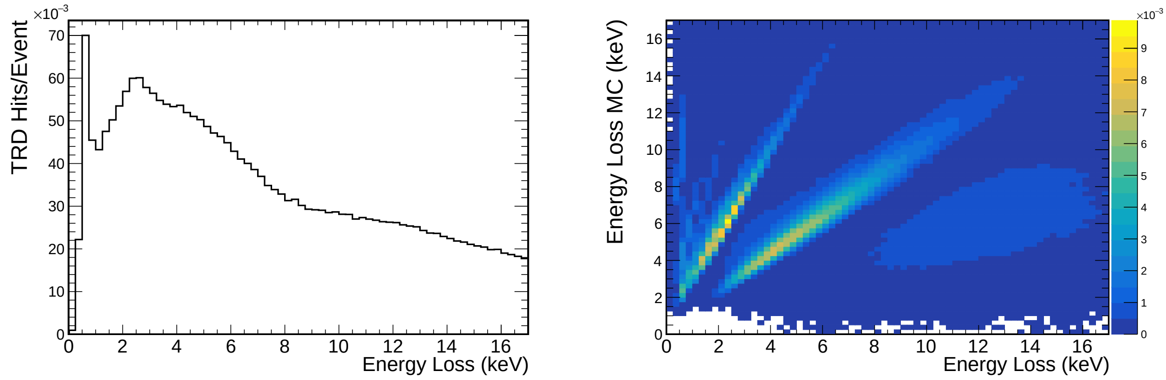

(a) **(b)**

Figure A.2: Energy loss for electrons in the TRD when the TRD-2D is used. A peak appears for low energy losses (a) and a comparison to the MC values for energy loss (b) shows that the low energy loss values lie on a second diagonal. Since this diagonal is above the main diagonal the reconstructed energy loss is lower than expected.

The second diagonal is above the main diagonal and therefore the reconstructed energy loss is lower than expected. Especially for an energy loss below 2 keV, all the hits are on the second diagonal. To locate these hits, the x- and y-distribution of the energy loss in the TRD detector is shown for the hits in Fig. A.3. The hits below 2 keV are all located at $x = \pm 114$ cm and $y = \pm 84$ cm. According to Fig. 2.4 and section 2.1.4 the TRD-2D chambers are of the size $57 \times 57\,\mathrm{cm}^2$ and there are 4 in $x-$ and 3 in y-direction. This fits the observed position of the hits with low energy loss.
Due to this unsolved problem, the geometry without TRD-2D is used, as stated in section 3.2.

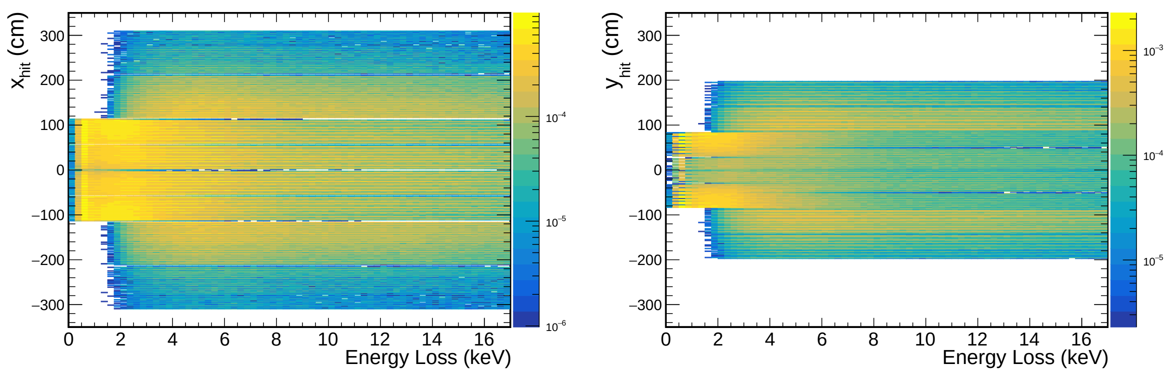

(a) **(b)**

Figure A.3: x and y position in the TRD as function of the momentum. Low enrergy loss values are located between $x = \pm 114$ cm and $y = \pm 84$ cm. This is the position of the TRD-2D chambers.

A.3 Centrality Correction

To correct for the change in centrality, a numerical program based on the Glauber model is used [37]. This program calculates a density distribution for projectile and target using the Woods–Saxon density profile. Subsequently the number of participants N_{part}, the nucleons that encountered at least one inelastic nucleon–nucleon collision, is computed.
For the calculation, the web interface is used with mass numbers $A = 197$, and $B = 197$ for gold as projectile and target. The statistics are set to 10000 trials per integral. Impact parameters 0–3.3 fm and 0–6.7 fm are chosen, corresponding to centrality classes of 0–5.01% and 0–20.66%, respectively. The orrection factor is given by $\frac{N_{\mathrm{part}0-20\%}}{N_{\mathrm{part}0-5\%}} = \frac{257.6}{336.4} \approx 0.7658$.

A.4 Additional Plots and Tables

Table A.1: Schematic overview of applied cuts in PAPA. Detailed cut values and geometry-dependent adaptations are discussed in sections 4.1 and 4.2.

Cut Class	Cut Name	Purpose/Range
PreCuts	mcPDG	MC particle selection
	accCuts	Acceptance cuts
	p_T	$p_T > 0.05\,\mathrm{GeV/c}$
	recSTSMVD	STS+MVD hits > 3
	rec1TRD	TRD hits > 0
	PairPreFilter	$m_{\mathrm{inv}} > 0.025\,\mathrm{GeV}$
	preCuts	χ^2/NDF < 3 to vertex
	recSTS	STS hits > 2
	recMVD	MVD hits > 2
RecCutsPID	recTRD	TRD hits > 2
	recTOF	TOF hits > 0
PID Cuts	recRICH	RICH hits > 5
	RICH ANN	80–90% e^- efficiency
	TRD Likelihood	70–80% e^- efficiency
	TOF β	$\Delta\beta_e > -5 \times 10^{-3}$
	STS dE/dx_{STS}	$dE/dx_{\mathrm{STS}} < 3.2 \times 10^4\,\mathrm{e}/300\,\mu\mathrm{m}$
Segment Cut	Opening angle	

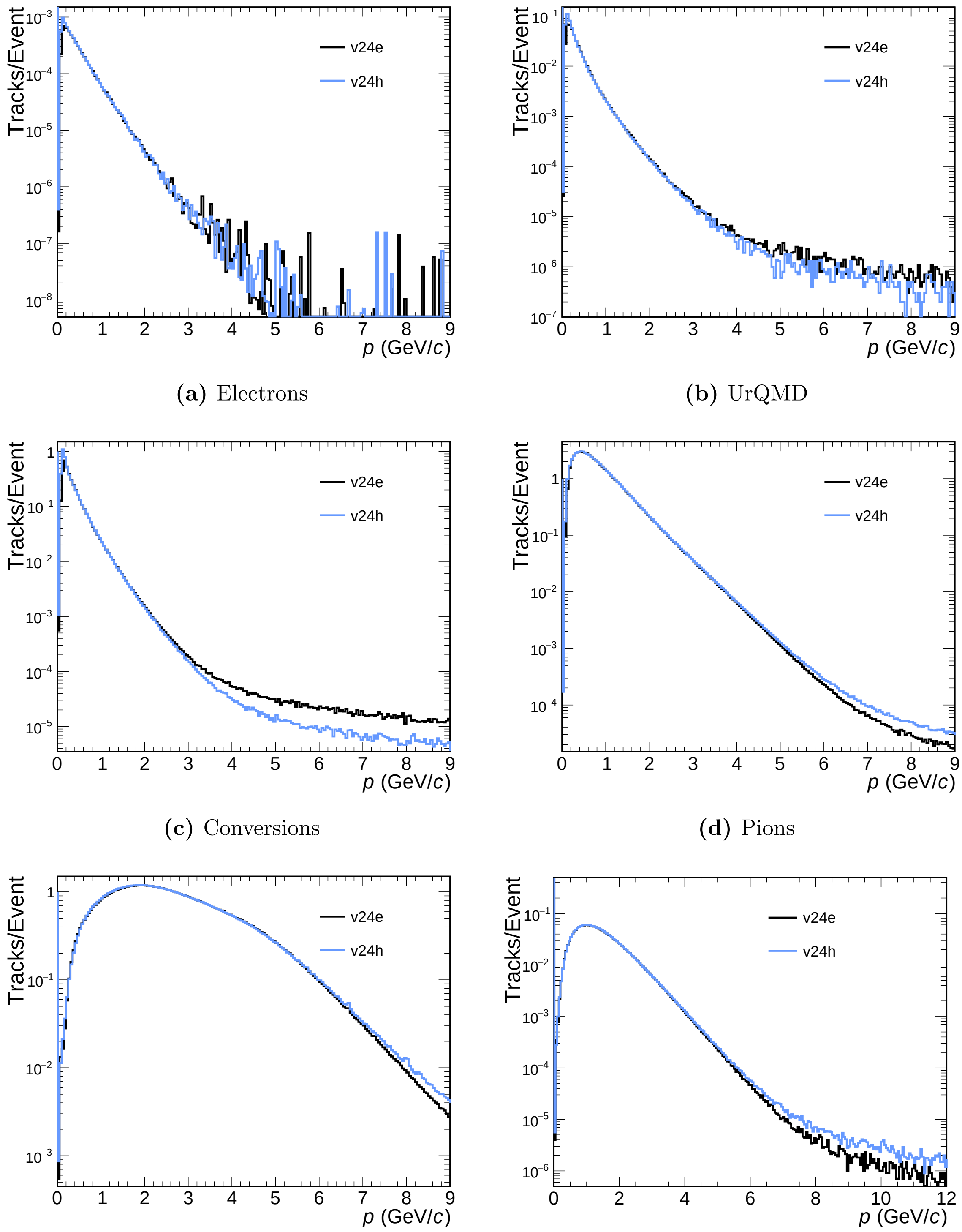

(a) Electrons (b) UrQMD

(c) Conversions (d) Pions

(e) Protons (f) Kaons

Figure A.4: Momentum distribution of the different particle sources before analysis for both setups, corresponding to the distribution in Fig. 4.2. Due to the lower magnetic field, there are more low momentum tracks in the `v24h` setup, which is visible up to 0.4 GeV/c. The three electron sources have a peak below 0.4 GeV/c while the momentum distributions of the hadrons peak above 0.4 GeV/c. Thus, the additionaly particles are relatively relevant only for the electron sources which is observable in the distribution in Fig. 4.2.

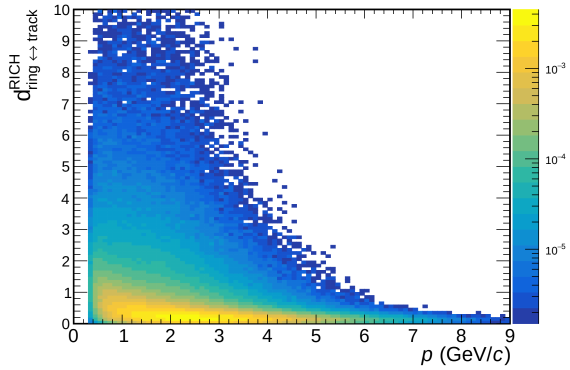

(a) v24e Electrons

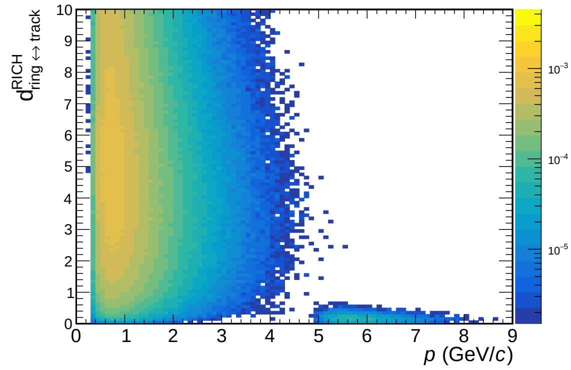

(b) v24e Pions

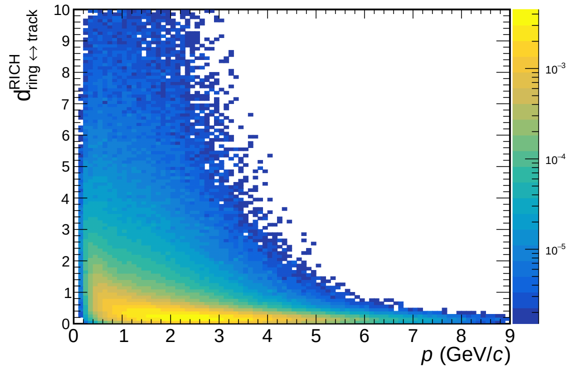

(c) v24h Electrons

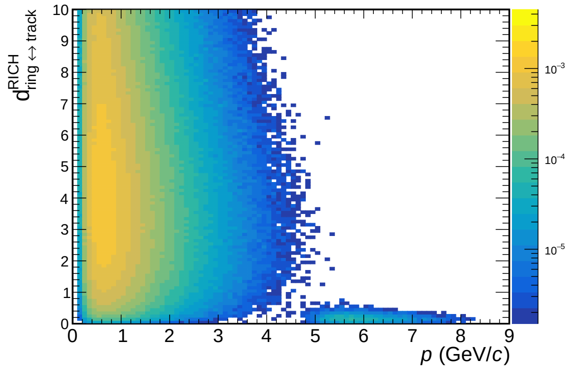

(d) v24h Pions

Figure A.5: Ring to track distance as function of momentum for electrons and pions for the two different setups, respectively. While the distance is widely distributed for pions up to 5 GeV/c, it is close to 0 above. For electrons it is close to 0 across the whole momentum range, but at low momenta it spreads to higher distances. For tracks matched to the corresponding ring, the distance should be small. Falsely matched tracks can have a higher distance. This is the case for pions up to the Cherenkov threshold. Since they do not produce Cherenkove light and thus do not form rings, the tracks are fake matches. Only above the Cherenkov threshold there are true matches which is also visible in the lower distance above 5 GeV/c. For electrons, the distance deviates stronger from 0 at low momenta which affects the classification of the RICH ANN.

A.5 Additional Plots for the `v24h` Setup

Each plot shown only for the **v24e** setup is shown here for the **v24h** setup structured in the same way as in chapter 4.

A.5.1 PID cuts

A.5.1.1 RICH

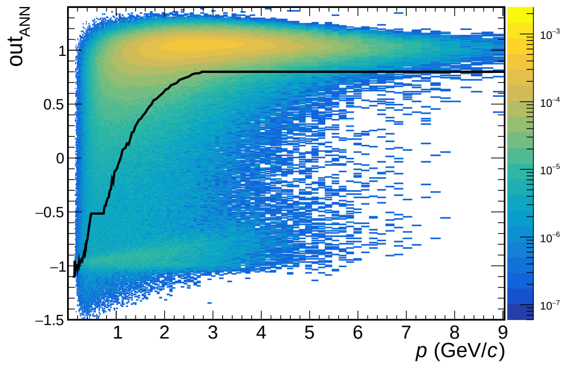

(a) Electrons

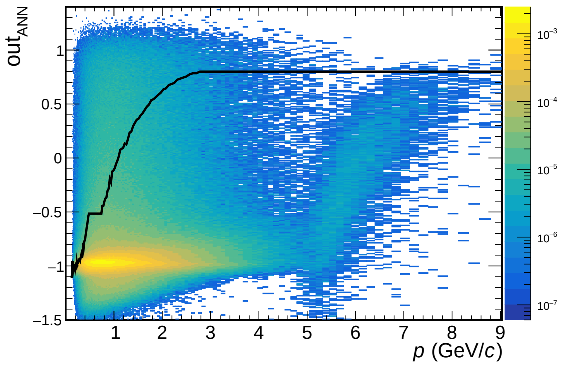

(b) Pions

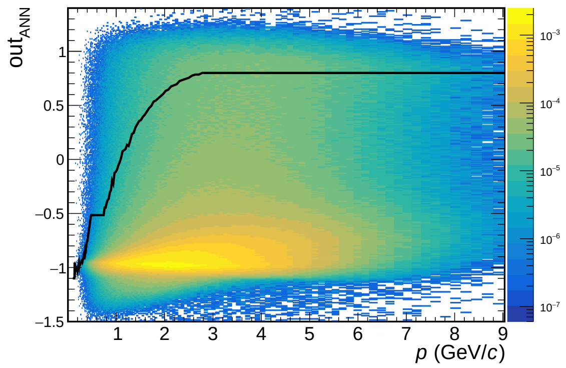

(c) Protons

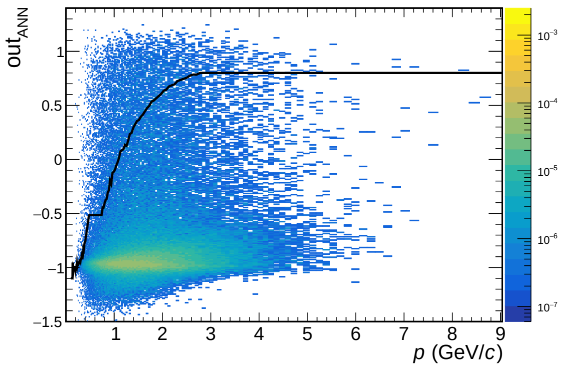

(d) Kaons

Figure A.6: ANN output as a function of the momentum for electrons, pions, protons, and kaons for the **v24h** setup. The black line marks the applied cut corresponding to the chosen electron efficiency.

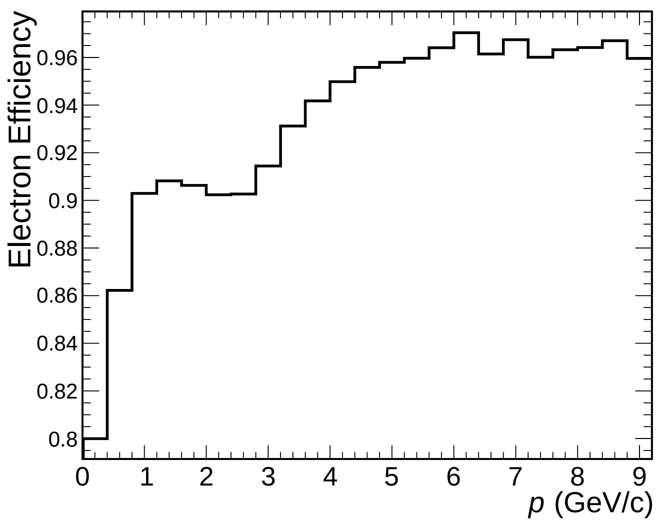

Figure A.7: Electron efficiency as a function of momentum for the RICH ANN cut for the v24h setup. Efficiency is fixed at 80 % up to 1 GeV/c and 90 % up to 3 GeV/c. Above 3 GeV/c, the constant ANN threshold of 0.75 yields even higher efficiency.

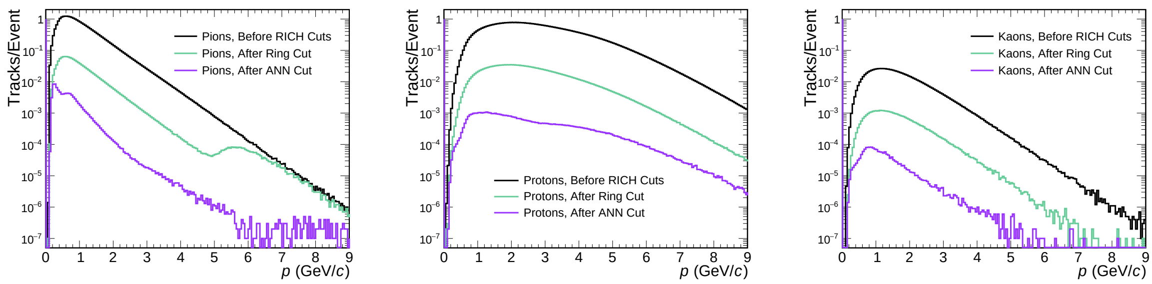

(a) Pions **(b)** Protons **(c)** Kaons

Figure A.8: Momentum distribution for pions (a), protons (b), and kaons (c), before any RICH cuts, after the ring cut, and after the ANN cut for the v24h setup. For kaons and protons, the number of tracks is reduced across the full momentum range by both cuts. For pions, the ring cut reduces tracks only up to about 5.5 GeV/c, because pions above their Cherenkov threshold of 4.65 GeV/c also produce rings.

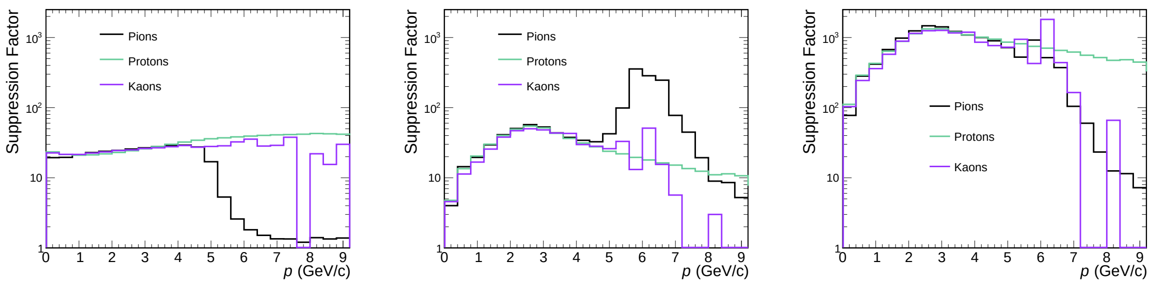

(a) Ring Cut **(b)** ANN Cut **(c)** Combined

Figure A.9: Suppression factors as a function of momentum for the ring cut (a), the ANN cut (b), and the combination of both (c) for pions, protons, and kaons each for the `v24h` setup. The pion Cherenkov threshold is visible because pion suppression is dominated by the ANN cut at high momenta, while proton and kaon suppression remains almost constant over the entire momentum range for both cuts.

A.5.1.2 TRD

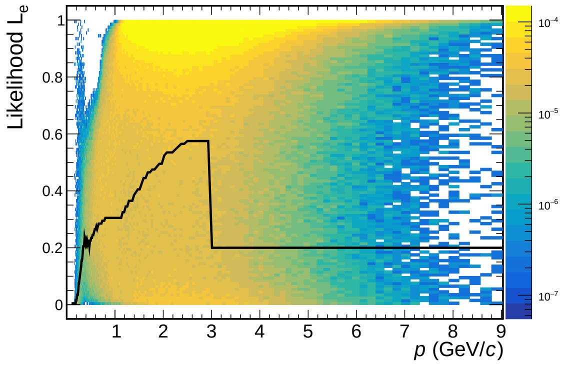

(a) Electrons

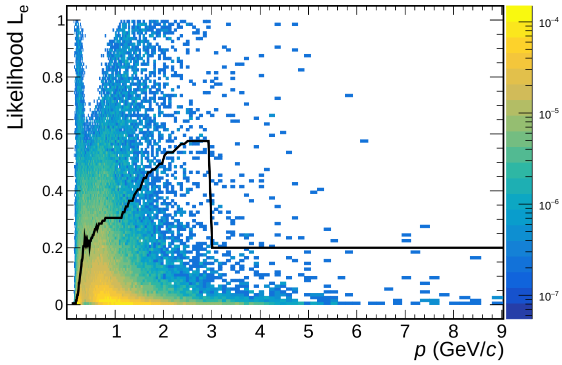

(b) Pions

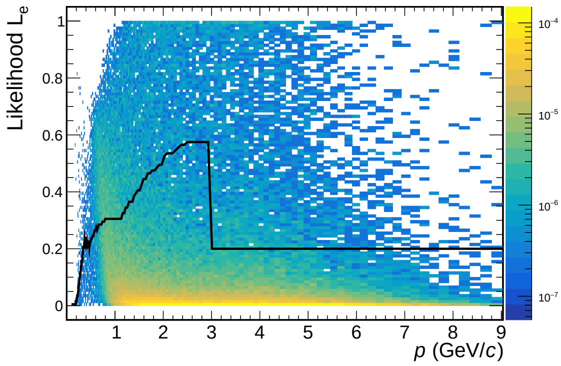

(c) Protons

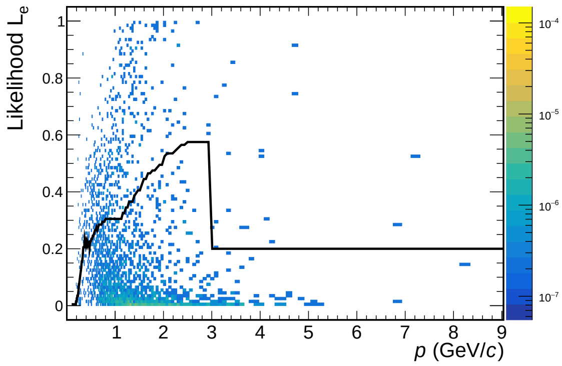

(d) Kaons

Figure A.10: Electron likelihood L_e as a function of momentum for electrons, pions, protons, and kaons for the `v24h` setup. The black line shows the applied cut corresponding to a fixed electron efficiency of 70–80 % up to 3 GeV/c. Above this, the constant $L_e = 0.2$ threshold increases electron efficiency while maintaining pion suppression.

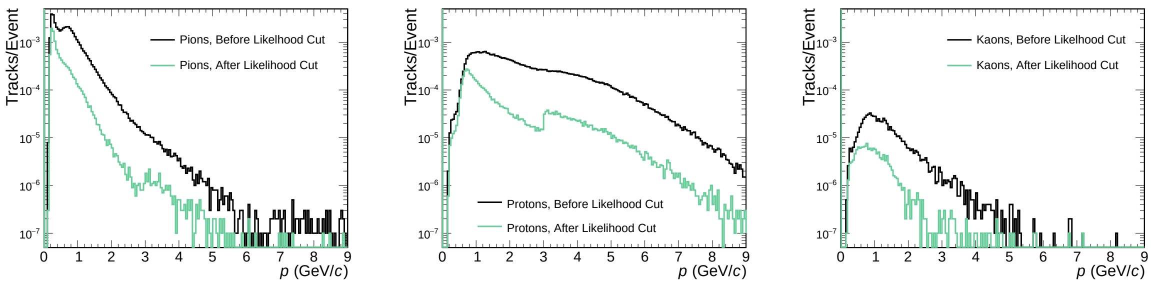

(a) Pions **(b)** Protons **(c)** Kaons

Figure A.11: Momentum distributions before and after TRD cut for pions, protons, and kaons for the `v24h` setup. Track suppression is visible above $\sim 0.5\,\text{GeV/c}$ across all hadron species.

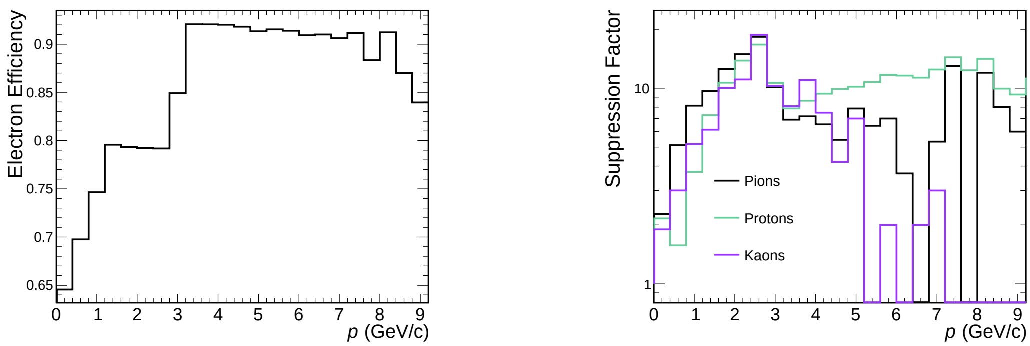

(a) Electron efficiency as a function of momentum.

(b) Suppression factors for pions, protons, and kaons as a function of momentum.

Figure A.12: Electron efficiency and corresponding hadron suppression achieved with the TRD likelihood cut for the `v24h` setup. The efficiency is fixed at 70 % at low and 80 % at intermediate momenta.The constant high-p cut ($L_e = 0.2$) yields $> 90\,\%$ electron efficiency while maintaining pion suppression.

A.5.1.3 TOF

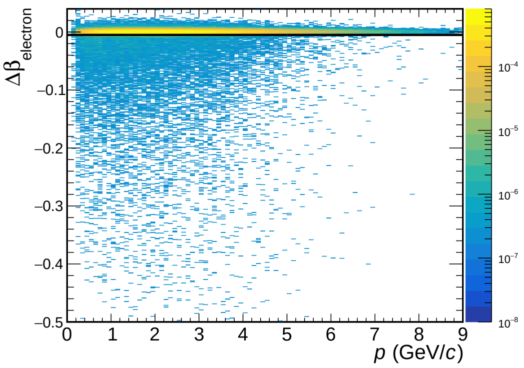

(a) Electrons

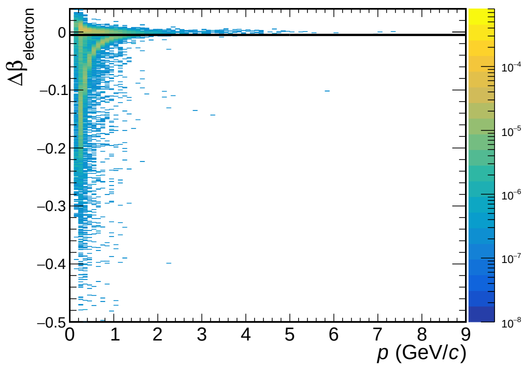

(b) Pions

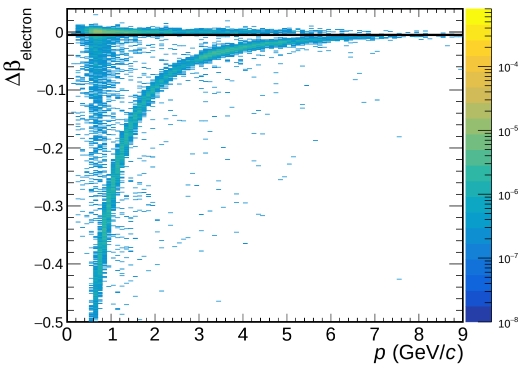

(c) Protons

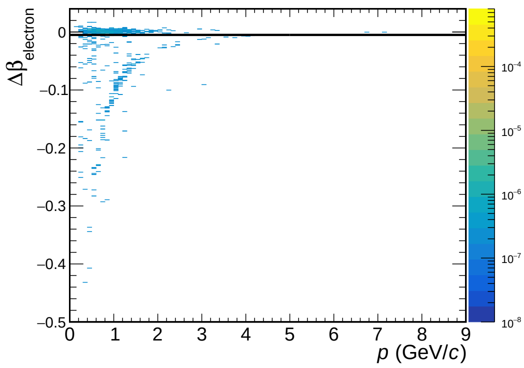

(d) Kaons

Figure A.13: $\Delta\beta$ as a function of momentum for the `v24h` setup. The β values calculated from TOF information are compared with those expected from track momentum assuming the electron mass. The difference $\Delta\beta$ is shown for electrons, pions, protons, and kaons. Since $\Delta\beta = 0$ is expected for electrons, a cut is applied, rejecting tracks with $\Delta\beta < 0.015$. Because β depends on the mass, $\Delta\beta$ approaches 0 with increasing momentum, and the effect is stronger for heavier particles.

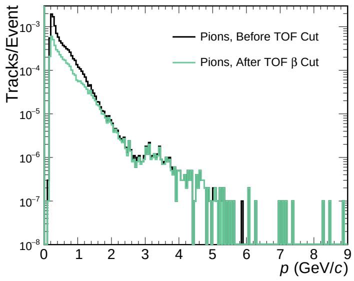

(a) Pions

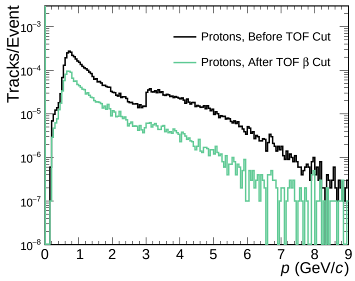

(b) Protons

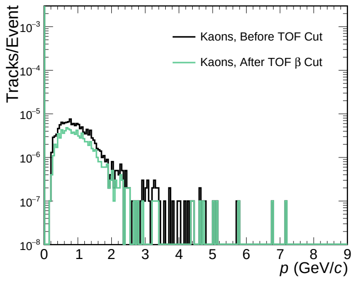

(c) Kaons

Figure A.14: Momentum distribution before and after the TOF cut for different particles for the `v24h` setup. The number of protons is reduced across the whole momentum range, similar to kaons, although the number of kaons was already small prior to the cut. Due to their low rest mass, pions are only suppressed for ($p < 2\,\mathrm{GeV/c}$).

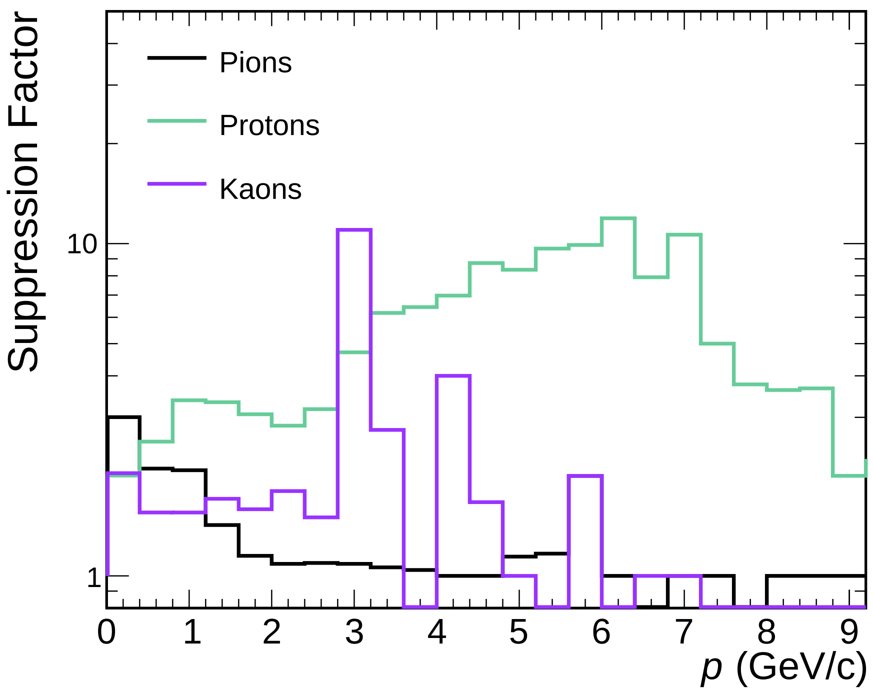

Figure A.15: Suppression factors of the TOF cut for the `v24h` setup. Due to the mass dependence in eq. (4.5), the strongest suppression is observed at low momenta. Kaons and protons are suppressed over nearly the entire momentum range of the remaining tracks, whereas pions are only suppressed below $2\,\mathrm{GeV/c}$.

A.5.1.4 STS

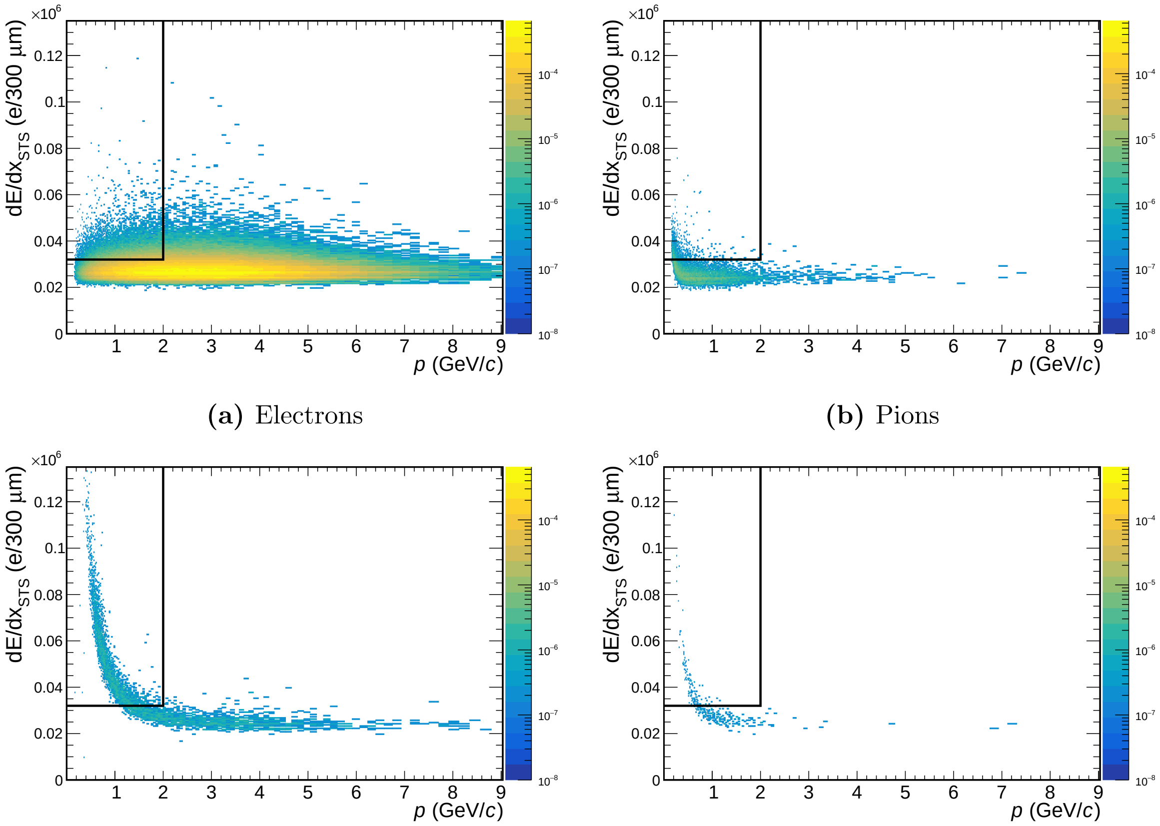

(a) Electrons **(b)** Pions **(c)** Protons **(d)** Kaons

Figure A.16: Energy loss in the STS layers as a function of momentum for the `v24h` setup. Energy loss in silicon for protons and kaons is higher at low momenta compared to electrons. A cut is applied along this edge, rejecting tracks with $dE/dx_{STS} > 3.2 \times 10^4\ e/300\ \mu$m for $0 < p < 2\,$GeV/c marked in black.

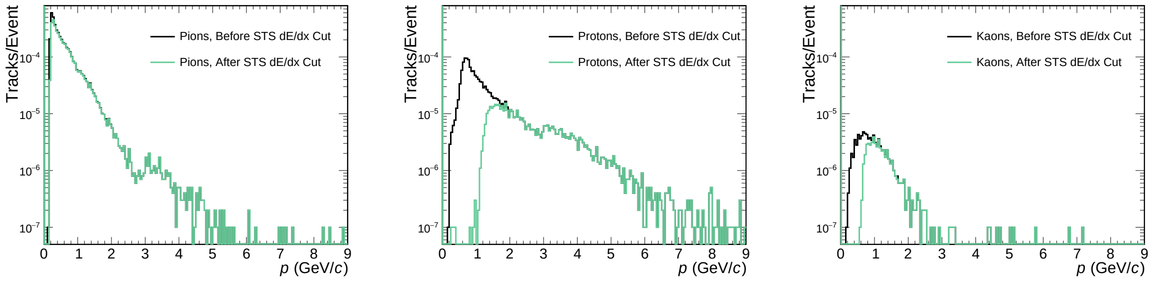

(a) Pions **(b)** Protons **(c)** Kaons

Figure A.17: Momentum distribution before and after the STS cut for protons, pions, and kaons for the `v24h` setup. The number of protons and kaons is reduced up to 2 GeV and 1 GeV, respectively, while there is no visible effect for pions.

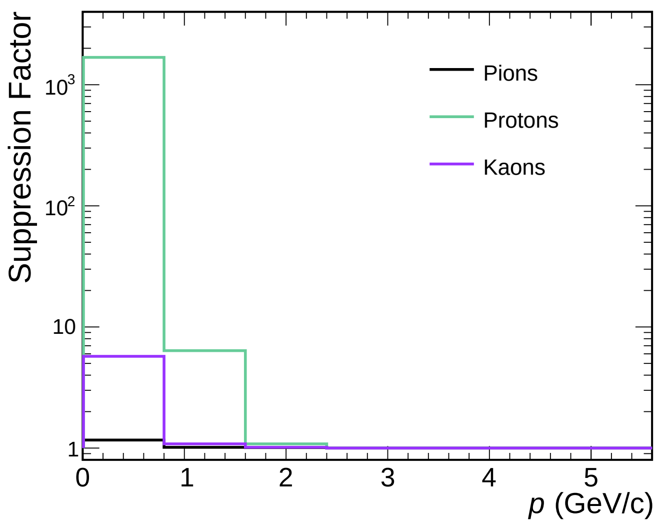

Figure A.18: Suppression factor as function of the momentum for the STS cut for the `v24h` setup. Protons and kaons at low momenta are suppressed by the STS cut while there is no effect on pions because the energy loss in silicon onl differs from electrons for protons and kaons at low momenta.

A.5.1.5 Electron

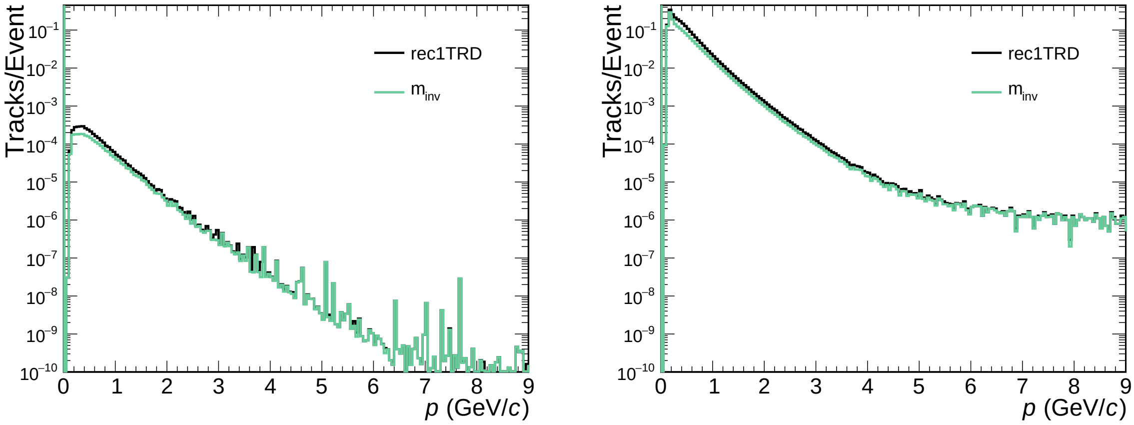

(a) Pluto electrons **(b)** Conversion electrons

Figure A.19: Momentum distribution of Pluto electrons and conversion electrons before and after the invariant-mass cut.

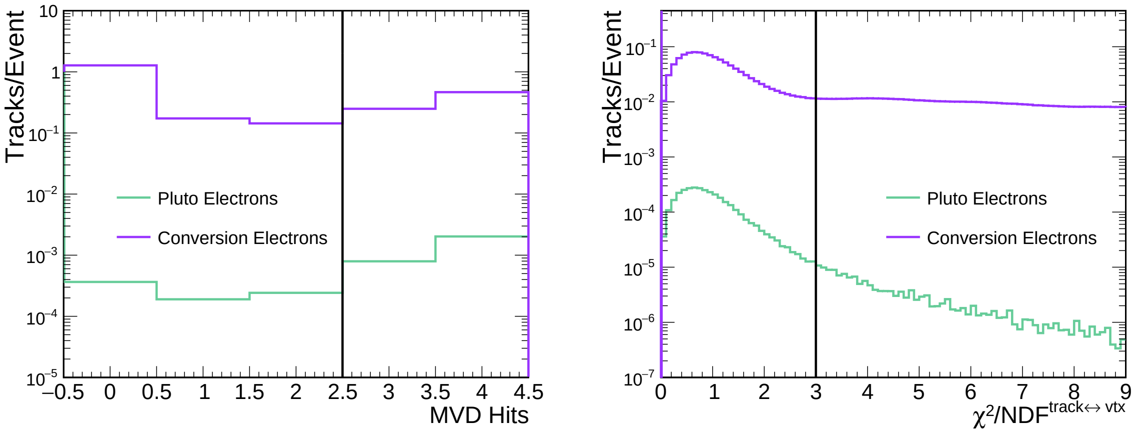

(a) MVD Hits **(b)** χ^2

Figure A.20: MVD Hits and χ^2/NDF distribution before the invariant-mass cut comparing Pluto and conversion electrons for the `v24h` setup. A cut is applied on both since signal electrons originating from the collision point should have lower χ^2 and more MVD Hits than conversion electrons produced along the detector.

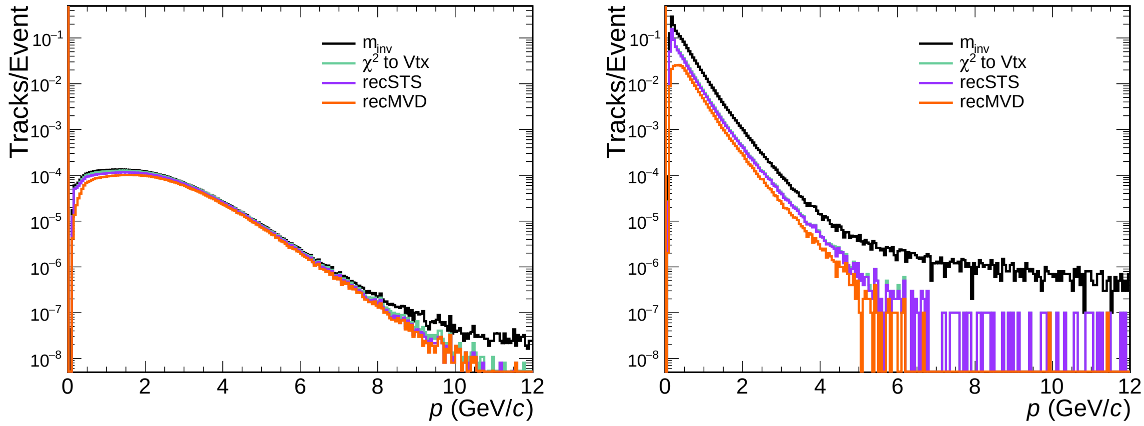

(a) Pluto electrons (b) Conversion electrons

Figure A.21: Momentum distribution after different position-related cuts of Pluto and conversion electrons for the `v24h` setup.

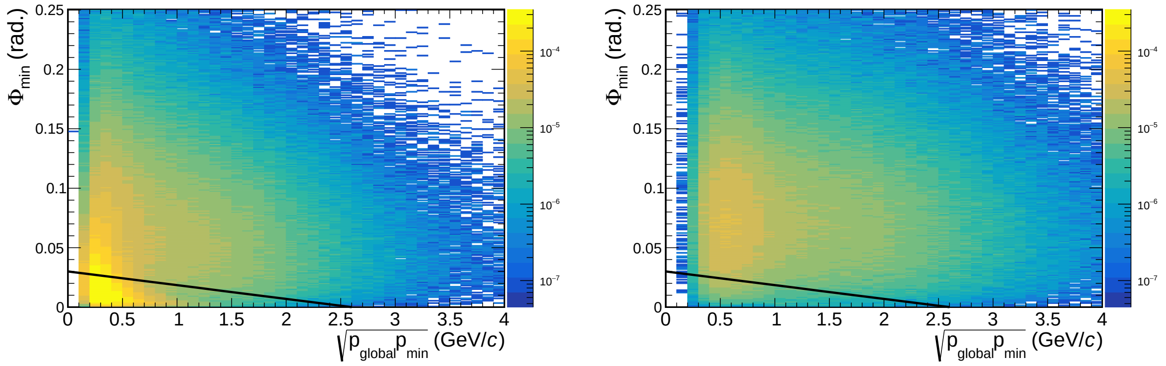

(a) $\gamma \to e^+e^-$ (b) $\omega \to e^+e^-$

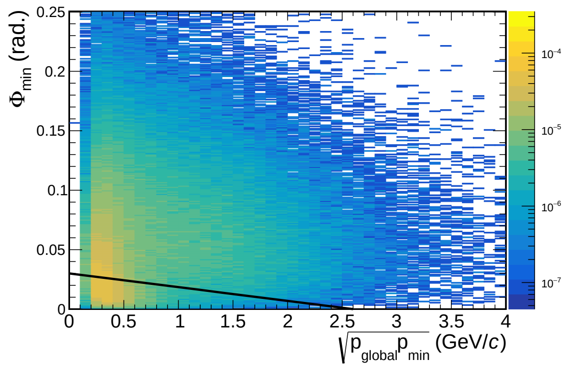

(c) $\pi^0 \to \gamma e^+e^-$

Figure A.22: Opening angle Φ_{min} for $\sqrt{p_{\text{min}} p_{\text{global}}}$ for different decays for the `v24h` setup. Low invariant mass decays have true matches which are visible in a bulk at small angles, which is removed by a cut indicated by the black line.

A.6 Background Simulation

The background simulation described in section 4.6 was also used for a comparable simulation, which was performed for $P_{\text{beam}} = 4.4\,\text{GeV/c}$, a centrality of $0 - 5\,\%$, the `v24h` setup with a $25\,\mu$m target and a magnetic field scaling of 0.5. The resulting comparison of input and output of the random background simulation is shown in Fig. A.23. As in Fig. 4.41, the background in the file is higher at low M_{inv}, but there is no shift across the whole M_{inv} range. The multiplicities of the input and output files are shown in Fig. A.24 for positive and negative UrQMD tracks for the two setups and the old simulation, respectively. Each sampled multiplicity distribution fits the one of the input file. Thus the random sampling works for both simulation campaigns and the differences between input and simulated output are expected to be caused by particle correlations. While pairs in UrQMD simulations are correlated, there is no such correlation in the random sampling.

.

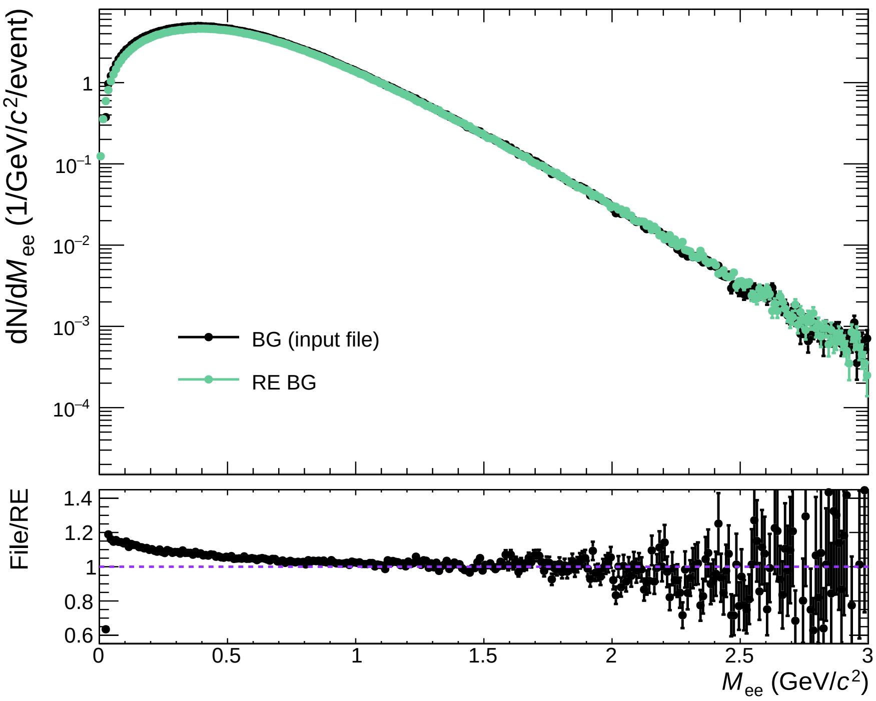

Figure A.23: Invariant mass distribution of the background simulated by the fast simulation approach compared to the background in the input file for a comparable simulation campaign.

The two main differences of the simulation campaigns are the updated UrQMD version and the changed target. As discussed in section 4.5 the target causes additional conversion background and thus more correlated pairs, which can be investigated by excluding all conversions.

Other than that, the change in centrality and UrQMD version are harder to evaluate. However, the prior simulation campaign shows that the background simulation works for the used energy and geometry.

As a next step, different background sources are excluded to identify the reason for the observed difference. There are also simulations available for $P_{\text{beam}} = 12\,\text{GeV/c}$ with the same UrQMD version which can be used for further investigations. Meanwhile the solution described in section 4.6 is used.

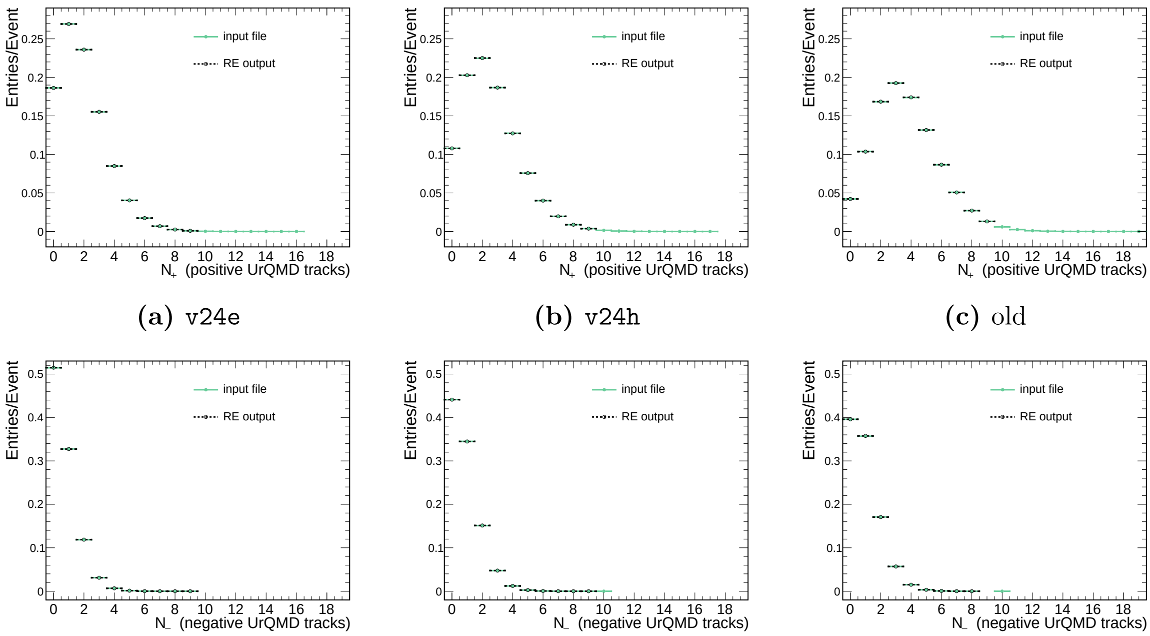

(a) v24e (b) v24h (c) old

(d) v24e (e) v24h (f) old

Figure A.24: Multiplicity for positive and negative UrQMD tracks for three different random background simulations in comparison to the multiplicity of the input files.

Bibliography

[1] B. Povh, K. Rieht, C. Scholz, F. Zetsche, W. Rodejohann, *Teilchen und Kerne*, Springer, **2014**.

[2] A. Andronic, *International Journal of Modern Physics A* **2014**, *29*, 1430047.

[3] L. Evans, P. Bryant, *Journal of Instrumentation* **2008**, *3*, S08001.

[4] T. Galatyuk, *Nuclear Physics A* **2019**, *982*, The 27th International Conference on Ultrarelativistic Nucleus-Nucleus Collisions: Quark Matter 2018, 163–169.

[5] R. Rapp, H. van Hees, *The European Physical Journal A* **2016**, *52*, DOI 10.1140/epja/i2016-16257-0.

[6] A. Meyer-Ahrens, PhD thesis, Univerität Münster, **2025**.

[7] P. Senger, *Particles* **2020**, *3*, 320–335.

[8] FAIR_GSI_de, X post, https://x.com/fair_gsi_de/status/886125178496835585 (visited on 02/11/2026).

[9] G. FAIR, CBM page, https://www.cbm.gsi.de/sites/default/files/inline-images/FAIR_CBM.jpg (visited on 02/11/2026).

[10] Micro Vertex Detector (MVD), tech. rep., **2021**.

[11] Silicon Tracking System (STS), tech. rep., The STS working group and the CBM collaboration, **2013**.

[12] Ring Imaging Cherenkov (RICH) detector, tech. rep., The RICH working group and the CBM collaboration, **2013**.

[13] Addendum Transition Radiation Detector 2D (TRD-2D), tech. rep., The CBM Collaboration, **2021**.

[14] Transition Radiation Detector (TRD), tech. rep., The CBM Collaboration, **2018**.

[15] T. W. Group, Technical Design Report for the CBM Time - of - Flight System (TOF), tech. rep., The CBM Collaboration, **2014**.

[16] M. Teklishyn, Detectors and Electronics for the CBM experiment at FAIR, **2025**.

[17] G. Eigen, *Detectors in High-Energy Physics Experiments*, Springer, **2025**.

[18] J. N. Guenther, *The European Physical Journal A* **2021**, *57*, 136.

[19] M. A. Stephanov, QCD phase diagram: an overview, **2006**.

[20] P. Steinbrecher, *Nuclear Physics A* **2019**, *982*, 847–850.

[21] D. Rischke, *Progress in Particle and Nuclear Physics* **2004**, *52*, 197–296.

[22] W. Demtröder, *Experimentalphysik 4 Kern-, Teilchen und Astrophysik*, SpringerSpektrum.

[23] A. Andronic, P. Braun-Munzinger, K. Redlich, J. Stachel, *Nature* **2018**, *561*, 321–330.

[24] D. Miśkowiec, Heavy-ion collision basics, **2023**.

[25] B. Friman, C. Höhne, P. Senger, *The CBM physics book*, Springer, **2011**.

[26] P. Salabura, *Acta Phys. Polon. B* **2008**, *39*, (Eds.: M. Pfutzner, T. Matulewicz), 307–320.

[27] R. Rapp, H. van Hees, *Physics Letters B* **2016**, *753*, 586–590.

[28] P. Senger, *Physica Scripta* **2020**, *95*, 074003.

[29] R. Rapp, **2013**.

[30] T. U. group, **2014**.

[31] I. Fröhlich, T. Galatyuk, R. Holzmann, J. Markert, B. Ramstein, P. Salabura, J. Stroth, *Journal of Physics: Conference Series* **2010**, *219*, 032039.

[32] CERN, GEANT Detector Description and Simulation Tool, **1994**.

[33] M. Bleicher, E. Zabrodin, C. Spieles, S. A. Bass, C. Ernst, S. Soff, L. Bravina, M. Belkacem, H. Weber, H. Stöcker, W. Greiner, *Journal of Physics G: Nuclear and Particle Physics* **1999**, *25*, 1859–1896.

[34] S. Bass, *Progress in Particle and Nuclear Physics* **1998**, *41*, 255–369.

[35] https://www.gsi.de/work/wissenschaftliche$_{n}etzwerke/helmholtz_{v}irtuelle_{i}nstitute/unigen$, Last visited 23.11.2025.

[36] I. Froehlich, L. C. Boado, T. Galatyuk, V. Hejny, R. Holzmann, M. Kagarlis, W. Kuehn, J. G. Messchendorp, V. Metag, M. .-. Pleier, W. Przygoda, B. Ramstein, J. Ritman, P. Salabura, J. Stroth, M. Sudol, Pluto: A Monte Carlo Simulation Tool for Hadronic Physics, **2007**.

[37] D. Miskowiec et al., Nuclear Overlap Calculation Code, Web interface for a Glauber model-based nuclear overlap calculation, including Monte Carlo sampling of the impact parameter space., GSI Helmholtzzentrum für Schwerionenforschung, **2000**, http://web-docs.gsi.de/~misko/overlap (visited on 04/20/2026).

[38] T. Galatyuk, CBM Dilepton wiki page, %7B%5Curl%7Bhttps://cbm-wiki.gsi.de/PWG/CbmDilepton%7D%5CUrlBreak%5Curl%7BInfoFilesAuAu3400%7D%7D (visited on 02/11/2026).

[39] E. Bechtel, *Development of a detector simulation and reconstruction for the CBM-TRD and the analysis of thermal dielectron pairs in 12 AGeV Au+Au collisions*, Phd thesis, **2020**.

[40] C. Feier-Riesen et al., Implementation of fast simulation techniques to simulate enhanced background for low-mass di-electron pairs, tech. rep. CBM Progress Report 2023, GSI CBM, **2024**.

[41] Mehulkumar Shiroya, Maksym Teklishyn. Private communication, 2026.

Acknowledgements

I want to thank Anton Andronic and Christian Klein-Bösing, not only for giving me the oppurtunity to write this thesis, but also for supporting various other experiences like a great summer at CERN. For the long introduction into PAPA and dileptons I am grateful for Adrians patience.

During my time in the working group I met a lot of great people. In particular, my office made everyday life much more enjoyable: Felix, Adrian again, Axel, Alexandra, Henning, Hannes, and Peter next door. I also really enjoyed working in the lab with Ruben. I also gained valuable skills from Norbert in the workshop, especially when it came to repairing my bike.

Of course, I would also like to thank my family, in particular my parents, who always support me and the different side quests I am chasing. Finally, I would like to thank those who support me on my various adventures, even though they have to deal with my limited time resources; especially Niklas.

Declaration of Academic Integrity

I hereby confirm that this thesis, entitled Dielectron Performance of the CBM Experiment at $\sqrt{s}$ = 3.19 GeV is solely my own work and that I have used no sources or aids other than the ones stated. All passages in my thesis for which other sources, including electronic media and AI Tools, have been used, be it direct quotes or content references, have been acknowledged as such and the sources cited. I am aware that plagiarism is considered an act of deception which can result in sanction in accordance with the examination regulations.

____

(date, signature of student)

I consent to having my thesis cross-checked with other texts to identify possible similarities and to having it stored in a database for this purpose.

I confirm that I have not submitted the following thesis in part or whole as an examination paper before.

____

(date, signature of student)